APPENDIX E

FCT DOCUMENT COVER SHEET [1]

Name/Title of Deliverable/Milestone/Revision No.	Coupled model for heat and water transport in a high level waste repository
Work Package Title and Number	Salt R&D FT-13LA081801
Work Package WBS Number	1.02.08.18
Responsible Work Package Manager	Doug Weaver / (Name/Signature)

Date Submitted 9-30-2013

Quality Rigor Level for Deliverable/Milestone[2]	■ QRL-3	☐ QRL-2	☐ QRL-1 ☐ Nuclear Data	☐ Lab/Participant QA Program (no additional FCT QA requirements)

This deliverable was prepared in accordance with Los Alamos National Laboratory
(Participant/National Laboratory Name)

QA program which meets the requirements of
☐ DOE Order 414.1 ☐ NQA-1-2000 ■ Other

This Deliverable was subjected to:

■ Technical Review ☐ Peer Review

Technical Review (TR)
Review Documentation Provided
☐ Signed TR Report or,
☐ Signed TR Concurrence Sheet or,
■ **Signature of TR Reviewer(s) below**

Name and Signature of Reviewers
HARI VISWANATHAN

Peer Review (PR)
Review Documentation Provided
☐ Signed PR Report or,
☐ Signed PR Concurrence Sheet or,
☐ Signature of PR Reviewer(s) below

NOTE 1: *Appendix E should be filled out and submitted with the deliverable. Or, if the PICS:NE system permits, completely enter all applicable information in the PICS:NE Deliverable Form. The requirement is to ensure that all applicable information is entered either in the PICS:NE system or by using the FCT Document Cover Sheet.*

NOTE 2: *In some cases there may be a milestone where an item is being fabricated, maintenance is being performed on a facility, or a document is being issued through a formal document control process where it specifically calls out a formal review of the document. In these cases, documentation (e.g., inspection report, maintenance request, work planning package documentation or the documented review of the issued document through the document control process) of the completion of the activity, along with the Document Cover Sheet, is sufficient to demonstrate achieving the milestone. If QRL 1, 2, or 3 is not assigned, then the Lab / Participant QA Program (no additional FCT QA requirements) box must be checked, and the work is understood to be performed and any deliverable developed in conformance with the respective National Laboratory / Participant, DOE or NNSA-approved QA Program.*

Coupled model for heat and water transport in a high level waste repository in salt

Fuel Cycle Research & Development

Prepared for
U.S. Department of Energy
Used Fuel Disposition Campaign
Milestone M2FT-13LA08180113

Stauffer, P.H., D.R. Harp, A.B. Jordan, Z. Lu, S. Kelkar, Q. Kang, J. Ten Cate,H. Boukhalfa, Y. Labyed, P.W. Reimus, F.A. Caporuscio, T.A. Miller, B.A. Robinson
Los Alamos National Laboratory

September 30, 2013

FCRD-UFD- 2013-000206
Los Alamos National Laboratory Document LA-UR-13-27584

EXECUTIVE SUMMARY

This report summarizes efforts to simulate coupled thermal-hydrological-chemical (THC) processes occurring within a hypothetical high-level waste (HLW) repository in bedded salt. Initial simulations with only thermal conduction are followed by coupled thermal-hydrological cases, culminating in a series of simulations coupling thermal, hydrological, and chemical processes. Addition of chemical processes to the system allows precipitation and dissolution of salt to be captured, as elevated temperatures drive water and water vapor flow around hot waste packages. Additional development includes the implementation of an algorithm for mineral dehydration based on data collected by LANL as part of an experimental task accompanying this project. The primary goal of this study is to use numerical modeling to gain insight into the dominant heat and mass transport processes that are driven by heat-generating HLW buried in bedded salt during the first few years of emplacement. The interaction between liquid brine flowing towards the heat source and establishment of a heat pipe in the Run of Mine (RoM) backfill caused by boiling and vapor condensation can lead to changes in porosity, permeability, saturation, and thermal conductivity of the salt surrounding potential waste canisters. The Finite Element Heat and Mass transfer code (FEHM) is used to simulate these highly coupled thermal, hydrological, and chemical processes.

Although the models developed are generic, the context in which these processes are studied is the Salt Defense Disposal Initiative (SDDI) test (DOE CBFO, 2012), which features a generic waste disposal concept with canisters (represented in the experiment by cylindrical heaters) resting on the drift floor and covered by RoM backfill. Differing canister heat loads, from 50 W to 1000 W, are modeled here, and the sensitivity of results to unknown hydrological and thermal parameters is investigated. Many significant new capabilities were added to the FEHM code in support of this effort (Chapter 2). These include previously developed or newly implemented representations of: salt solubility as a function of temperature; water vapor diffusion coefficient as a function of pressure, temperature, and porosity; vapor pressure of water as a function of aqueous sodium chloride concentration and temperature; temperature- and porosity-dependent thermal conductivity of the RoM salt; capillary behavior and permeability-porosity relationships for RoM salt; salt dissolution/precipitation processes; mineral dehydration and its influence on the water balance; and analyses to capture the effect of convective and radiative heat transfer in the air-filled portion of a drift. New analyses of the behavior of the system are presented that result from the code updates and incorporation of important coupled processes.

Benchmarking exercises are presented (Chapter 3) that compare simulation results to recent LANL experiments on the thermal behavior of salt and water release from clay dehydration (FY13), as well as analytical solutions and 1980's era non-heated and heated experimental data from WIPP. These

modeling exercises serve to confirm that the FEHM model, when assigned appropriate parameter values, is able to reproduce information on water migration toward the drift opening under isothermal and heated conditions. Similarly, benchmarking of the model against newly performed heat transport experiments on RoM salt provide confidence that the thermal properties of the backfill are properly captured.

The numerical model is then used to make predictions of temperatures, porosity changes, and saturations that may occur for waste emplaced using the in-drift concept. These simulations are presented in order of increasing complexity, from thermal (T), to thermal-hydrologic (TH), to thermal-hydrologic-chemical (THC) (Chapters 4, 5, and 6, respectively) in order to illustrate the relative importance of each process. These calculations are presented in the context of a future field test, and include, for the most complex analyses, full THC calculations with initial results from clay dehydration simulations. The results indicate that during the early phases of waste emplacement, or in a field-scale heater test such as the proposed two year SDDI test, formation of a heat pipe and subsequent salt redistribution will be enhanced by a combination of high heat load (>500 W/canister, leading to boiling conditions around the heat source), accessible water (>0.5 wt%), and capillary properties of the RoM backfill. Highly active heat pipes lead to a rind of bone dry, low porosity salt (<5%) deposited around the canisters with a dissolution band located near the top of the RoM backfill, where porosity in the simulations increases above initial values. The dried out low porosity region is coincident with temperatures above boiling (>110°C), while the high porosity region is found across the boiling line where water condenses out of the vapor phase, dissolving RoM backfill.

Evidence for such mass redistribution is found in overcore analysis from WIPP experiments performed in the 1980s, where crushed salt in the annulus of a heated borehole became fused into a low porosity mass in a relatively short period of time. If additional forensic work is performed to examine the properties of the salt in the vicinity of these historic heater tests in WIPP (e.g. Weaver, 2013), attention should be paid to uncovering additional evidence to confirm this observation.

High heat load simulations without an effective heat pipe lead to higher maximum temperatures (200°C vs 150°C) near the HLW canisters. A heat pipe is a very efficient mode of heat transport compared to thermal conduction, a fact that leads to flatter temperature profiles and lower maximum temperatures when a heat pipe is active. Thus, temperature alone should be a sensitive diagnostic for detecting whether or not heat pipes are established in the RoM salt. Also, simulations of low heat loads (<500 W, representing over 90% of the defense HLW) show almost no salt mass redistribution and very little movement of water. Thus, these effects are much more modest at low heat loads where maximum temperatures remain below the boiling point of water.

The complexity of the coupled THC processes controlling the behavior of a salt repository presents challenges regarding the interpretation of the results. For such a complex system, it is difficult to unravel the processes to determine which parameters contribute the most to the overall uncertainty with respect to a given metric. In Chapter 7, a numerical model is set up to examine these uncertainties for the early-time behavior of a generic salt repository with waste emplaced using the in-drift disposal concept. Aside from the trivial result that the heat load of the canisters has a dominant impact on the maximum temperatures attained in the various domains of interest (except for the air gap), the analysis highlighted the importance of properly representing the heat transfer processes across the air gap. Other sensitive properties include the depth of the RoM salt, and the properties of the excavation damage zone (EDZ), also referred to as the disturbed rock zone (DRZ).

Initial modeling investigations are also presented to better represent the release of water from brine inclusions. Chapter 8 presents a model for the pore-scale simulation of brine transport within aggregates of salt crystals with no mineral impurities, in the hope that eventually this model can inform the development of water-release-related parameters in field scale models. The pore-scale model is based on the lattice Boltzmann method and combines the single-component multiphase model, the mass transport model, and the dissolution/precipitation model previously developed at LANL. After confirming the numerical implementation by comparing to other solutions of several multiphase flow and reactive transport problems, the model is used to study the behavior of a brine inclusion in a single salt crystal. Multiphase reactive transport phenomena with phase transition between liquid-vapor phases and dissolution/precipitation of the salt in the brine inclusion are simulated, and effects of initial inclusion size and temperature gradient on the brine behavior are investigated. Many experimental observations are reproduced, and processes observed in ongoing laboratory-scale processes but not yet observed in the model are identified.

Finally, an analysis of potential early-time geomechanical effects is presented (Chapter 9). In general, because the focus of the studies presented herein is on the early-time behavior before large-scale deformation and drift closure take place, these effects are expected to be modest. Of particular interest are the characteristics of the EDZ with respect to fracturing, permeability, and water drainage into to drift. An analysis is presented to justify that, for the purpose of the current modeling, it is adequate to treat the EDZ as a single porosity medium with effective damaged porosity and permeability values appropriate for the EDZ. For much longer time periods and higher heat loads, a fuller description of the evolution of the EDZ will be required.

Table of Contents

List of Figures

List of Tables

COUPLED MODEL FOR HEAT AND WATER TRANSPORT IN A HIGH LEVEL WASTE REPOSITORY IN SALT

1. Introduction

In March, 2012, a workshop was convened that included the Department of Energy Office of Nuclear Energy (DOE-NE) and Office of Environmental Management (DOE-EM), as well as Los Alamos National Laboratory (LANL) and Sandia National Laboratories (SNL) to develop plan for a generic salt repository research effort. The outcome for this workshop was a plan for an 18-month study designed to conduct initial research and to establish the future direction for salt R&D initiatives in the U.S. A series of data compilation, laboratory experiments, and modeling activities were initiated, including the development of coupled thermal-hydrologic-mechanical-chemical (THMC) models that could be used to predict the evolution of a repository after waste emplacement. These advanced models are required because of the strongly coupled processes that are relevant to prediction of heat and fluid transport in salt. One of many such examples is that salt deformation mechanisms are strongly dependent on brine content, and subsequent deformation is coupled back to brine migration through altered porosity, permeability, and water release from bound fluids. The approach called for in the THMC activity is to leverage existing computational models and tools to couple TM, TH, and C phenomena in salt under subsurface repository conditions, with a particular focus on brine accessibility and moisture transport.

Another parallel research track, funded by the DOE Office of Environmental Management (DOE-EM), is underway to plan the Salt Defense Disposal Initiative (SDDI) experiment (DOE CBFO, 2012), a field test designed to confirm the behavior of bedded salt as a geologic disposal medium for defense high level waste (HLW) and spent nuclear fuel (SNF). The SDDI test will extend knowledge accumulated during the licensing and operation of the Waste Isolation Pilot Plant (WIPP) by testing a new disposal concept for emplacement of heat-generating radioactive waste. In previous studies (Robinson et al., 2012; Carter et al., 2011), a waste-disposal concept called the alcove disposal method was introduced and analyzed that innovatively balances safety, ease of operation, and heat management for situations in which waste packages with large heat loads would be disposed in a salt repository. That concept relied on minimal mining, minimal roof support, use of standard mining industry equipment, and minimized the need for specialty equipment. However, because the HLW and defense SNF waste canisters being targeted in the present study are not as hot as those associated with commercial HLW, it is not necessary to spread them out into separate alcoves. For this reason, an alternative concept, called the in-drift disposal method, has been developed in which the waste canisters are placed along the length of a drift, one at a time, and covered with salt backfill for shielding. This efficient in-drift emplacement

configuration will maximize the utilization of the valuable repository real estate, eliminating wasted or empty space.

The in-drift emplacement design concept is based on a disposal strategy in which a series of repository panels, each of which is a subsurface cell consisting of individual drifts, are constructed underground. Mining advances one drift ahead of the drift where disposal operations are being conducted. Retreat waste emplacement is conducted in the open disposal drift by bringing in one canister at a time using a remotely operated vehicle (ROV) and placing it perpendicular to the drift, on the floor. The single canister (or multiple canisters) is covered with run-of-mine (ROM) salt backfill for shielding. The backfill strategy and the target areal heat loading desired will dictate the location of the next canister (typically 1 – 5 foot spacing). The process is repeated until the entire drift is filled and the backfill is emplaced. There are several operational advantages to this disposal concept over traditional concepts such as the borehole emplacement method currently used for Remote Handled waste at WIPP, several of which would lead to tremendous advantages across the entire waste management system for defense wastes. In addition, the in-drift emplacement concept imposes few limits on disposal of a wide array of waste forms, container sizes, shapes and configurations. These operational advantages include: eliminating the need for pre-drilling emplacement holes; straightforward radiation shielding; narrow room height and width; and efficient disposal operations.

Past field heater tests, performed at WIPP, other U.S. salt sites, and worldwide, have provided significant benefit to our knowledge of salt behavior. Previous studies (Callahan et al., 2012; Kuhlman et al., 2012) have synthesized the information from these tests to evaluate the completeness of our understanding, so that an accurate assessment of the need for future field testing could be evaluated. Callahan et al. (2012) concluded that despite the fact that significant thermal testing has been conducted in both bedded and domal salts both in the U.S. and Germany, there is a gap in our experience base regarding the way in which bedded salt such as that at the WIPP site would behave for the in-drift disposal concept, either for intermediate or high heat loads. Testing has been conducted for the borehole disposal concept in both bedded and domal salt, and the in-drift concept has been tested in domal salt, but knowledge of the behavior of bedded salt for the in-drift disposal concept is a gap that still exists. In this context, the principle technical uncertainty that would be addressed is the behavior of the small amounts of water contained in the salt upon heating. Because bedded salt may contain upwards of an order of magnitude more water than domal salt, either in the form of fluid inclusions or hydrous minerals, testing of the in-drift concept in domal salt is insufficient for understanding the behavior of water when subjected to decay heat.

Part of the current report leverages an EM funded numerical mesh for the SDDI test to allow us to examine coupled processes in a hypothetical drift scale heater test in three dimensions at very high resolution. Because of the limited time period for testing (2 years), many questions concerning brine migration for the SDDI test revolve around understanding coupled THC issues because mechanical deformation during 2 years will likely be limited.

The ultimate goal of this project is to model the dominant heat and mass transport processes that are driven by heat generating nuclear waste buried in bedded salt. Liquid brine flow towards the heat source, establishment of a potential heat pipe in the mine-run salt backfill, boiling, and vapor condensation all lead to changes in porosity, permeability, saturation, thermal conductivity, and rheology of the salt surrounding potential waste canisters. The effect of these processes on the final state of the system has not yet been accurately quantified. Advances in numerical simulation over the past year under the scope of this project and new predictions and analysis of likely behavior of the heated salt are presented in this report. The focus of the current work is on inclusion of chemical processes and creation of a robust THC simulator.

Modeling fluid migration around heated waste is critical for understanding transient thermal, hydrological, and rheological states of the repository system. Water found in bedded salt geologic formations can occur as inter-crystalline inclusions (which are brine pockets present in the boundaries between salt crystals and fractures), intra-crystalline (which are brine inclusions of a few microns to larger than several millimeters present within the crystal structure), and water associated with accessory mineral present in salt such as clay or structural water within secondary mineral structures in the salt such as carnallite, kieserite, gypsum, polyhalite and clay. The total water content in bedded salt varies between 0.5 and few wt. % based primarily on clay content. As the salt is heated above 65°C, water is liberated from accessory minerals and is free to migrate through porosity and fractures. Free water contained in bedded salt is projected to flow towards excavated drifts along pressure gradients. This transport will be driven by both far-field lithostatic pressure and capillary pressure due to drying at the drift walls. Within the drifts, water in the backfill covering waste canisters may reach boiling and be transported as vapor. Further, water in equilibrium with bedded salt at 30°C contains over 300 g/L of dissolved salt, which may be left behind as a precipitate when the water boils off, contributing to porosity change in the boiling region. Understanding the highly coupled physical processes involving water and salt transport around hypothetical heat generating waste packages in bedded salt is a necessary step in possible future proposals for disposal of HLW in salt. This research effort uses numerical modeling to further our understanding of these processes.

Past work on modeling nuclear waste disposal in salt has been limited by the capability of models to handle the highly coupled THMC processes. Furthermore, these processes are not completely quantified or understood for the temperature regime in question for HLW. Previous work completed as part of this project is presented in Stauffer et al. (2012). Studies that have laid the foundation for ongoing research to fill science gaps of relevance to HLW disposal in bedded salt are outlined in Hansen and Leigh (2011), Robinson et al. (2012), and Kuhlman and Malama (2013).

In particular, modeling has been conducted to illustrate the likely thermal behavior of a HLW disposal system and to quantify the uncertainties (Clayton and Gable, 2009; Gable et al., 2009). The propagation of the thermal pulse between waste disposal areas was studied. However, details at the drift scale, including fully coupled THMC processes for which we have insufficient knowledge, have a strong bearing on the temperature-time history experienced by the waste and surrounding salt. It was found that uncertainties on the mechanisms and timing of the crushed salt consolidation process lead to a wide range of predictions of the temperatures experienced by the waste form, waste container, and nearby salt.

In addition to direct thermal effects, the THM behavior of the intact salt and the disturbed rock zone (DRZ) is insufficiently understood. The permeability of the D will, for some period of time, be orders of magnitude higher than that of intact salt; it will exhibit directional dependence; it will depend on distance from the mined opening; and it will vary in time as fractures undergo stress-induced healing (Beauheim and Roberts, 2002; Hansen and Leigh, 2011; Pfeifle and Hurtado, 1998). Healing of fractures in salt at high temperature and the role of water in facilitating healing and crushed salt consolidation must be understood at a basic level in order to provide confidence in numerical models of the hydrological properties of the DRZ, which are critical to quantifying fluid fluxes in the waste canister area. At ambient temperatures, creep, dilation, and shear lead to an increase in fracture permeability in the DRZ from a pre-mining condition of essentially impermeable, intact salt (Pfeifle and Hurtado, 1998; Van Sambeek et al., 1993; Holcomb and Hardy, 2001). Over time, salt creep will result in closure of the mined opening and healing of the fractures in the damaged zone, presumably at rates that are dramatically greater at elevated temperature (Hansen and Leigh, 2011). In short, the interplay of these various processes, especially water liberation and migration, is currently unknown and requires further study.

This report is organized as follows. We begin by presenting a summary of the coupled processes that are used in the simulations, including new algorithms implemented in FEHM specifically for this project (e.g., porosity change as salt dissolves and/or precipitates, water vapor pressure as a function of both salt concentration and temperature). Next, benchmarking exercises are presented that compare simulation results to recent LANL experiments on the thermal behavior of salt and water release from clay dehydration (FY13), as well as1980's era non-heated and heated experimental data from WIPP.

Next, the numerical model is used to make predictions of temperatures, porosity changes, and saturations that may occur for waste emplaced using the in-drift concept. These simulations are presented in order of increasing complexity, from thermal (T), to thermal-hydrologic (TH), to thermal-hydrologic-chemical (THC) in order to illustrate the relative importance of each process. These calculations are presented in the context of a future field test, and include, the most complex analyses, full THC calculations with initial results from clay dehydration simulations. Next, uncertainties in parameters such as initial saturation, depth of RoM backfill, and thermal diffusivity of drift air are addressed through uncertainty analyses for a generic salt repository. The report with chapters that begin the process of linking small scale observations of fluid inclusion migration to recent LANL experiments, and a brief discussion of the impacts of stress on short term calculations of heat and fluid flow.

2. Modeling Capabilities and Enhancements in FEHM for Salt

The Finite Element Heat and Mass Transfer Code, FEHM, has been developed by LANL for more than 30 years (Zyvoloski, 2007). The code started as a tool to simulate geothermal reservoirs as part of LANL's groundbreaking Hot Dry Rock geothermal energy program (Kelkar et al., 2011), but has grown over the years to include unsaturated flow, reactive chemistry, stress, and carbon dioxide (https://fehm.lanl.gov). FEHM has been used in research studies in more than 100 peer reviewed publications (FEHM 2012). FEHM uses a finite volume method for solving multiphase flow and transport, while using a finite element formulation for the fully coupled stress solutions. Capabilities pertinent to the salt simulations presented in this report include the ability to run fully coupled heat and mass transfer on both 2-D radial and 3-D numerical meshes. We also make use of the reactive chemistry module of FEHM, allowing us to modify porosity caused by dissolution and precipitation and explore mineral dehydration reactions including associated release of water during heating. In the rest of this chapter, we describe additions to FEHM allowing simulation of fully coupled THC processes in salt. These additions to the code make FEHM uniquely capable for addressing the questions concerning water migration during the SDDI heater test.

In the FEHM simulations presented, we ignore the large-scale deformation processes due to salt creep that will dramatically impact the long-term process of the sealing of the repository. Therefore, our results are relevant to the initial evolution of the thermal regime and water transport processes during the initial heat-up of the repository. A firm understanding of these processes is required to enable better prediction of the long-term behavior of the system. For example, if the presence of water has an impact on salt fracture healing and crushed salt consolidation, then characterization of the water balance in the drift and surrounding salt will be required. Also, the short-term evolution of the repository near field impacts the degradation of engineered systems such as the waste package, making it important to understand the conditions of the repository system in the period before permanent closure.

In the subsections that follow, the constitutive relationships and other model issues specific to the modeling the thermal, hydrologic, and chemical behavior of a salt repository are described.

2.1 Thermal Conductivity of Salt as a Function of Porosity and Temperature

Thermal conductivity of salt can change dramatically with changes in porosity and temperature. Munson et al. (1990) investigated the temperature dependence of the thermal conductivity (k_t [W/m/K]) of intact salt at the Waste Isolation Pilot Plant (WIPP), identifying the following relationship:

$$k_{t-WIPP}(\mathrm{T}) = k_{t-300}\left(\frac{300}{\mathrm{T}}\right)^{1.14} \quad (1)$$

where k_{t-300} is the thermal conductivity at 300 K (5.4 W/m/K) and T is temperature in Kelvin (K); this relationship is used for the thermal conductivity of intact salt in this study.

Bechthold et al. (2004) investigated the dependence of thermal conductivity on porosity ϕ of run-of-mine salt at the Asse salt mine in Germany. They developed the following relationship fitting the thermal conductivity of run-of-mine salt to porosity (ϕ) using the following fourth-order polynomial:

$$K_{T-ASSE}(\phi) = -270\phi^4 + 370\phi^3 - 136\phi^2 + 1.5\phi + 5 \quad (2)$$

In order to combine the findings of Munson et al. (1989) and Bechthold et al. (2004), K_{T-ASSE} has been scaled to match K_{T-300} at f=0 as

$$K_{T-300}(\phi) = \left(\frac{K_{T-300}}{K_{T-ASSE}(\phi=0)}\right) * K_{T-ASSE}(\phi) \quad (3)$$

where $K_{T-300}/K_{T-ASSE}(f = 0)$ is 5.4/5.0, or 1.08. Equations 1 and 2 have been derived using data from domal and bedded salt formations, respectively. The relationship of thermal conductivity to temperature and porosity may not be the same in these formations. The combination of equations 1 and 2 allows the available information on salt thermal properties to be incorporated in this generic salt repository study, while further experimental investigations are still needed. Following Clayton and Gable (2009), the assumption has been made here that run-of-mine salt has the same temperature dependence as intact salt, giving

$$K_{T-crushed}(\mathrm{T}, \phi) = K_{T-300}(\phi)\left(\frac{300}{\mathrm{T}}\right)^{1.14}. \quad (4)$$

(5)

These equations have been implemented in FEHM.

2.2 Salt solubility as a function of temperature

The solubility of salt is calculated in FEHM by a simple function shown in Figure 1, derived from Sparrow (2003).

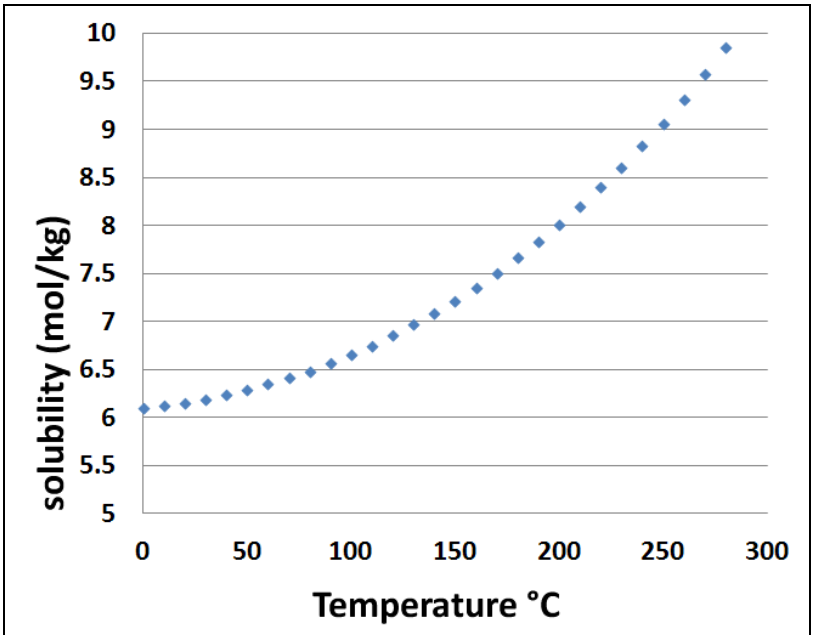

Figure 1: Salt solubility in water as a function of temperature, calculated from functions in Sparrow (2003).

Solubility is quite important in the coupled THC simulations because as temperature rises, the water is able to dissolve more salt, leading to higher porosity and permeability while simultaneously lowering thermal conductivity and water vapor pressure.

2.3 Precipitation/Dissolution of Salt

In this model, precipitation and dissolution reactions of NaCl result in changes in the porosity of the salt medium. Precipitation and dissolution are explicitly coupled to the heat and mass transfer solution through feebacks on porosity, permeability, thermal conductivity, and vapor pressure. Changes in porosity ($\Delta\,\phi$) are calculated at each node after each chemistry iteration as:

$$\Delta\phi_i = \Delta c \rho_s m_s \frac{1}{\rho_{NaCl}}(1-\phi_i), \tag{6}$$

where $\Delta c = c_i - c_{i-1}$ is the change in the moles of solid NaCl per weight of the solid [kg], ρ_s is density of the solid [kg/m^3], m_s is the molar mass of NaCl [kg/mol], ρ_{NaCl} is the density of NaCl [kg/m^3], and i is a solute transport solution iteration index. We further assume, $\rho_s = \rho_{NaCl}$.

2.4 Water vapor diffusion coefficient as a function of pressure, temperature, and porosity

Water vapor diffusion is modified to account for thermal and pressure effects through the following equation (modified from Zyvoloski et al., 1997).

$$D_{va} = \tau D_{va}^{o} (P_o/P) ((T+T_o)/T_o)^{\theta} \quad (7)$$

where τ = tortuosity, $D_{va}^{o} = 2.23 \times 10^{-5}$, To = 273.15 K, $\theta = 1.81$, T = temperature in C, P = pressure in MPa, and $P_o = 0.1$ MPa. The effective free air water vapor diffusion coefficient is then modified using the Millington Quirk relationship where tortuosity (τ) is calculated as:

$$\tau = (S_v * \phi)^{2.333} / \phi^{2} \quad (8)$$

where S_v = air saturation. The resulting vapor diffusion coefficient is implemented in the mass transport equation for diffusion of water vapor through air driven by a concentration gradient in the bulk vapor phase (air + water vapor) as:

$$mf_{wv} = -D_{va} \varphi S_v MW_{wv} \nabla C_{wv} \quad (9)$$

where mf_{wv} = mass flux of water vapor, MW_{wv} = molecular weight of water vapor (kg/mol) and C_{wv} = moles of water vapor per cubic meter of air. In Equation (9), mf_{wv} reduces to units of kg/(m^2 s).

2.5 Capillary pressure relationships

Limited data on the capillary pressure of granular salt versus saturation are available in the literature, and we rely on Cinar et al. (2006) to guide our choice of which capillary pressure values to use in our simulations. As seen in Figure 2, the measured data for granular salt suggest capillary suction of greater than 0.5 MPa at dry conditions. RoM salt is comprised of grains ranging from sub millimeter scale to cobble sized chunks; we have developed three capillary pressure functions that span uncertainty in this function. All of these functions are linear, with suction at zero saturation defined to be 0.2, 0.5 or 1.0 MPa for the three cases; suction at full saturation is equal to zero for each case. Although the cases are unequal in their ability to match the data at the wet end of the curves (S > 0.2), for the low end of saturation (<0.2 MPa), the range most relevant to these simulations, these three functions lie across the measured data.

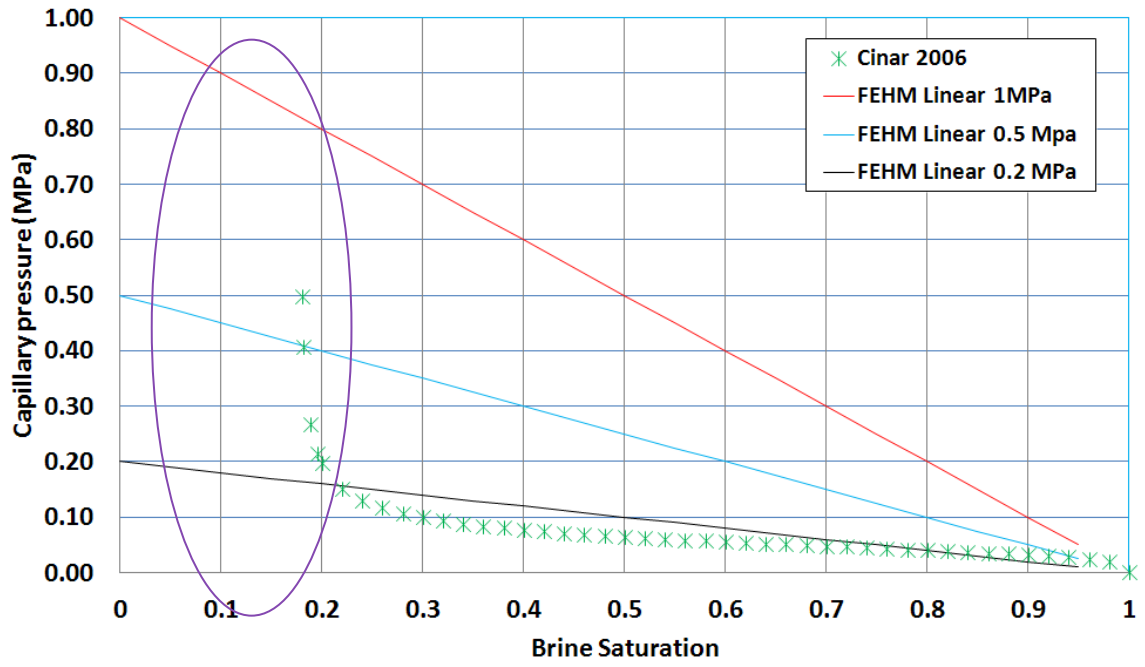

Note: The purple oval is the region most applicable to the range of saturations found in the RoM salt in the simulations.

Figure 2: Capillary pressure versus saturation after Figure 5 in Cinar et al. (2006).

2.6 Permeability-Porosity Relationship for RoM Salt

Cinar et al. (2006) identified a permeability-porosity relationship based on measurements of compacted pure sodium chloride. A generalized form of this relationship was implemented into FEHM as

$$k = \begin{cases} c_1 \phi_l^{\,c_2} & if\ \phi \le \phi_l \\ c_1 \phi^{c_2} & if\ \phi_l \le \phi \le \phi_u \\ c_1 \phi_u^{\,c_2} & if\ \phi \ge \phi_u \end{cases} \quad (10)$$

where k is permeability (m^2), ϕ_l and ϕ_u are the upper and lower porosity limits for the relationship, respectively, and c_1 and c_2 are fitting parameters.

The user specifies the upper and lower porosity limits and fitting parameters. For the simulations presented here, the values of c_1 and c_2 from Cinar et al. (2006) of 4.866×10^{-9} and 4.637, respectively, are used (refer to Figure 3). The upper and lower limits were set to 0.2 and 1×10^{-6}, respectively. This lower limit is an extrapolation beyond the data presented in Cinar et al. (2006). This model does not include the compaction of RoM salt, but instead simulates only the dissolution and precipitation of NaCl, for which it is assumed that the relationship depicted in Figure 3 is valid.

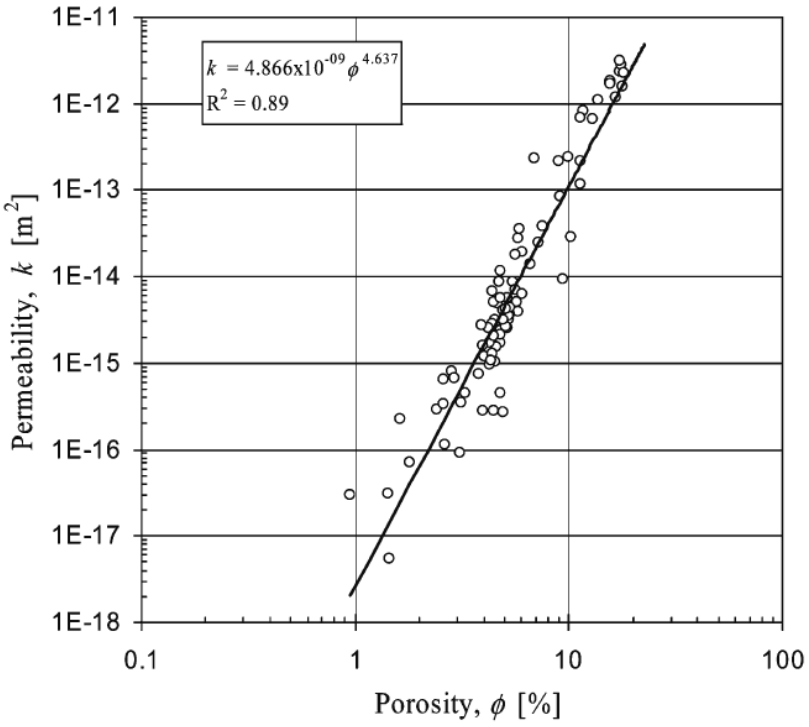

Figure 3: Permeability/porosity data and trend line from Figure 6 in Cinar et al. (2006)

2.7 Vapor Pressure of Water as a function of Aqueous Sodium Chloride Concentration and Temperature

The vapor pressure of water depends on the dissolved salt concentration, with higher concentrations resulting in lowered vapor pressures. Sparrow (2003) developed polynomial equations relating vapor pressure (P_v) to the salt mass fraction and temperature.

These equations are valid near the saturation pressure of the solution and for temperatures within 0 and 300°C. The equations take the form

$$P_v = A + BT + CT^2 + DT^3 + ET^4 \quad (11)$$

where T is temperature in °C and A, B, C, D, and E are 4th order polynomials of salt mass fraction (refer to Sparrow (2003) for details). Figure 4, taken without permission from Sparrow (2003), presents vapor pressure as a function of salt mass fraction and temperature. These equations, truncated at 300°C, have been implemented in FEHM.

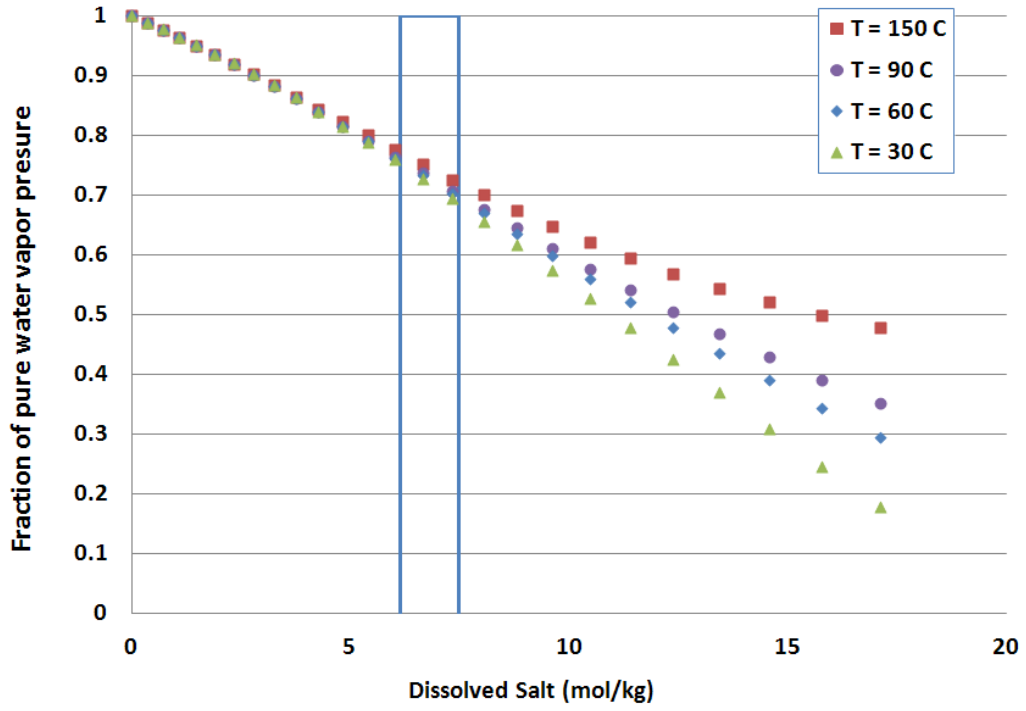

Note: The blue vertical lines span the region of interest for most of our simulations (30 °C to 170 °C).

Figure 4: Water vapor pressure (expressed as the fraction of the pure water value) as a function of dissolved salt and temperature, based on functions in Sparrow (2003).

2.8 Approximating Heat Transfer across the Air Gap

Heat transfer in the region between the RoM salt and the drift wall or roof is controlled by a combination of conductive, convective, and radiative heat transfer. Because the modeling codes being used focus on porous media, approximations are required to capture these heat transfer processes. In our simulations, the air gap is modeled as a porous medium with high porosity (~0.999) and permeability (~1x10^{-11} m^2). Convective and radiative contributions to heat transfer are approximated using an effective thermal conductivity. The next three subsections describe the process for establishing the thermal properties to properly account for convective and radiative effects.

2.9 Convective Heat Transfer Across Air Gap

To determine the effective thermal conductivity that incorporates convective effects, the first step is to determine the Rayleigh (Ra) and Prandtl (Pr) numbers as

$$\mathrm{Ra} = \frac{g\beta(T_h - T_c)H^3}{\alpha\upsilon} \tag{12}$$

and

$$\mathrm{Pr} = \frac{\nu}{\alpha} \tag{13}$$

where g is the acceleration due to gravity, β is the thermal expansion coefficient, T_h is the temperature at the top of the mine-run salt, T_c is the temperature of the roof of the adit, H is the height of the air gap, α is the thermal diffusivity, and ν is the kinematic viscosity.

The Nusselt number (Nu), which describes the ratio of conductive and convective heat transfer to conductive only heat transfer, can be approximated for an enclosure heated from below (Bejan, 1995) as

$$\mathrm{Nu} = 0.069\mathrm{Ra}^{1/3}\mathrm{Pr}^{0.074},\ 3\mathrm{x}10^5 < \mathrm{Ra} < 7\mathrm{x}10^9 \quad (14)$$

Figure 5 plots this correlation with the valid range in red. Due to the geometry and temperature differences across the air gap, the Rayleigh numbers extend beyond the valid range of the correlation, and an extrapolation is required. Using the definition of Nu as the ratio of conductive/convective heat transfer to conductive heat transfer, the effective thermal conductivity can be approximated as

$$k_{c,eff} = \mathrm{Nu} * k_{t,a} \quad (15)$$

where $k_{t,a}$ is the thermal conductivity of air (0.03 W/m*K; Bejan, 1995).

Figure 6 presents the $k_{c,eff}$ for a 4 ft air gap as a function of the temperature difference across the air gap. A potential minimum $k_{c,eff}$ for an air gap of 2 ft with a ΔT ($T_h - T_c$) of 1 K is about 2.6 W/m*K, while a potential maximum for an air gap of 6 ft and a ΔT of 30 K is around 8.3 W/m*K.

In the simulations presented here, a constant $k_{c,eff}$ is used for the air gap. This is assumed to be a reasonable approximation given the small variations due to changes in ΔT.

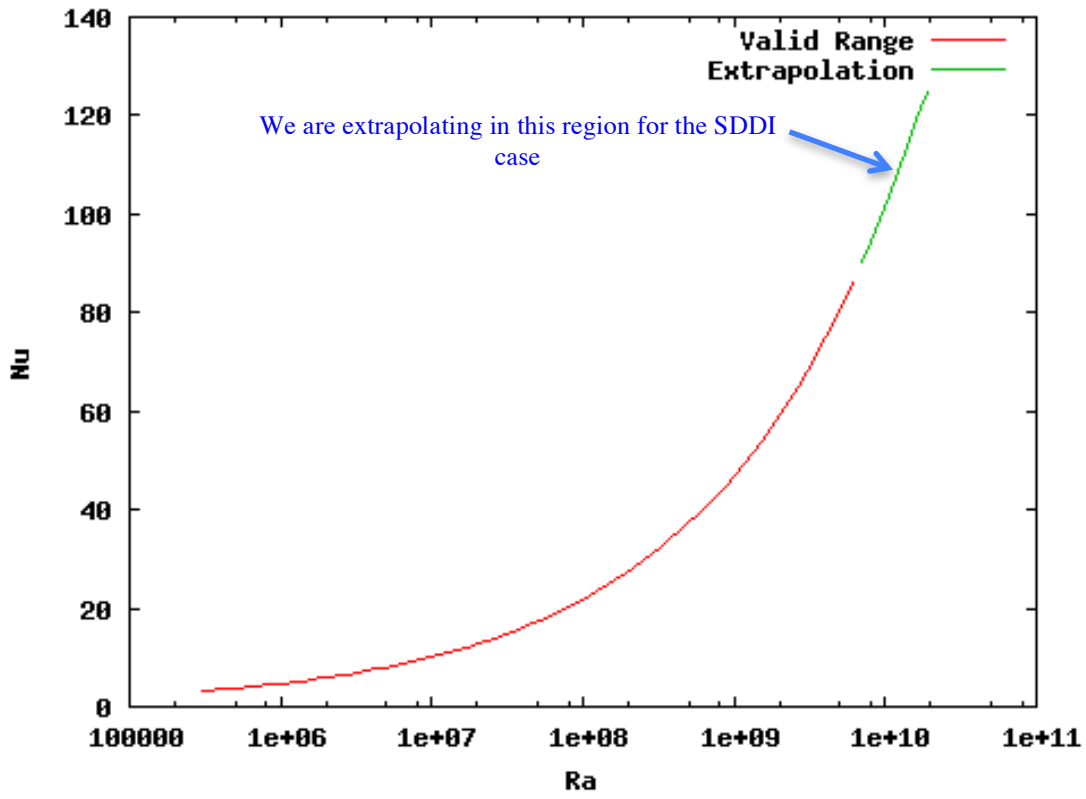

Figure 5: Rayleigh-Nusselt correlation for enclosures heated from below (Equation 14).

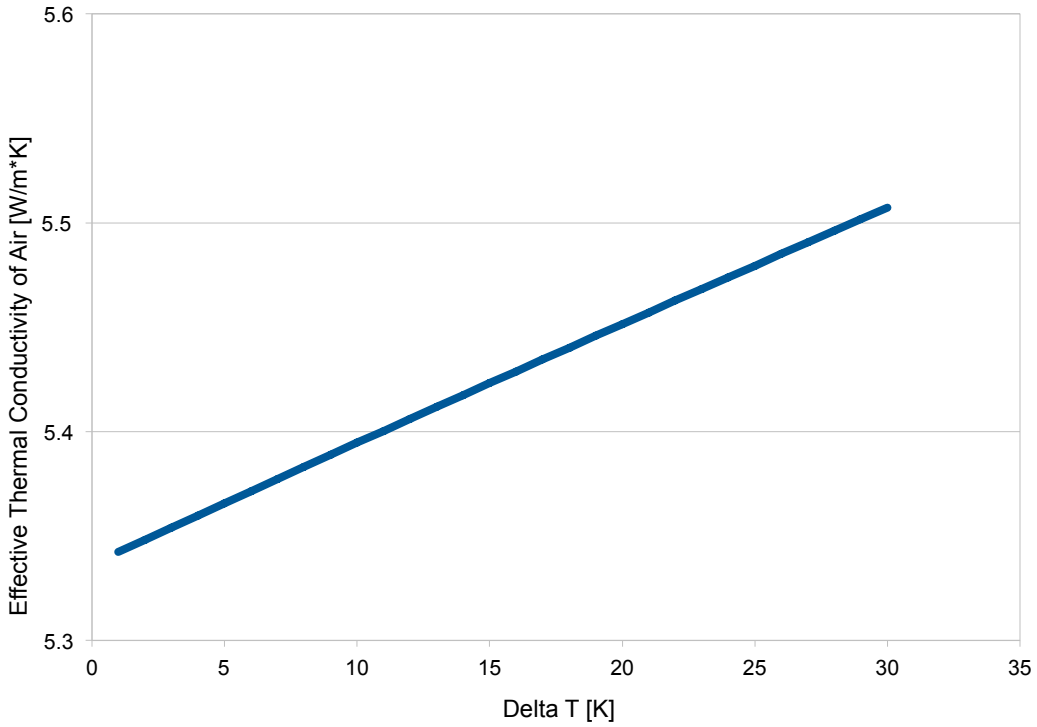

Figure 6: Effective thermal conductivity of air in a 4 ft air gap incorporating convective heat transfer effects as a function of the temperature difference across the air gap.

2.10 Radiative Heat Transfer across Air Gap

A term for radiative heat transfer in air was calculated assuming infinite parallel plates at temperatures T_h (mine-run salt pile) and T_2 (ceiling of adit) across a range of temperatures, although more accurate shape factors could be calculated for the crushed salt pile and the surrounding walls. For parallel plates, if the emissivities of the materials are ε_1 and ε_2 for the crushed salt and walls, respectively, the effective emissivity is (Incropera and Dewitt, 1985):

$$\varepsilon_{eff} = \frac{1}{\frac{1}{\varepsilon_1}+\frac{1}{\varepsilon_2}-1} \tag{16}$$

While the emissivities of the crushed salt and walls will differ, a lack of experimental data on radiative properties of salt leads to the selection of $\varepsilon_1 = \varepsilon_2$ across a range of values: 0.65 (Svalstad, 1983) to 0.9 (published value for sand; Incropera and Dewitt, 1985).

Radiative flux is then given by

$$J_{rad} = \varepsilon_{eff}\sigma(T_h^4 - T_c^4) \tag{17}$$

where σ is the Stefan-Boltzmann constant (5.67 x 10^{-8} W/m^2*K^4) and temperatures are in Kelvin. An effective thermal conductivity for radiative transfer, k_r (W/m*K), analogous to $k_{t,a}$ for conduction and $k_{c,eff}$ for conduction plus convection, was calculated using

$$k_{\mathrm{r,eff}} = \frac{J_{rad} d}{(T_h - T_c)} \tag{18}$$

where d is the distance across the air gap (4 ft). Figure 7 shows $k_{r,eff}$ for radiative transfer in air for a variety of salt emissivities, for a fixed RoM salt temperature of T_h = 100°C and ceiling temperatures ranging from T_c = 25°C to 100°C. To approximate the radiative heat transfer effect, a fixed value of 8.6 W/m*K was selected as an approximation, but the code could be updated to compute a transient effective thermal conductivity due to radiative transfer as the temperatures of the walls and crushed rock change.

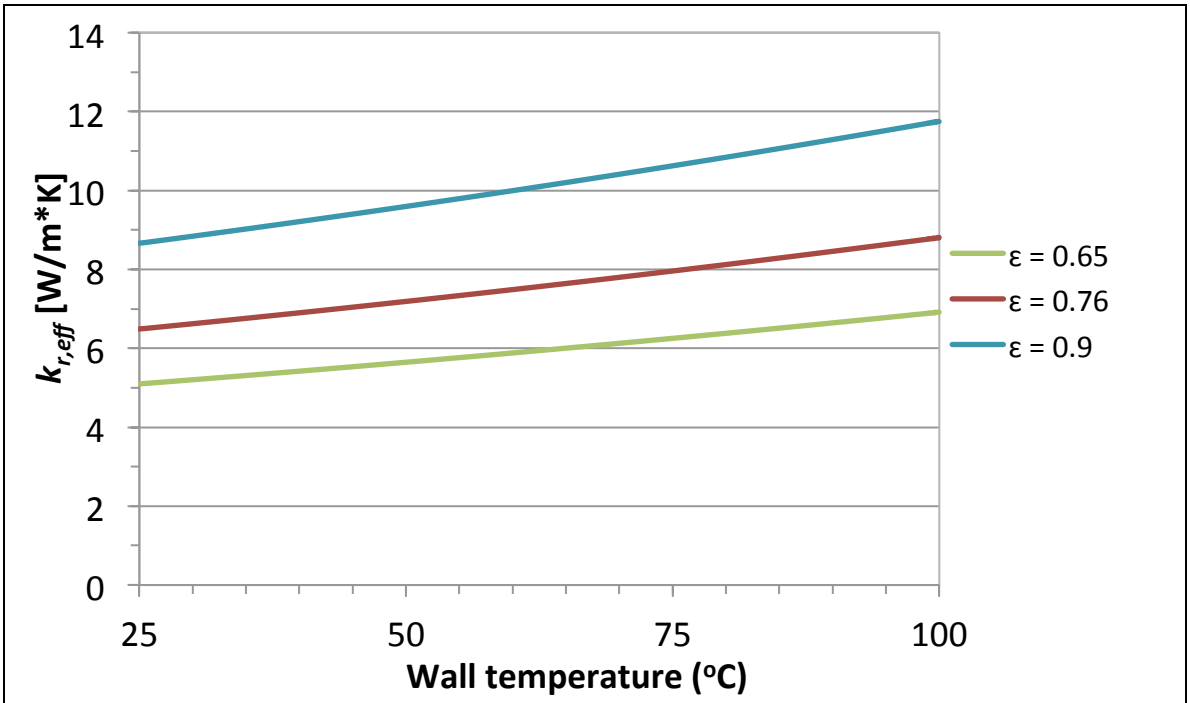

Figure 7: Effective thermal conductivity of air due to radiative heat transfer as a function of wall temperature, assuming a fixed crushed salt temperature of 100°C.

2.11 Superposition of Conductive, Convective, and Radiative Effective Thermal Conductivities

As radiative transfer occurs in parallel with convection and conduction, the radiative transfer term may be added to the contribution from convection and conduction to form a combined effective conductivity (Kreith and Bohn, 1997):

$$k_{t,\mathrm{eff}} = k_{c,\mathrm{eff}} + k_{r,\mathrm{eff}} \tag{19}$$

The constant combined effective conductivity of air as implemented in FEHM is $k_{t,eff}$ = 14 W/m*K.

2.12 Clay Dehydration

Hydrous mineral dehydration reactions have the possibility of impacting the evolution and transport of water in a salt repository, so models must be developed to capture these effects, including the temperature-dependent introduction of water into the pore space, where it is available to transport nad react with the solid salt. FEHM has been previously used to estimate the dehydration of zeolites for the Yucca Mountain project. Based on that initial code development, the code was modified in the present study to provide a water source from dehydration of clay impurities in salt, based on preliminary experimental data from WIPP samples with varying clay content. The current implementation will be improved in the future, but as a first cut, the impact of water production on heat transport and temperature distributions can be studied.

The experiment upon which the clay dehydration model is based is described in greater detail in Caporuscio et al. (2013). Samples of known clay content (weight percent) were heated at constant temperature (64^{o}C) and periodically weighed until their masses stabilized after approximately 40 hours of heating. The temperature was then raised to 110^{o}C and maintained until mass loss again ceased (24 hours). A temperature increase to 165^{o}C produced little additional mass loss in most samples after 10 hours. The temperature was raised to 264^{o}C and the procedure was repeated (90 hours to mass stabilization).

The mass of water lost as a percentage of clay mass varied slightly with total weight percent clay, but averages were used in the clay dehydration model developed herein (Figure 8). Although the progression appears linear, because the temperature profile between the chosen temperature steps is not known, the model developed here uses a simple stair-step function of water loss with temperature. For now, it reflects the limited information provided by this experiment, but it will be updated as additional information becomes available. In particular, water loss below 64^{o}C may be an important source in some regions of the heater test model.

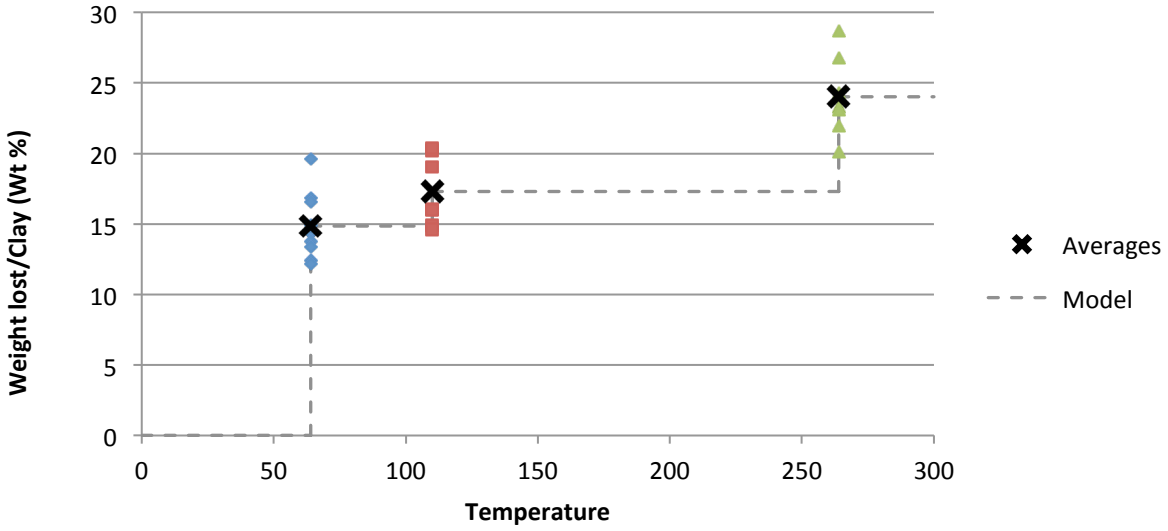

Note: The clay dehydration model is a stepwise function that produces all the water loss when the model reaches the temperatures indicated (64, 110, and 264°C).

Figure 8: Weight lost as a percentage of clay weight during a phased heating experiment.

As implemented in FEHM, the clay dehydration model can be applied to selected nodes or zones within the model, and differing clay fractions can be specified. Based on the experimental information available, at 64°C, 14.8% of the mass of clay in the node is added as a source term in a one-time release. At 110°C, 2.5% of the clay mass is released, and at 264°C, an additional 6.7% is released. For a given node for which the clay dehydration is invoked, for a specified clay mass fraction f_c, the mass of water produced at 64°C is given by

$$M_w = 0.148\, f_c\, (1 - f_i)\, \rho_c\, V_{cell} \tag{20}$$

where f_i is the initial porosity of the node, ρ_c is the density of clay, and V_{cell} is the volume of the node. The water mass production for the second and third clay dehydration temperatures follows similarly.

The implementation of dehydration in FEHM was tested by running a 6-node model of composed of crushed salt with many of the same relevant physical processes as the full model. One test problem assumed initial temperatures of 30°C everywhere except at node 1, which had initial temperature 115°C, and was held at this value. Nodes 4, 5, and 6 contained 10% clay, while nodes 1, 2, and 3 contained no clay. The saturation, temperature, and water vapor partial pressure as a function of time for this 6-node problem are shown in Figure 9. Total water production was correct to within 2% of the expected amount for all test cases, with many cases correct to within 0.5%.

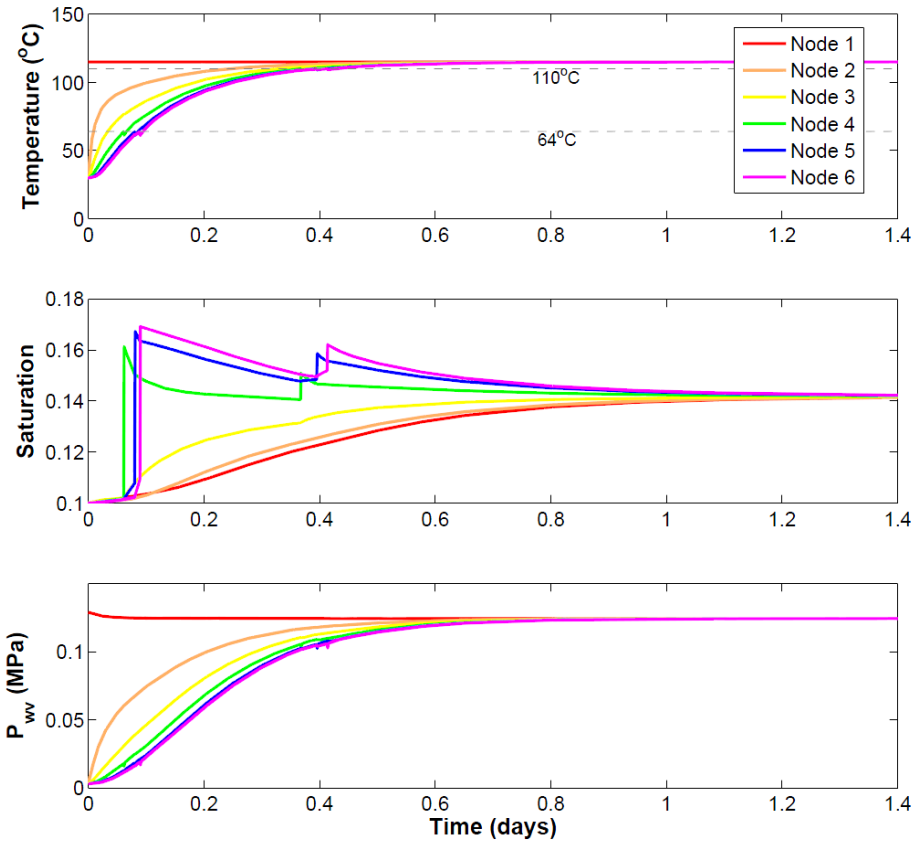

Note: nodes 1, 2, and 3 contain no clay. Nodes 4, 5, and 6 contain 10% clay and release water when they reach 64 and 110°C.

Figure 9: Temperature, saturation, and partial pressure of water vapor for the 6-node problem.

As temperature rises, saturation also rises due to the thermal expansion of water. Water vapor partial pressure rises due to the increase in water vapor saturation pressure with temperature. In this 6-node no-flow problem, nodes 4, 5, and 6 are already saturated with respect to water vapor during the 110°C transition, so although the transition occurs above boiling, the liquid saturation increases.

The current clay dehydration model does not distinguish between water released by clay dehydration and that produced by other bound water sources such as fluid inclusion migration to a grain boundary. In the future, it is possible that all crushed salt nodes will utilize the "clay dehydration" model to release water from fluid inclusions. In the low-porosity intact salt, water production might raise fluid pressures and influence hydraulic fracturing. On the other hand, water production in intact salt will be most significant at the clay seams, where shrinkage could occur during dehydration, producing additional porosity for the produced water. These issues will be the subject of future work.

2.13 Implementation of variable property diagnostics in FEHM output

To ensure that the simulations are properly accounting for the many new variable properties, a new output reporting feature was implemented in FEHM in both the output file and in the screen output. For example, Table 1 shows a row of nodes going from the top of the mesh, to the top of the adit, into the RoM backfill, the heater, into the floor of the adit, and finally to the bottom of the mesh at node 21. Permeability, porosity, x component of thermal conductivity, water vapor pressure, water vapor diffusion coefficient, and the change in porosity due reaction is reported at each of these nodes. The output indicates that the thermal conductivity function is indeed keeping "Kx" fixed at 14.0 W/(m K) in the adit air and 1.1 W/(m K) in the waste canisters, while allowing "Kx" to change in the rest of the domain. This new output has been invaluable in ensuring that our many constitutive relationships are performing as expected.

Table 1: New screen output from FEHM

```
 - - - - - - - - - - - - - - - - - - - - - - - - - - - - - - - - - - - - - - - -

   Node    perm (m2)     porosity     Kx W/(m K)    Pwv (MPa)      D*wv (m2/s)   ps_delta_rxn
  117495   0.10000E-20   0.10000E-02    5.3361      0.31557E-02    0.10629E-12     0.0000
  102233   0.10000E-18   0.10000E-01    5.0982      0.64491E-02    0.87686E-09    0.29872E-11
   85866   0.10000E-10   0.99900        14.000      0.80089E-02    0.28997E-04     0.0000
   70134   0.27929E-11   0.48402       0.57114      0.19505E-01    0.19459E-04    0.39003E-05
   54963   0.15400E-17   0.89400E-02    4.0922      0.10769        0.79177E-05     0.0000
   43160   0.88841E-17   0.13046E-01    3.9657      0.10906        0.93052E-05     0.0000
   39022   0.10000E-20   0.10000E-04    1.1000      0.11204        0.88788E-06     0.0000
   34337   0.10000E-20   0.10000E-04    1.1000      0.11307        0.90078E-06     0.0000
   15980   0.10000E-20   0.10000E-04    1.1000      0.84381E-01    0.86175E-06     0.0000
   10667   0.10000E-18   0.10000E-01    4.2656      0.64085E-01    0.39347E-05   -0.91248E-07
    3612   0.10000E-18   0.10000E-01    4.3988      0.44300E-01    0.23626E-05    0.11403E-07
    2639   0.10000E-20   0.10000E-02    4.8613      0.12512E-01    0.56724E-08     0.0000
      21   0.10000E-20   0.10000E-02    5.3361      0.31560E-02    0.24695E-13     0.0000
```

3. Benchmarking

The following sections present simulations compared to data from both historic field tests and recent laboratory experiments at LANL. The field test section starts with isothermal simulations designed to show that the model is adequately capturing the process of water entry into the drift in the absence of heat. Next, a set of heated examples are presented to show that the model properly reporesents the heated case. For the heated cases, results are also presented examining the sensitivity to DRZ permeability. Finally, results are presented from three laboratory experiments using dry salt that confirm the thermal conductivity model described in section 2.1.

3.1 Three-dimensional fine resolution simulations

In this section, simulations for non-heated and heated boreholes are compared to analytical solutions and field-scale observations to ensure that the processes controlling water migration toward an excavated opening are adequately captured.

3.1.1 Non-heated cases

In the first test case, we consider a three-dimensional domain located about 600m below the ground surface. The domain contains an evacuated tunnel-shape space of 2.438m×3.04m×20m. The excavation damaged zone (EDZ) was not included in this simulation because of uncertainty of the parameters (such as thickness and permeability) of the EDZ. The initial pressure head was set to 6MPa (which is the hydrostatic pressure) everywhere except in the open space where the air pressure and the water pressure were fixed to 0.11MPa and 0.1MPa, respectively. The water saturation in the air was set to 1e-6 (Note: Absolute humidity in air ranges from zero to roughly 30 grams per cubic meter when the air is saturated at 30 °C, which is equivalent to saturation of 3×10^{-5}). The water flow into this open space for the first 14 days is plotted in Figure 10.

For this simplified case, the steady state flow in deep tunnel without heating can be estimated using simple solution (Polubarinnova-Kochina, 1962):

$$q = \frac{2\pi K(d-\phi_0)}{\ln(2D/R)} \tag{21}$$

where K is the hydraulic conductivity (m/day), R is the tunnel radius (m), D is the depth of the tunnel (m), ϕ_0 is the head at the tunnel perimeter (m), d is the water depth above the ground surface, and q (m^3/day/m) is the flow rate per unit length of the tunnel. At the depth of about 600 m, the impact of the orientation of a short borehole is not significant and thus this equation can be used to approximate the steady water flow to the borehole. Given K = 8.43×10^{-9} m/day (converted from permeability 1×10^{-20} m^2), R=0.38m, D =600

m, $\phi_0 = -600$ m, and d =0, a value of $q = 3.94\times10^{-6}$ m^2/day is obtained. The total flow rate Q to the borehole of length of 3.1m will be $Q = 3.1q = 1.22\times10^{-5}$ m^3/day, or 12.2 g/day, which is very similar to the recorded values.

The FEHM simulation lasts for 14 days. The flow rate from the FEHM model as a function of time is plotted in Figure 10, where the flow rate from this simulation has been scaled because the open space in the flow simulation domain is different from the borehole. For the open space in the simulation, it may be approximated as of a tunnel of radius R=1.52m and length of 20 m. The water flow per unit length of tunnel can be calculated using the above equation as $q = 4.75\times10^{-6}$ m^2/day, and the total flow rate Q = 20q = 95 g/day, or 1.1×10^{-6} kg/s, which is similar to the simulated value of 0.98×10^{-6} kg/s. We should emphasize that from the equation the flow rate q should be using the equivalent radius but not the cross-sectional area of the tunnel.

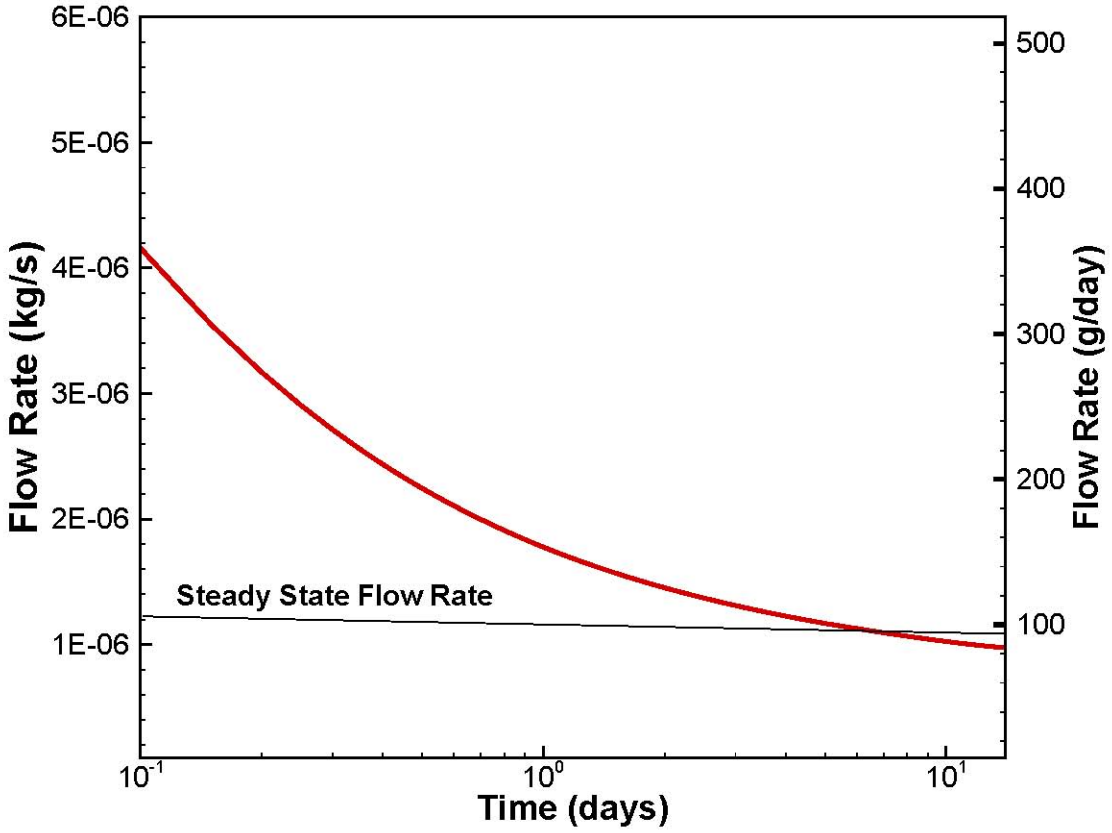

Figure 10: Scaled Water Flow Rate

The second example was adapted from Christian-Frear and Freeze (1997), who presented a site-specific example with damaged zones at the Waste Isolation Pilot Plant (WIPP). A large-scale

experiment was designed to gain insight into the flow processes around the WIPP underground excavation. The experiment room, Room Q, is a 109 m long cylindrical room with a 1.45m radius that was drilled horizontally in the WIPP underground, as illustrated in Figure 11. Following excavation, the room was instrumented for geochemical and hydrological measurements and sealed to prevent evaporative losses. Data were collected from inside the sealed room over a six-year period. The brine accumulation was not seen for the first two years following excavation, possibly because of evaporation from the wall due to ineffective seals at the entrance of the room. The damaged zone extended 0.55m from the wall of the room. There is a significant pressure gradient from the far-field (12.5 MPa at the distance of 49.68m) to the room at 0.1MPa. The permeability values for the damaged zone and the far-field rock are taken to be 1×10^{-15} m^2 and 1×10^{-21} m^2, respectively. The Brooks-Corey constitutive model was used to describe the relationship between the relative permeability and capillary pressure, with a threshold pressure of 0.087MPa and the pore-size distribution parameter of 0.7.

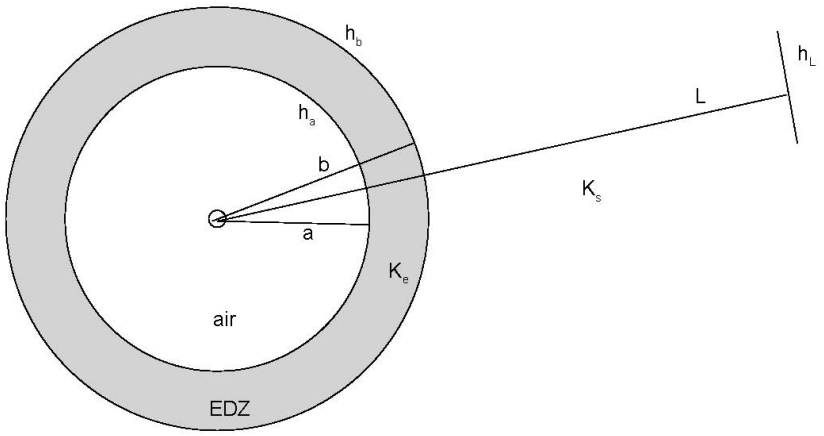

Figure 11: Upper and lower boundaries in numerical model

In our numerical model, the room is not exactly cylindrical in shape, but the effective radius is about 1.5m (which is close to 1.45m for Room Q), and the width of the damaged zone is 2ft (0.61m).

The upper and lower boundaries in the numerical model are located at z = ±20m. Therefore, the far-field boundary condition of 12.5 MPa may not directly apply to our boundaries. The equivalent boundary value

may be derived as follows. For a cross-section as illustrated in Figure 11, the flow rate through the circle of radius r = a can be approximated as:

$$Q_a = 2\pi K_e \frac{h_b - h_a}{\ln(b/a)} \tag{22}$$

where h_a and h_b are respectively the head at the wall (r = a) and the interface (r = b) between the EDZ and the intact salt. Similarly,

$$Q_b = 2\pi K_s \frac{h_L - h_b}{\ln(L/b)} \tag{23}$$

Since these flow rates must be the same, the following equation is derived:

$$\frac{h_L - h_b}{h_b - h_a} = \frac{K_e}{K_s}\frac{\ln(L/b)}{\ln(b/a)} \tag{24}$$

Or equivalently,

$$\frac{h_L - h_a}{h_b - h_a} = 1 + \frac{K_e}{K_s}\frac{\ln(L/b)}{\ln(b/a)} \tag{25}$$

For given h_L = 12.5 MPa at L = 49.68m, we can calculate h_b from this equation. In order to maintain the same flow rate at the wall, h_b must be held constant. If L = 20m, the pressure at the boundary can be determined from this equation as 8.99MPa. The results of two simulations with constant boundary pressure of 12.5MPa and 8.99MPa are presented in Figure 12. In both cases, the permeability of the EDZ has been assigned to 10^{-19} m^2.

The steady state flow rate can be calculated from either Equation (22) or (23), or can be rewritten by solving h_b - h_a from Equation (25), followed by substitution into Equation (22):

$$Q_a = 2\pi\left(h_L - h_a\right)\frac{K_e K_s}{K_e \ln(L/b) + K_s \ln(b/a)} \tag{26}$$

From this expression, it follows that the permeability of EDZ does not have a significant impact on the steady flow rate because L/b is much larger than b/a. The calculated flow rate based on the chosen parameter values is 227 mL/day, which is about twice the simulated values. This is reasonable agreement, given the fact that there are some uncertainties and differences between the numerical simulations and reality, such as the numerical grid (parallelogram shaped domain instead of cylindrical domain) and the uncertain width of the EDZ.

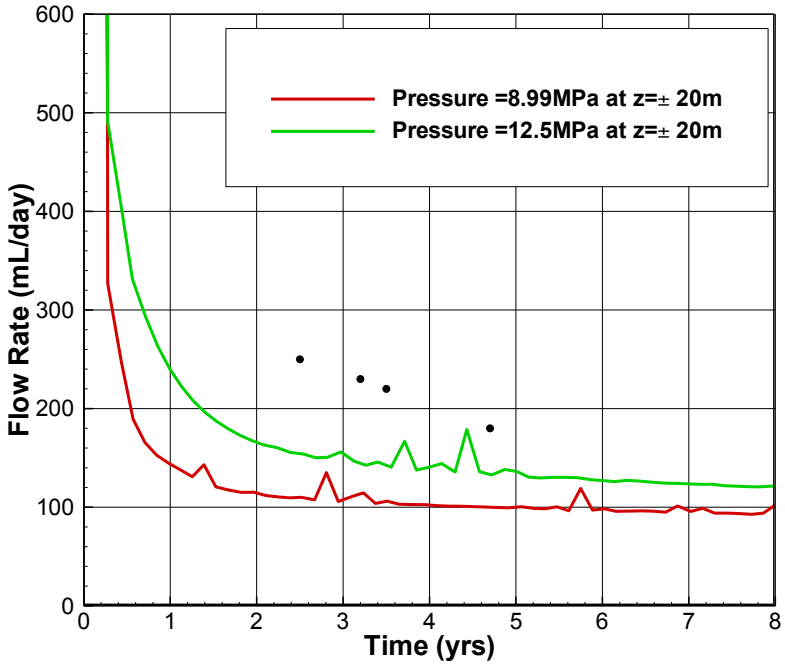

Figure 12: Computed flow rate versus time, compared to data collected from Room Q at WIPP.

3.1.2 The effect of excavation damaged zone

We conducted a series of FEHM simulations to investigate the effect of the EDZ on the water flow into the drift by either varying the width of the EDZ at a fixed EDZ permeability of 10^{-17} m^2 or varying the EDZ permeability at a fixed EDZ width of 5ft. In both cases, the permeability of the intact salt is fixed at 10^{-20} m^2, while the porosity of the EDZ is taken as 0.01, which is 10 times the porosity of the intact salt. The results are illustrated in Figures 13 and 14.

As expected, when the EDZ has a high permeability, the early-time water flow rate into the drift will be high, but the rate then decreases quickly, which yields a crossover between the curves of different values of EDZ permeability. Such a decrease in the flow rate is partially due to the available water in the system. To investigate the possible cause for the crossover, we derived analytical solutions for a cylindrical medium with composite properties, i.e., one set of medium properties for the inner cylinder and the different set of properties for the outer cylinder (Appendix A). The results from analytical solutions are illustrated in Figure 15, which also exhibits crossover between curves of different EDZ permeability. Figure 16 depicts the cumulative water flow into the drift, computed from analytical solutions. The results indicate that the cumulative amount of water entering the drift varies with the EDZ permeability at early times, but it is almost independent of the EDZ permeability at later times.

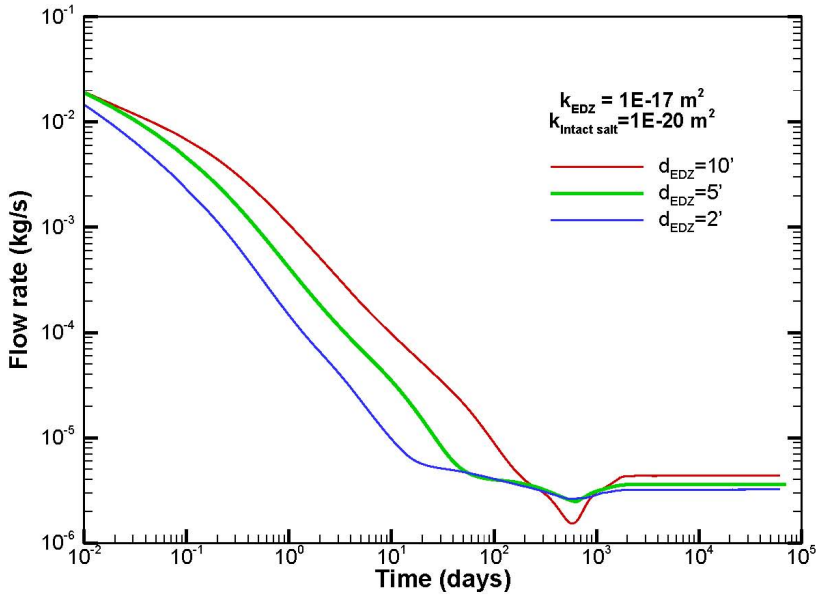

Figure 13: The effect of EDZ width on flow rate into the excavated opening.

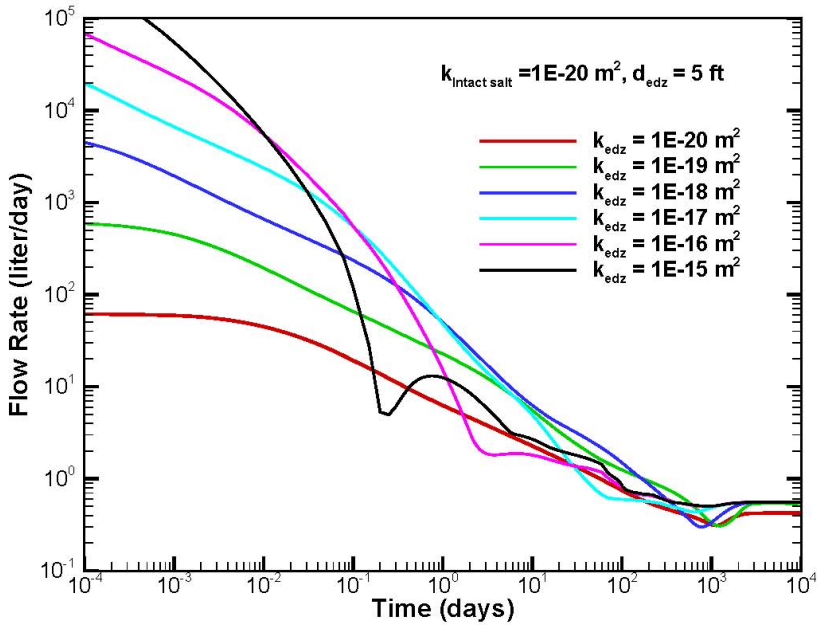

Figure 14: The effect of EDZ permeability (parallelogram shaped grid) on flow rate into the excavated opening.

Figures 15 to 16 show that the flow rate decreases quickly at earlier time and reaches a minimum, and then increases slightly, followed by a slow decrease. The magnitudes of these increases and decreases depend on the permeability contrast between the EDZ and the intact salt. Such behaviors are observed even when the permeability contrast does not exist (i.e., the permeability of both EDZ and intact salt is 10^{-20} m^2), which simply means that, besides the permeability contrast, there are other factors that may contribute to this behavior. Possible explanations that were examined and ruled out include: 1) inaccuracies due to the parallelogram shaped grid in these numerical simulations (ruled out by repeating the calculations using a cylindrical grid); and 2) artifacts that arise due to the particular permeability values selected (other combinations of values exhibited similar behavior). A final possibility is that such behavior may be due to the fact that the cavity is treated as an unsaturated "Porous medium" in the numerical model, However, in the analytical solution, the cylinder has a hollow and water can freely enter the empty space. Future work will explore different approaches to modeling the cavity that may be closer to reality.

3.1.3 Heated Cases

In experiments conducted in WIPP described by McTigue and Nowak (1988), 470W and 1500 W heaters were placed in 0.8-m diameter vertical boreholes to simulate the heat generation that might be expected from the disposal of defense high level waste. Upon heating, the 470 W holes in Room Al yielded as much as 20 g/day within 10 days, after which the flow rates declined subsequently to about 10 g/day after 100 days, and the cumulative brine collected at 441 days was 4.3kg. A total of 36 to 38 kg of brine were collected in 600 days from the holes with 1500 W heaters. The cumulative flux of water to borehole B042 at the WIPP is shown in Figure 17. The flow rate rose steadily to a peak value of approximately 0.08 liter/day at about 100 days, and declined slowly thereafter. Also shown in Figure 17 are the flow rate and cumulative water simulated from FEHM. Both the flow rate and the cumulated flux have been scaled by the ratio of the borehole wall area and the opening area in the FEHM model.

Although our results show less total water flow into the borehole, the actual experiment intersected several clay bearing horizons that could add significant water to the totals (Bradey et al., 2013). Future simulations of B042 could be performed to look at the addition of these clay-bearing horizons.

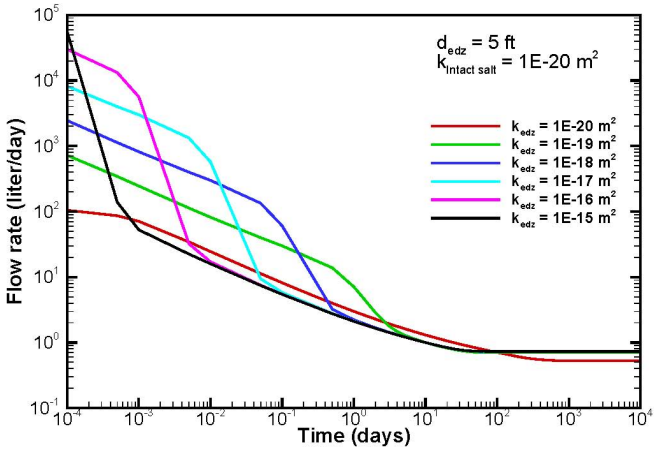

Figure 15: The effect of EDZ permeability computed from analytical solutions.

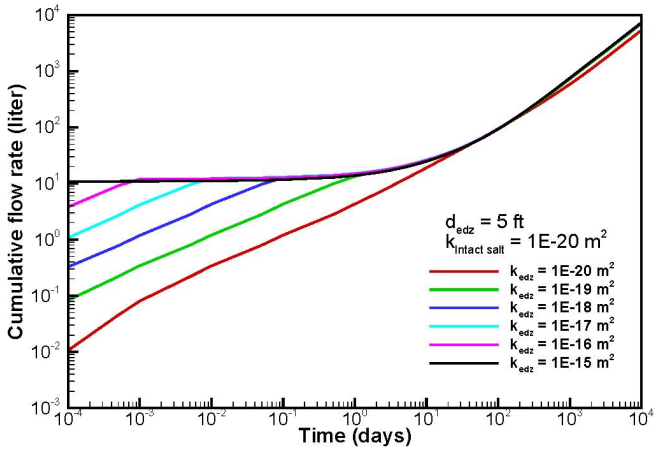

Figure 16: The effect of EDZ permeability on cumulative water flow into the drift (computed from analytical solutions).

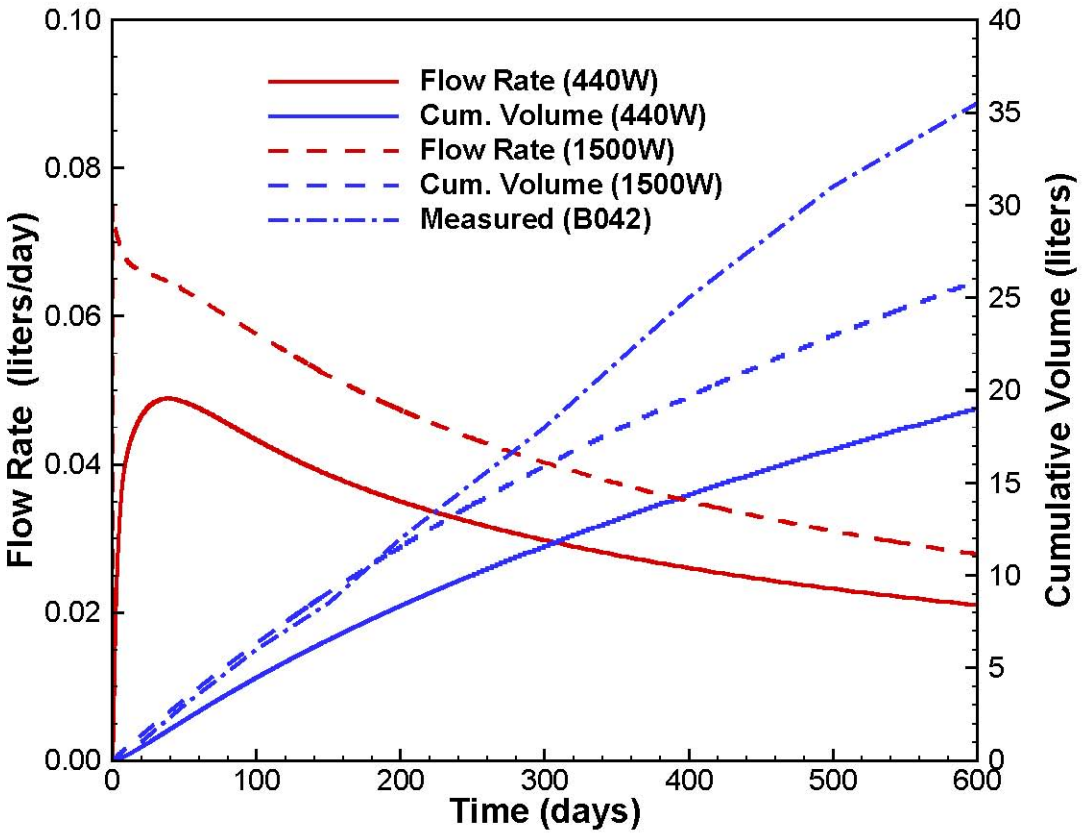

Figure 17: Comparison of flow rates and cumulative volumes for two heater sources and the measured cumulative volume from borehole B042 (McTigue and Nowak, 1988).

3.2 Code validation with bench-scale experiments

The thermal properties behavior of the RoM salt placed on heatings units, or in the case of a repository, on the waste packages, will have a strong bearing on the overall response of the near-field system. This section presents the results of several bench-scale experiments performed to test the salt material model in FEHM. The experiments ranged in size from a single intact salt crystal to a half meter-sized tub of crushed salt. Three experiments are presented:

(1) Intact salt crystal, heated on one side with fixed temperature
(2) 12.5 cm beaker, linear heating element with fixed temperature
(3) Cone of salt in 0.5 m-diameter tub, 125 W lightbulb

A brief description of each experiment is provided below, alongside the model results. Additional information about the intact salt and beaker-scale models is provided in Caporuscio et al. (2013).

3.2.1. Intact salt crystal

A single intact salt crystal of approximate dimensions 3.1 cm x 1.8 cm x 1.4 cm was heated uniformly across the face perpendicular to the longest side; the temperature was maintained at 60, 80, and 100°C for three separate experiments. The intact salt crystal was modeled on a grid with 0.5 mm grid spacing in the crystal and 2 cm spacing in the surrounding air for a total of 222,666 nodes (Figure 18). The crystal was assumed dry. Within the salt crystal, thermal conductivity varies with temperature following Equation 1.

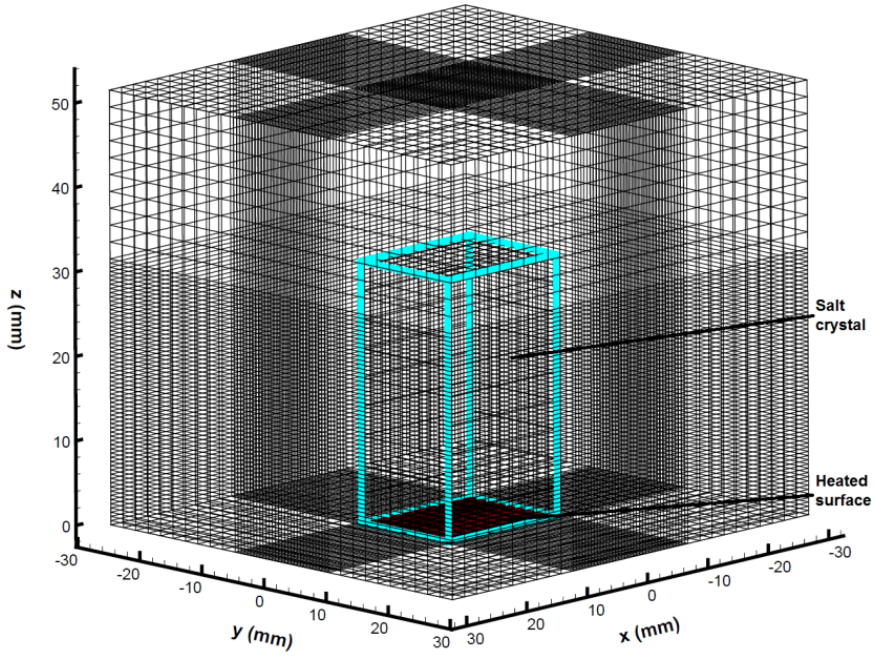

Figure 18: Numerical grid for the intact salt crystal model

In the experiment, after approximately 15 minutes, the surface temperatures of the crystal reached steady state, after which temperatures were measured along the length of the salt crystal. Data are shown in Figure 19. In all cases, the temperature drops steeply with distance before leveling off.

The effective thermal conductivity of air in the model greatly influences modeled surface temperatures of the crystal. Estimates of effective air thermal conductivity for this system ranged from 0.5 to 1.0 $Wm^{-1}K^{-1}$ for combined conductive, convective, and radiative heat transfer in air. The best matches to the intact salt crystal data ranged from 0.25 to 0.4 $Wm^{-1}K^{-1}$, depending on the temperature of the heater. Figure 19 shows the experimental data and FEHM model results for the intact salt crystal at three temperatures (60, 80, and 100°C) after 24 hours. The "bounce" in the end of the data that is not well-matched by the simulation results could be due to unmodeled edge effects (the experimental setup included a metal rod in contact with the salt crystal on the far side).

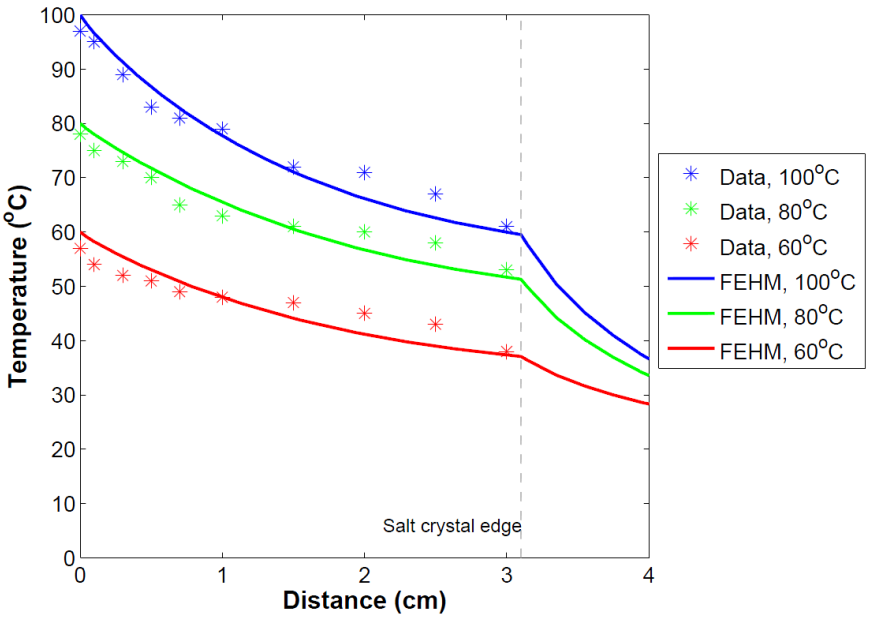

Figure 19: Intact salt crystal data and model results at steady-state.

3.2.2. Crushed salt beaker experiment

An experiment was performed with a beaker of diameter 12.5 cm filled to 10 cm in height with RoM crushed salt (Figure 20). A linear heating element maintained a temperature of 250 ± 20°C. The measured value of the porosity of the crushed salt was 0.39. After temperatures in the beaker reached steady-state, a probe was used to measure temperature in the crushed salt with distance from the heating element.

The beaker of crushed salt was modeled in 2-D and 3-D on fine grids using FEHM. A portion of the 3-D grid is shown in Figure 21; the 2-D grid is a YZ-plane slice with the heating element that extends infinitely in the X dimension. The thermal conductivity function for crushed salt is both temperature- and porosity-dependent (Equation 4).

The zones of the model and temperature distribution after 1 day are shown in Figure 22 for the 3-D model and Figure 23 for the 2-D model.

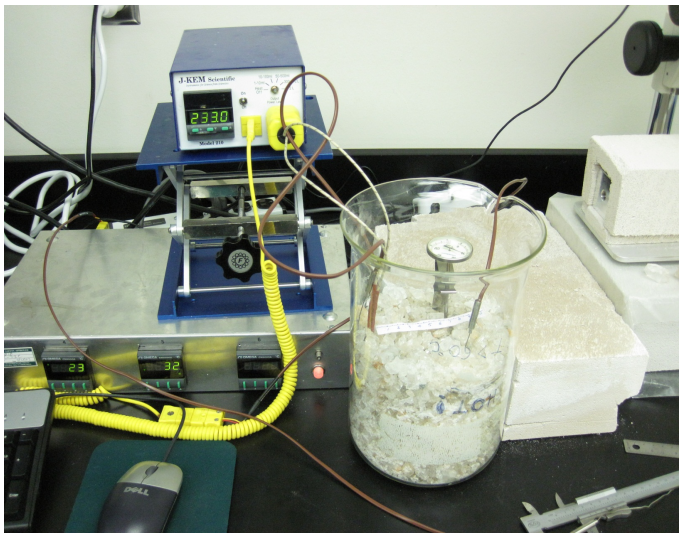

Figure 20: Crushed salt experiment in a 12.5-cm diameter beaker

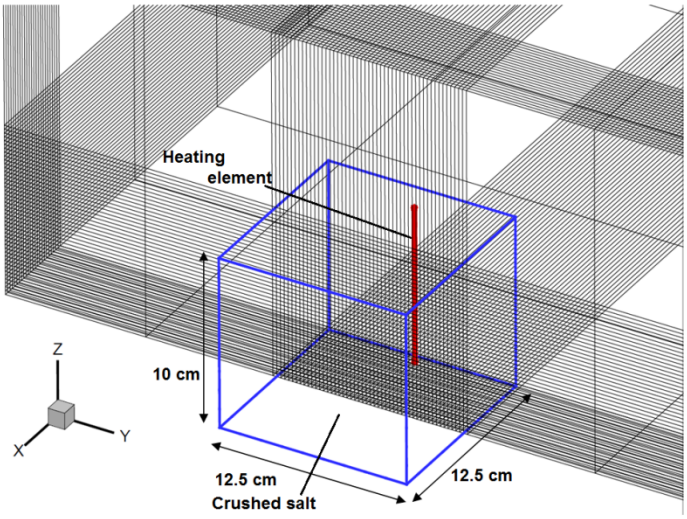

Figure 21: Grid for the 3-D model of the crushed salt beaker.

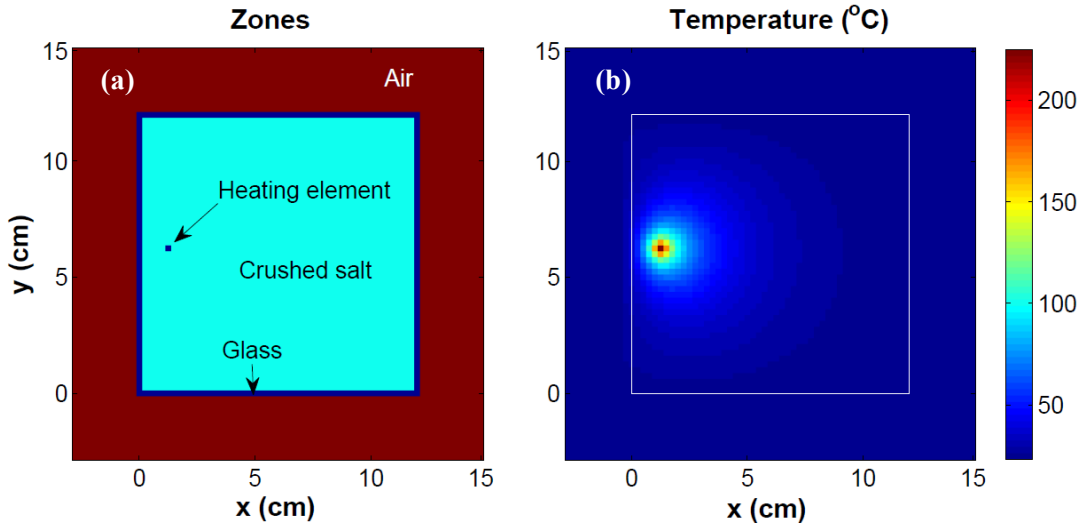

Figure 22: Slice through the 3-D model (XY-plane at z=4.5 cm). (a) Zones of differing properties in the model; (b) Steady-state temperature.

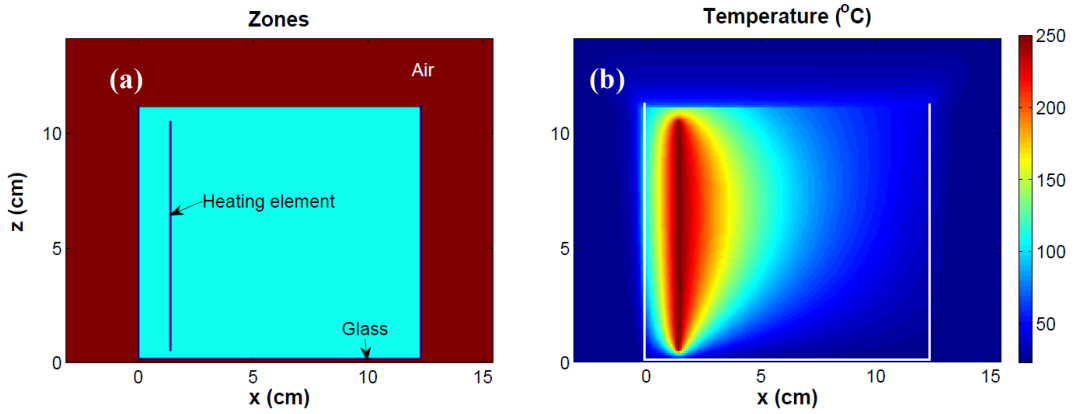

Figure 23: Side view of 2-D model, where model is infinite in the plane into/out of the page. (a) Zones of differing properties in the model; (b) Steady-state temperature.

The 2-D case stays warmer to greater distances than the experimental data due to the heating element having planar geometry in the 2-D model. In 3-D, the heating element was a line of nodes 1.5 cm from the edge of the beaker. As expected, the salt cools much more rapidly with distance from the heating element in the 3-D case, but the temperature decline with distance is steeper than the experimental data (Figure 24). Additional tests will be needed to analyze the model/data discrepancy.

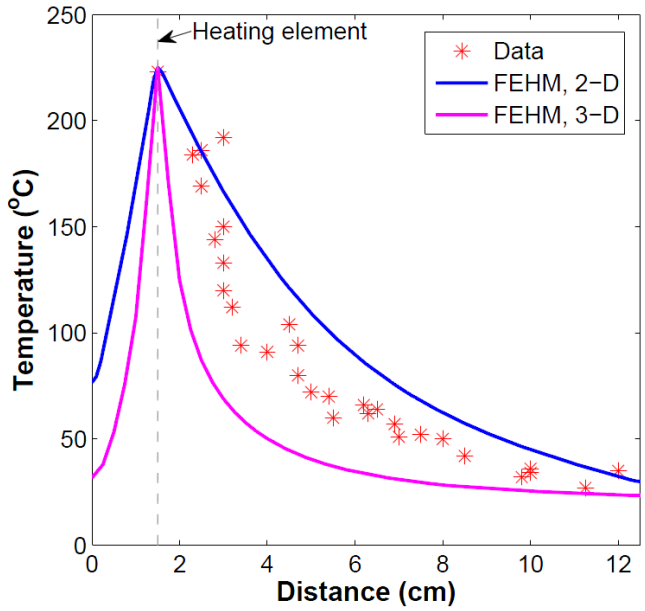

Figure 24: Crushed salt data and model results at steady-state.

3.2.3. Crushed salt tub experiment, cone shape

An experiment was performed with a 125 W bulb mostly submerged in RoM crushed salt piled into a cone shape of height 31 cm in a plastic tub (Figure 25). The measured porosity of the crushed salt was 0.375. Temperatures were recorded at 1-minute intervals in separate experiments with the temperature probe at different distances below the bottom of the bulb. Temperatures taken directly against the bulb were used as a time-varying boundary condition for the bottom half of the bulb.

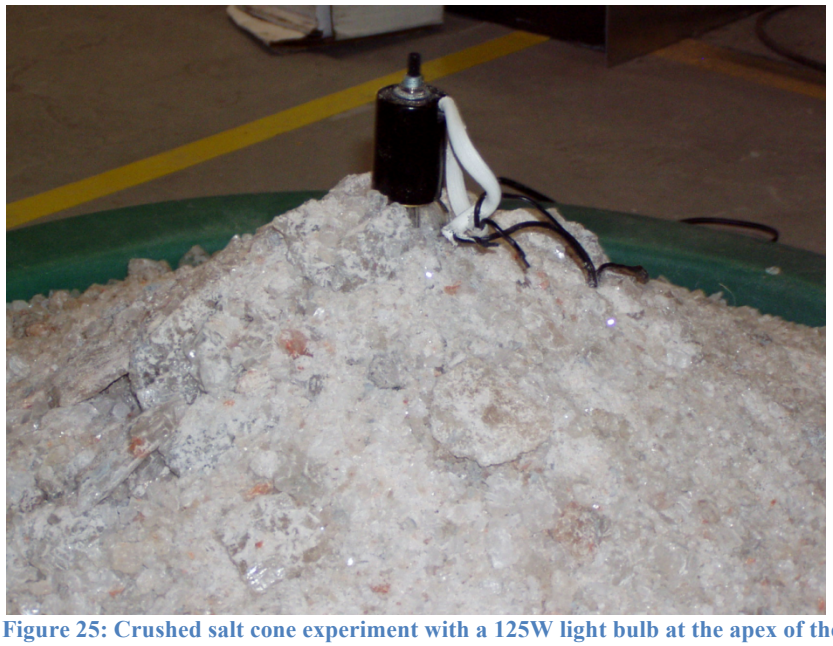

Figure 25: Crushed salt cone experiment with a 125W light bulb at the apex of the cone.

A 2-D radially symmetric model was designed in FEHM to simulate the experiment and test the variable thermal conductivity function for crushed salt. The model has 10609 nodes with 0.5 cm spacing in the crushed salt pile and 1% saturation. Final temperatures after 120 minutes are shown in Figure 26.

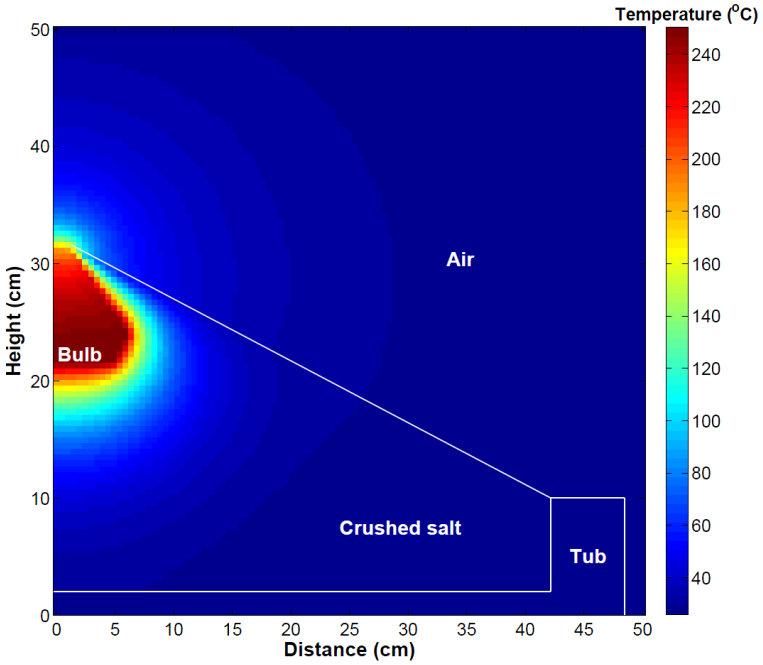

Figure 26: Temperatures after 120 minutes for the crushed salt cone experiment.

Temperature data and model results are shown in Figure 27 for the experiment with thermocouple 6 in. (15.2 cm) below the bulb. Figure 28 shows results for a separate experimental run with the thermocouple 2.5 in (6.35 cm) below the bulb.

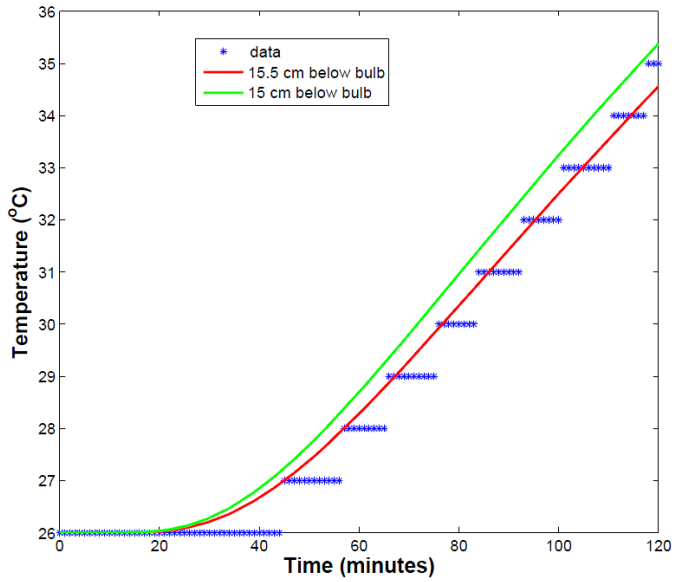

Figure 27: Temperature data and model results for a thermocouple located 6 in. (15.2 cm) below the bulb.

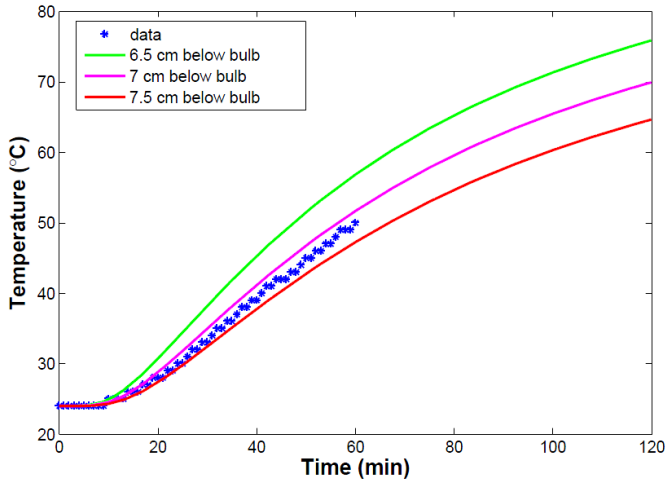

Figure 28: Temperature data and model results for a thermocouple located 2.5 in (6.35 cm below the bulb.

As indicated by these comparisons, the model runs slightly hot; that is, greater depths match the temperature profile more closely than the actual depth of the thermocouple. However, the results are quite good: for the deeper thermocouple, the closest match to the data is < 0.5 cm from the actual depth, and for the shallower thermocouple, < 1 cm. The model results are very sensitive to saturation and porosity. The difference in temperatures between a drier (saturation of 0.1%) and wetter (saturation of 1%) simulation are shown in Figure 29. Drier conditions result in hotter temperatures close to the bulb, in the boiling region, where less water means less cooling from the latent heat of vaporization of water. Temperatures are cooler farther from the bulb in the drier case, outside the boiling region, where the greater thermal diffusivity of the dry crushed salt ($k/\rho c_p$) more effectively transports heat away than in the wetter case.

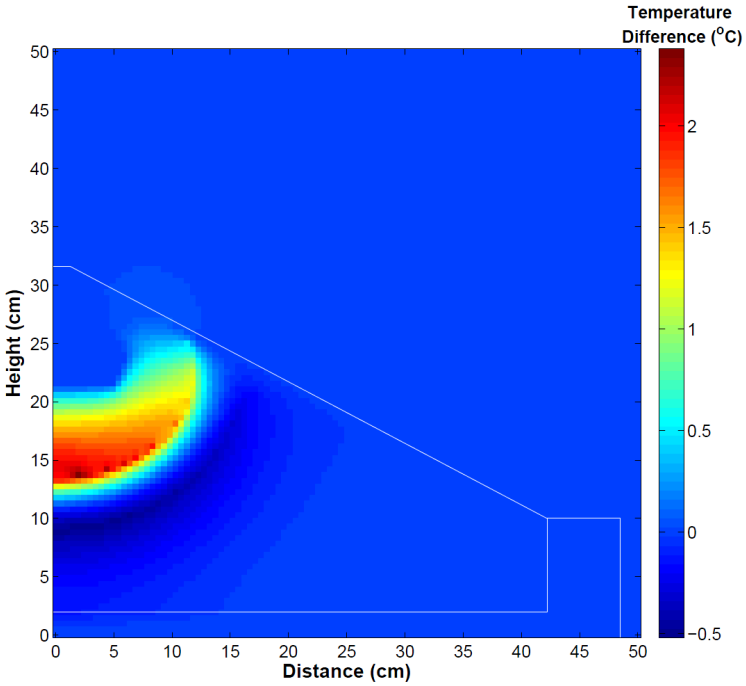

Figure 29, 3.2.3-5, Temperature difference, dry (0.1% saturation) minus wet (1% saturation) after 120 minutes for the crushed salt cone experiment.

4. Thermal-Only (T) Calculations of a Field Scale Heater Test

The goal of the next three chapters is to show, step by step, the model-building process that culminated in the full THC capability that can ultimately be used to predict the thermal evolution and liberation and fate of water during the initial phase of waste emplacement, before significant geomechanical effects influence the properties of the intact and RoM salt. A subsidiary goal of this model development is to assist in the design of field scale heater tests to study the behavior of such a system. If such a test is performed in the future, the model would be essential to design the test and place instrumentation, as well as being a prediction that could ultimately be benchmarked against the observed field-scale behavior.

In this chapter, we present calculations using heat flow only, with no water present. Following this chapter (Chapter 5), a series of simulations using an approximation of the seepage flow from intact salt into partially saturated run-of-mine salt is presented. Finally, in Chapter 6 we present the fully coupled THC simulations. Thus, this model configuration simulates an experiment testing the in-drift disposal concept of placement of a waste package (or heater in the case of a field demonstration) on the floor of the drift, and covering it with RoM salt as backfill for radiation shielding. Presenting the results in this way illustrates the role that the more complex hydrologic and chemical processes play in the behavior of the system, as compared to a system controlled by thermal conduction.

To motivate discussions of potential behavior of a defense-waste repository and a thermal test at those conditions, we begin this chapter with a discussion of the heat loads that would be encountered in such a system. For defense waste, data on existing thermally active waste containers from around the DOE complex suggest heat loads that could vary from less than 100 W per package to some with over 2000 W per package (Carter et al. 2012). Figures 30 (HLW) and 31 (SNF) show histograms of the inventory.

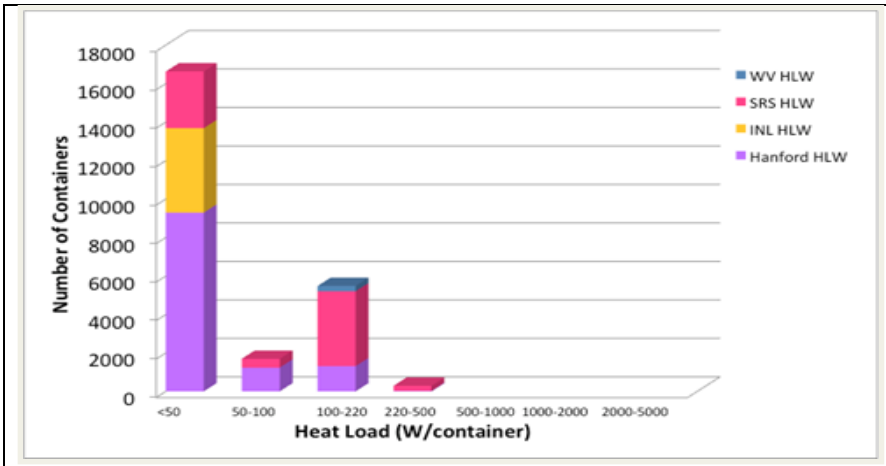

Figure 30: Histogram of DOE High Level Waste (HLW) packages by heat load

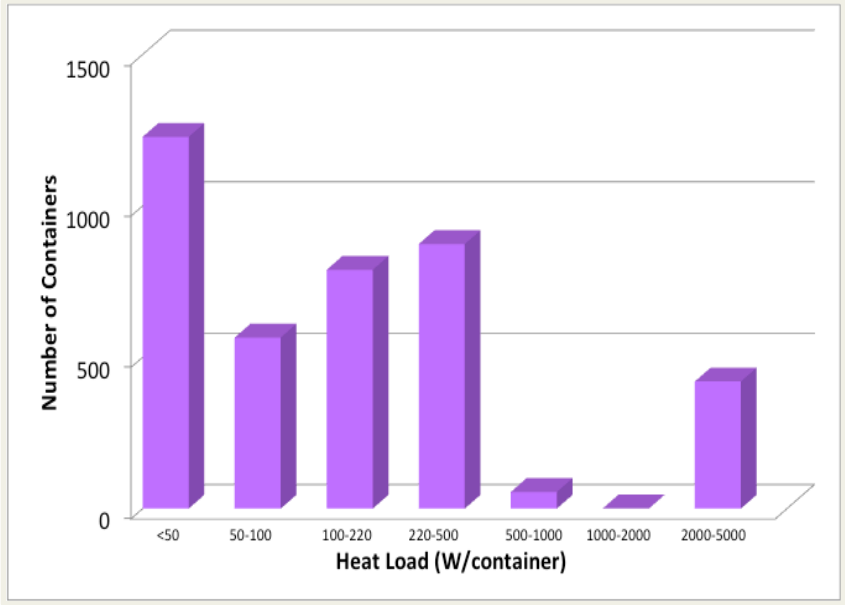

Figure 31: Histogram of DOE Spent Nuclear Fuel (SNF) packages by heat load

Civilian waste consists primarily of SNF from the nation's nuclear power reactors, stored temporarily by the utilities at the site of currently or formerly operating nuclear power plants. The Yucca Mountain EIS categorized the heat loads of disposal packages for the Yucca Mountain repository on the basis of average heat loads across a wide range of fuel burnups and ages. The analysis was designed to enable the average heat load across the repository to be represented, to specify the configuration of disposal packages to be disposed of in the repository, and to ensure that the heat loads were reasonably bounding. Given this purpose, the EIS specified a total of 4239 containers of PWR SNF with 21 fuel assemblies per container, and 2784 containers of BWR SNF with 44 fuel assemblies per container. The

heat loads specified were 8800 W/container for the PWR SNF, and 6200 W/container for the BWR SNF; we call these average values the "EIS baseline values." These values mask a broad variability in the heat loads of actual SNF, some of which is much cooler. In general, SNF discharged from commercial reactors in the 1960s - 1980s has much lower burnups than fuel being produced today, a factor that, along with the longer out-of-reactor cooling period, leads to lower heat loads. For example, the 6138 MTHM of BWR SNF and 9,701 MTHM of PWR SNF produced from 1968 to 1987 was discharged with an average burnup of 21,000 MWd/MTHM for the BWR SNF and 28,000 MWd/MTHM for the PWR SNF (derived from Tables 3 and 4 of Notz, 1990). Considering the 50 years of cooling of a low-burnup, older fuel, versus an average design basis of 23-year cooled fuel with higher burnup (33,600 MWd/MTHM for BWR and 41,200 MWd/MTHM for PWR), we would expect some 21-PWR and 44-BWR packages to have heat loads at the time of disposal that are at least a factor of 0.5 lower than the design values used in the EIS, placing these packages in the range of 3100-4400 W/container. At a finer level of discretization, within the inventory of older, low-burnup fuel, there are portions with burnups much smaller even than these lower average values, implying heat loads that are lower still.

Beyond this analysis, it is possible that the consideration of a new repository might lead to a reconsideration of the number of fuel assemblies packaged in an individual disposal container. Hardin et al. (2011) examined thermal management issues associated with clay, granite, deep borehole, and salt repository disposal concepts, and concluded that for the concepts considered and our current state of knowledge on repository temperature limits likely to be used in repository design, salt is the medium best suited to enable relatively large disposal packages to be emplaced without exceeding temperature limits. However, all media and disposal concepts examined by Hardin et al. (2011) required smaller waste packages: from 1 assembly per waste container for deep boreholes to 12 or more assemblies per container for salt. Because all of the scenarios examined were for closed repository designs, heat management limitations are more severe than for the open design of the Yucca Mountain repository, which emphasized retrievability and thermal management during the pre-closure period as basic design concepts.

Given this result, it is reasonable to conclude that smaller disposal packages (with fewer assemblies per package) could be disposed of in a future salt repository, with the heat load per package scaled accordingly. For example, if the EIS baseline values for 21-PWR and 44-BWR packages are scaled to 4 and 12 assemblies, respectively, the heat loads would scale to values of 1680 W/container for 4-PWR packages and 1270 W/container for 12-BWR containers. These values fall within the range of thermal outputs for disposal packages of defense wastes.

The purpose of this discussion is to illustrate that an intermediate heat load thermal test would provide important field based evidence relevant to commercial SNF, either for older, cooler fuel, or in a

disposal scenario in which assemblies are emplaced in smaller waste packages with fewer assemblies per package, or a combination of the two approaches. Thus, such a test would significantly advance the scientific basis for both defense and civilian wastes. When combined with an alcove disposal concept that optimally distributes high heat waste packages in the repository (e.g. Robinson et al., 2012), the in-drift concept covers the entire range of thermal conditions likely to be required for all defense and civilian wastes. Finally, we note that the in-drift concept would lead to significant ventilation of the drift for the time period in which the salt remains unconsolidated. During this period, perhaps lasting several decades, air flow through the system will remove significant quantities of heat and water vapor, influencing the moisture content and the thermal profiles in the heated area. Therefore, the in-drift system resembles an open repository design in which heat and moisture will be expelled from the emplacement drifts: these processes are considered to be advantageous from the standpoint of repository operations. For this reason, it is likely that fairly aggressive heat load in the drift could be accommodated, which opens the possibility of disposal of intermediate-heat wastes in the range of 500-2000W/container.

The crossover heat loads for which alcove disposal would be preferred over in-drift disposal are at present uncertain, but important information would be derived from an in-drift field test to address that issue. Finally, we note that the time period of significant air flow in a disposal operation will be much greater than the duration of a field test, meaning that the demonstration will focus on a quantitative understanding of early-time processes important to thermal management and repository conditions that would then set the stage for predicting long-term behavior of the RoM salt and adjacent intact salt. Note that because of the focus on initial behavior, the degree to which drift closure impacts the consolidation of the backfill salt should be relatively small, thereby justifying the use of a coupled model that excludes the long-term geomechanical effects on the system. For long-term simulations, including post-closure analyses, these effects would certainly need to be included.

4.1 Drift scale heater test simulation design Thermal Only (T)

A 3-D numerical mesh, shown in Figure 32, was created to include a section of a salt repository measuring 40 m x 40 m x 40 m. An experimental drift is located in the center of the domain, with five heaters spaced equally along the length of the drift. RoM salt is backfilled on top of the heaters with angle-of-repose slopes forming on either end of the drift.

The experimental drift is centered at coordinate position (0,0,0), and surrounded by access tunnels. Dimensions of the experimental drift, crushed salt backfill, access tunnels, and other aspects of the simulations are given in Table 2. This table shows actual dimensions in both feet and meters followed by the approximate equivalents that were used in the simulations. The slight differences are due to

approximations made for convenience in the construction of the orthogonal grid. The numerical mesh maintains 0.5 m lateral spacing around the experimental drift with the same 0.5 m vertical to 3 m above and 3 m below the drift floor (Figures 32 and 33). Five heaters, shown in both Figures 33 and 34 have dimensions of 2.5m x 0.5m x 0.5m in XYZ space.

Table 2: Dimensions used for simulated drift for thermal-only calculations

	ft	m	Simulated
heater length	9	2.7432	2.5
drift width	11	3.3528	3.5
lateral salt width	38	11.5824	11.5
length	80	24.384	25
hight of crushed salt	10	3.048	3
depth below floor	10	3.048	3
above ceiling	10	3.048	3
lateral center to drift	43.5	13.2588	13
hight of salt + buffer	16	4.8768	5
Access tunnel height	13	3.9624	4
Access tunnel width	16	4.8768	5
half the length of the block	40	12.192	12
solid crused salt section N	20	6.096	6
edge of salt slope	34	10.3632	10.5

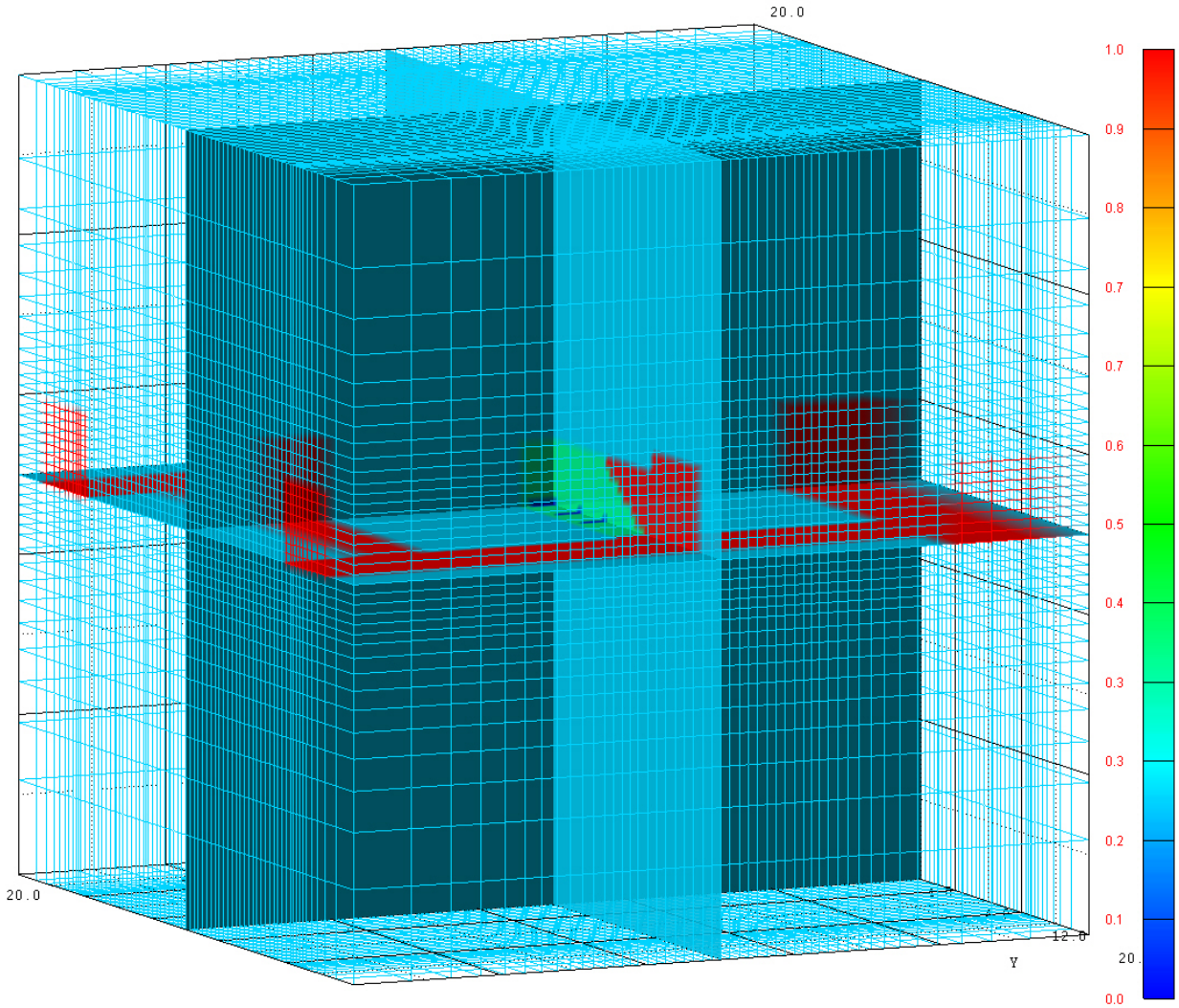

Figure 32: Porosity mapped onto slice planes of the numerical mesh for the proof-of-concept drift scale heater simulations. Access drifts and the outer edge of the experimental drift can be seen as red (porosity = 1.0), while the crushed salt backfill can be seen as the sloping green region with porosity of 0.35.

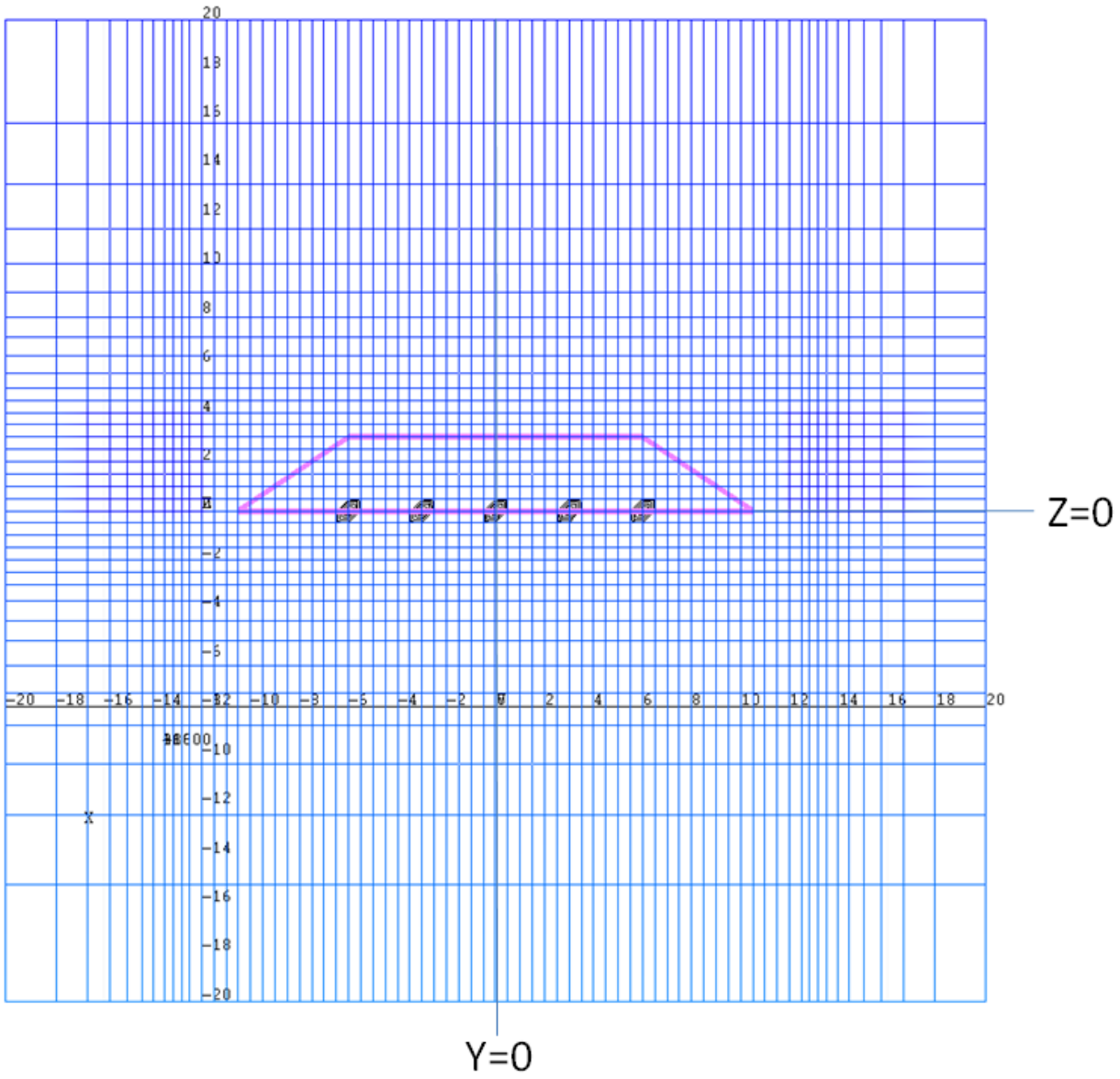

Figure 33: Numerical mesh on XZ plane. The five heaters can be seen in the middle of the mesh, lying under a pile of run-of-mine salt used as backfill (pink trapezoid).

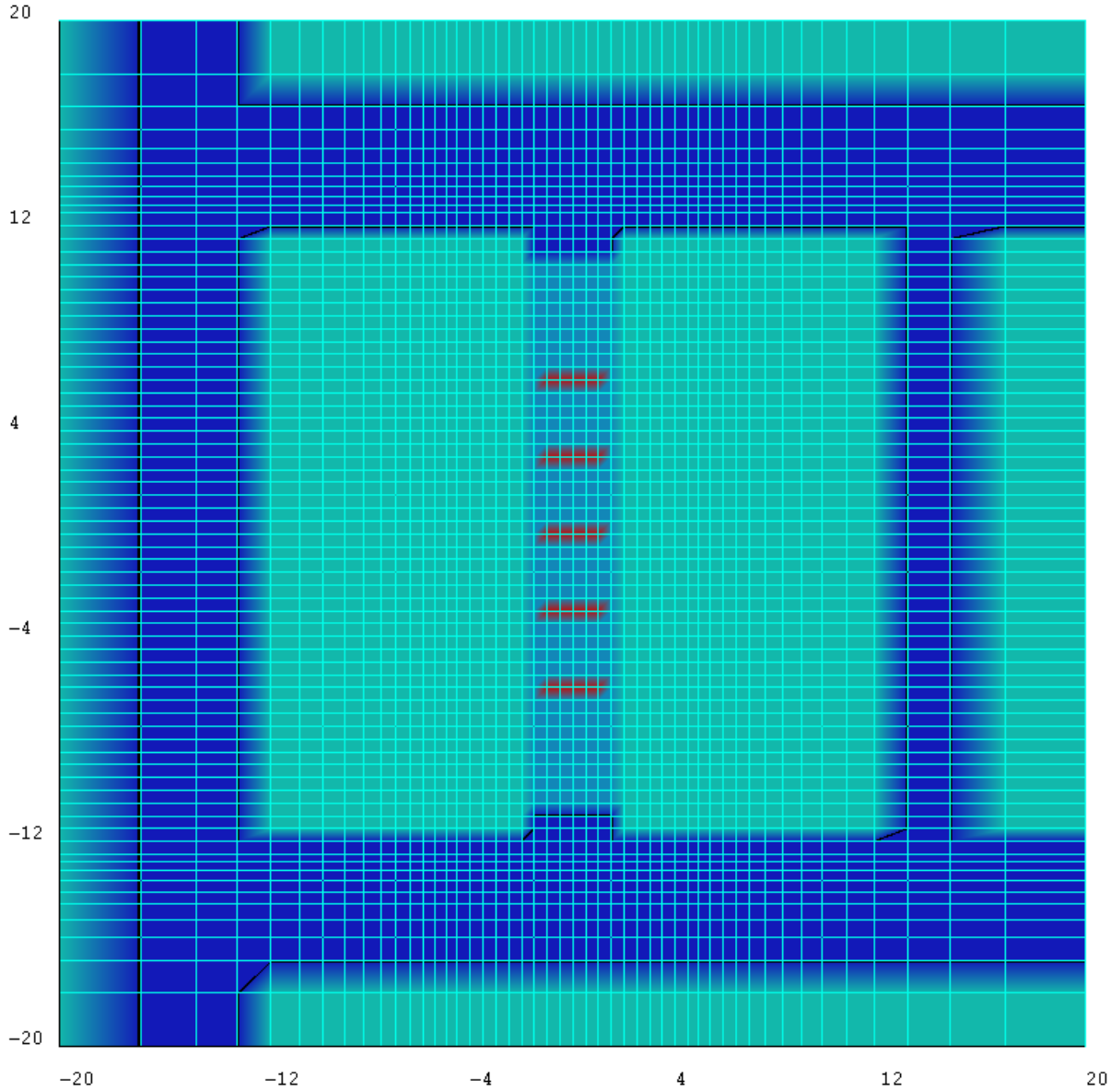

Figure 34: Numerical mesh on the XY plane at Z=0. The five heaters can be seen in the middle of the mesh. The access drifts are dark blue around the perimeter of the domain, while the experimental drift lies directly in the center and is lighter blue where the run-of-mine salt backfill is located.

4.2 Results of the Drift scale heater test Thermal Only (T)

In this section, simulations are presented for a range of heating scenarios with heat loads per canister ranging from 500-2000 W. These results are depicted in Figures 35 – 37 and discussed below.

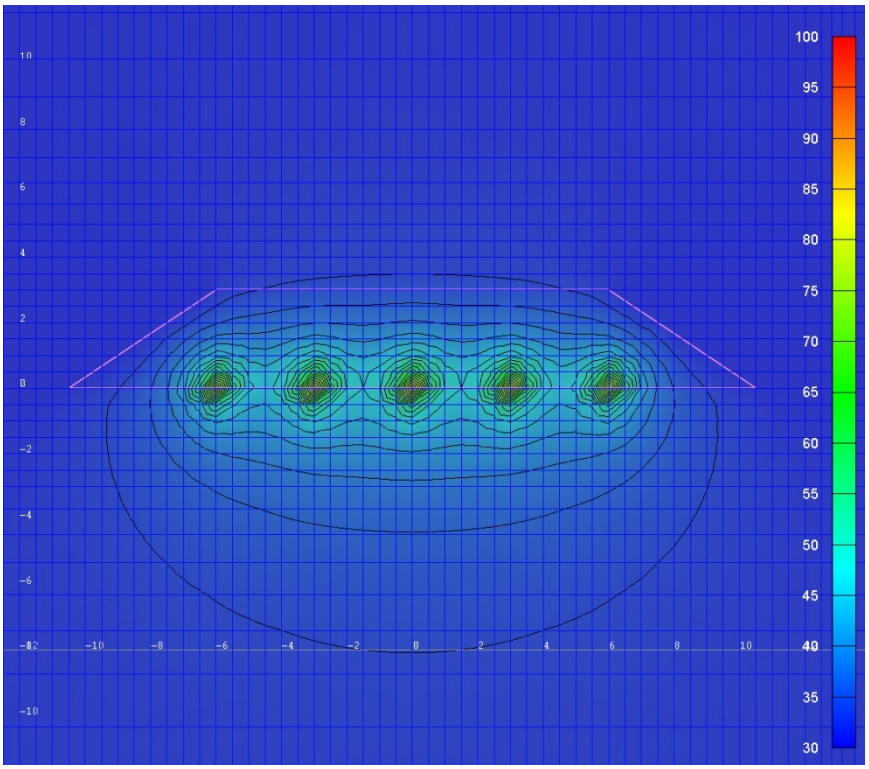

Figure 35: Temperature profile near steady state (1 yr) for five 500W heaters.

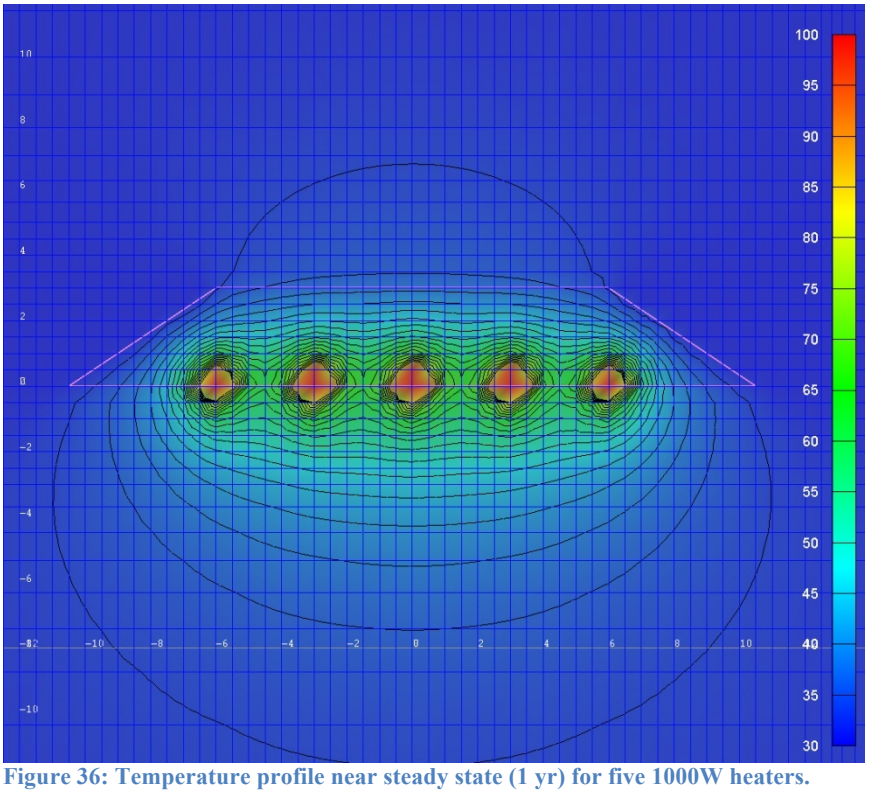

Figure 36: Temperature profile near steady state (1 yr) for five 1000W heaters.

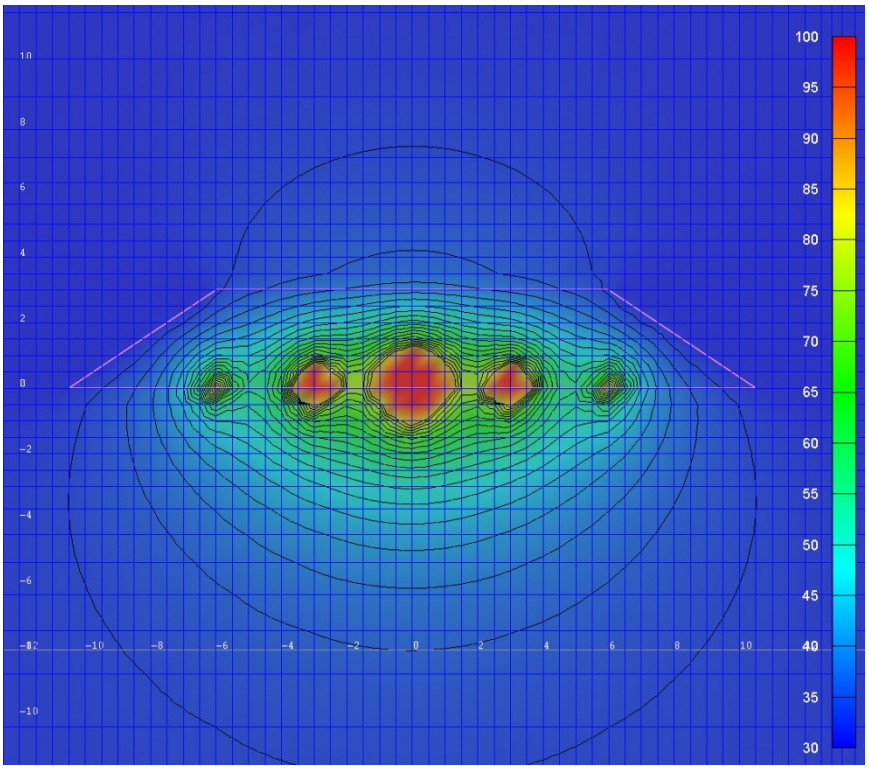

Figure 37: Temperature profile near steady state (1 yr) for five heaters with variable loads ranging from 2000W in the center, 1000W adjacent to the center, and 500W on the outer edges.

Temperature gradients of the sort presented in these figures serve as a prelude to understanding the potential water migration issues in either a field experiment with electrical resistance heaters or an actual repository scenario. Coupled thermal-hydrologic simulations are presented in the next chapter, but the concepts to be studied are introduced here. As air moves through the porous run-of-mine salt that covers the heaters, it will become saturated with water vapor at the local thermodynamic conditions (temperature, fluid ionic strength), as long as there is liquid water present. As the air moves from a warmer to a cooler location, there will be a driving force for water condensation. Furthermore, water vapor transport and condensation could itself affect the thermal response through the heat transfer if the water vapor effects are vigorous.

Water is present initially in the run-of-mine salt, and will be augmented by seepage of water toward the drift from the surrounding intact salt. Thus, the bulk migration of water as liquid and vapor in the vicinity of the heaters (or waste packages) is subject to multiple processes, including pressure and temperature-driven flow into the drift, vaporization, and advective transport in the air phase, and possibly condensation in cooler regions due to supersaturated conditions. One of the main purposes of a field test is to demonstrate an understanding of the interplay of these processes that is sufficient to develop a quantitative model of the overall water balance during the first few years of heating. This model will

serve to characterize potential changes to the rock mass that are influenced by the presence of water, and enable potential fluid interactions with the waste packages to be assessed. More information on these results can be found in Harp et al., (2013).

5. Thermal-Hydrologic (TH) Calculations of a Field Scale Heater Test

This chapter presents results from initial calculations of coupled thermal-hydrological simulations intended to give a first glimpse at how moisture will redistribute in the presence of thermal loading. FEHM has been used successfully for convection studies in unsaturated media (e.g. Stauffer and Rosenberg, 2000; Stauffer et al., 1997; Kwicklis et al., 2006). We first describe a reduced numerical mesh (extracted from the mesh used in Chapter 6) that allows faster calculations. Next we describe unsaturated properties and initial conditions. Finally, we present a several hypothetical scenarios involving different amounts of seepage water at different heat loads.

5.1 Model Setup

A 3-D numerical mesh, shown in Figure 38, was created to include a section of a salt thermal test domain measuring 20 m x 25 m x 40 m, with 0,0,0 lying exactly in the middle of the simulated experimental drift. An experimental drift is located in the center of the domain, with five heaters spaced equally along the length of the drift. RoM salt is backfilled on top of the heaters with angle of repose slopes forming on either end of the drift. The mesh represents a half-space with a reflection boundary along x=0.

Material properties are the same as used in subsequent THC calculations (see Chapter 6, Table 4), with the exception of porosity of the intact salt, which was increased to 2%. The coupled model requires the several additional properties. The simulations require that a tortuosity be used to calculate the water vapor diffusion coefficient; a standard value of 0.6 is used for this term. Unsaturated relative permeability/suction functions must be assigned for all materials. The run-of-mine salt and intact salt are assigned van Genuchten properties that lead to very low suction (large pore structure) with α=5.6 m^{-1}, n=1.8, residual water saturation of 0.0001 and maximum saturation of 1.0. The air in the drift is assigned a linear relative permeability model that generates no capillary suction. Rom salt is given a permeability of 1.0×10^{-12} m^2, while the air is set to 1.0×10^{-11} m^2. Thermal properties are assigned based on the information presented in Chapter 2.

Modeling the air as a porous medium facilitates maintaining the air at constant pressure while limiting computationally expensive convection that would occur in open air.

The drift lies along a reflection boundary, resulting in symmetry that reduces the number of grid points in the simulation by a factor of two. The run-of-mine backfill can be seen as yellow while the air in the drift is blue. The red surrounding material is intact salt with porosity of 0.02.

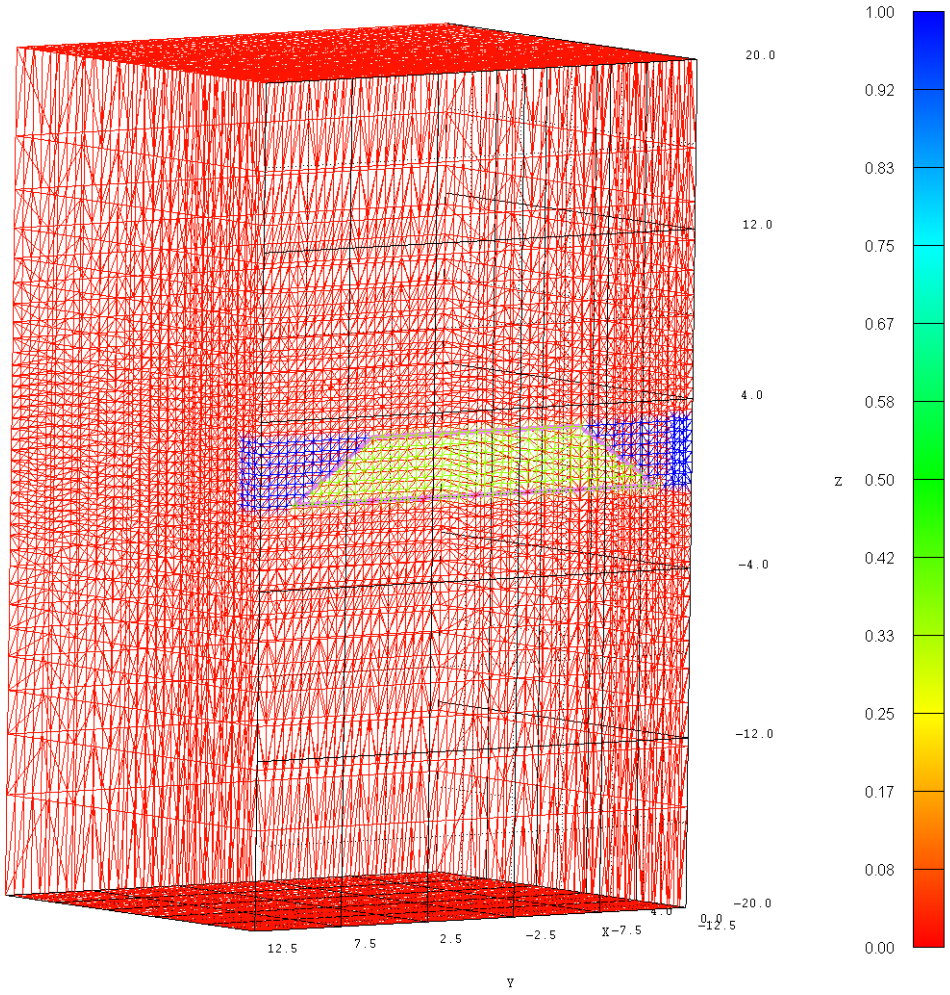

Figure 38: Porosity of coupled thermal/hydrological mesh.

Air pressure is fixed at the drift ends at a partial pressure and temperature such that the drift air maintains a pressure of 0.1 MPa and a temperature of 30°C. Thus, with no driving force for air circulation through the drift, these simulations represent the case in which air circulation is minimized, perhaps through the use of bulkheads to block or carefully control the air flow. The numerical mesh consists of 0.5 m lateral spacing around the experimental drift with the same 0.5 m vertical to 3 m above and 3 m below the drift. Background pressure in the far-field is set to 6.0 MPa at 30°C.

An initial condition is established by running the model for 50 days with no heating, and the permeability of the intact salt is established so as to generate leakage comparable to the borehole experiments. For this geometry, the surface area is approximately 32 times larger than the borehole

experiments (350 m^2), and a permeability of $6.0x10^{-20}$ m^2 yields leakage of 44 kg in 50 days. This is the same order as suggested by the non-heated period of borehole B042 (5-15 g/day on 11 m^2). The initial 50 day run is used to initiate simulations of heating in the drift and subsequent moisture redistribution in both the liquid and vapor phases.

The heater simulations are run for between 0.5 and 2.0 years, an amount of time likely to be devoted to such an experiment. Some of the simulations become numerically challenging as the competing flows of vapor and liquid set up a heat pipe in the crushed salt, and time step size is reduced such that running to 2 years of simulation time would require days of CPU time. Finally, thermal loads of 500W per heater to 1500W per heater are explored.

5.2 Model Results

5.2.1 Water Accumulation in the RoM Salt

To investigate the impacts of heat on the movement of water in the test drift, the initial 50-day run is restarted at time = 0 days and the heaters are turned on at constant thermal load. Because the problem uses symmetry, the heater nodes at the center of the drift are assigned ½ the thermal load of the heater nodes lying away from the reflection boundary. One of the primary diagnostics of the thermal simulations is the mass of water that moves from the intact salt into the run-of-mine salt backfill and the drift. The air in the simulation has no capillary suction, however because there are no outflows of liquid water allowed, some ponding on the drift floor occurs. This ponding accounts for less than 10% of all water flowing from the intact salt, so is relatively small from the standpoint of the overall water budget results presented here. To process the results, an algorithm was written to calculate the change in mass ΔM, for different regions as:

$$\Delta M = \sum_{n=1}^{nodes} (\mathrm{sat_f} * \rho_\mathrm{f} - \mathrm{sat_i} * \rho_\mathrm{i}) * \phi * vol)_\mathrm{n} \quad (27)$$

for each node n of the run-of-mine salt, drift, or bare drift floor; sat is the saturation, vol is the volume, ϕ is the porosity, ρ density of the water in the volume (a strong function of temperature), and the subscripts f and i refer to final and initial states. Table 3 shows output from the model for six simulations. Total drift water includes all water in the air and RoM salt, the floor water is only the bare drift floor nodes, and the run-of-mine row integrates the water found in only the RoM salt. As can be seen, less than 10% of the water that seeps into the drift ends up as ponds on the floor, while the majority of the water is pulled into the RoM salt and contributes to the coupled flow.

Table 3: Water mass found in different regions of the model at 305 days

	500W			1000W			1500W	
Permeability (m^2)	6.E-20	3.E-19	3.E-19	6.E-20	3.E-19	6.E-19	6.E-20	6.E-19
Total water seeped into drift (kg)	522	1230	2648	653	1338	2773	701	3576
Extra water in run-of-mine backfill (kg)	473	1115	2396	600	1219	2515	645	3315
Drift floor water (kg)	50	115	251	53	119	258	56	261
Percent on drift floor	0.095	0.094	0.095	0.081	0.089	0.093	0.079	0.073
% increase in run-of-mine water	0.132	0.312	0.671	0.168	0.341	0.704	0.181	0.928

5.2.2 Base case simulation (500W with k= 6 x 10^{-20} m^2)

An initial set of calculations were performed with 500W heaters to find a permeability that led to approximately the same amount of water per time per area as seen in the heated borehole experiment, B042. The rate of inflow from the experiment is 30 liters in 600 days for 11 m^2, corresponding to 490 kg in 305 days for the simulations presented. The time of 305 days was chosen for convenience, to accommodate the fact that several of the simulations could reach this time before numerical instabilities slowed the time stepping to very low increments. The closest fit simulation is represented in the second column of Table 3 and yielded 522 kg of seepage water. The initial saturation and saturation at 305 days on the symmetry boundary (x=0) are shown in Figure 39. The results of this simulation are typical of all the combinations of seepage and heat loads. Water is driven away from the five heaters, with saturation dropping to zero near the heaters. Water vapor is driven off and condenses as it cools away from the heaters. Once condensed, liquid water flows back toward the heaters, creating an ad-hoc heat pipe in the RoM salt. A map view of the saturation result on a plane sliced at z=0.5 (just above the drift floor) is shown in Figure 39C. The heaters do not dry out due to their material properties (very low permeability. Water preferentially accumulates at the end of the heater that contacts the drift wall (x=1.5 m).

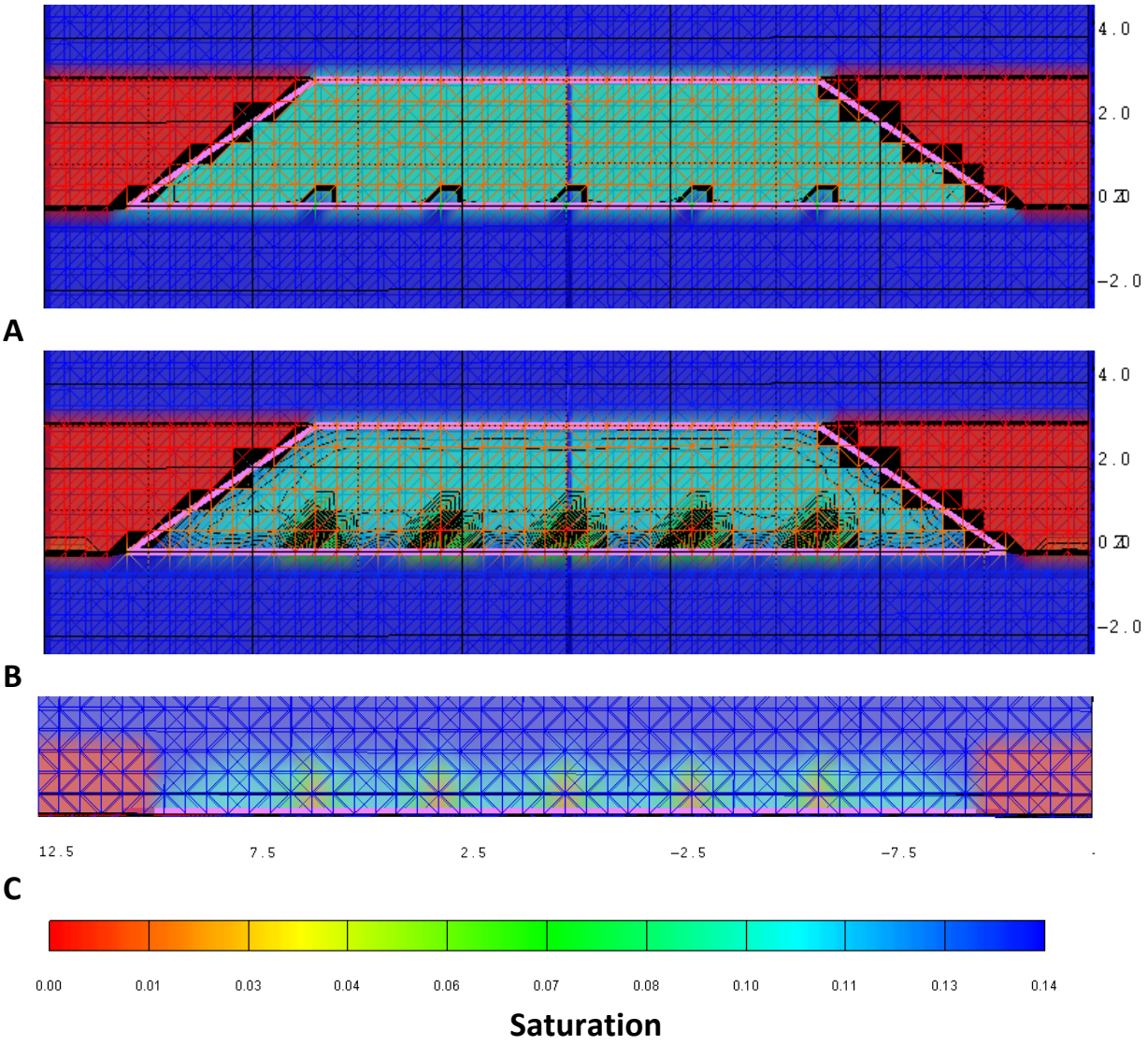

Figure 39: The initial saturation (A) and saturation at 305 days (B) close to the symmetry boundary (x-0.5). (C) shows saturation on the z=0.5 plane, just above the floor of the experimental drift.

The pressure profile driving flow from the background initial hydrostatic 6 MPa toward the 0.1 MPa drift is shown in Figure 40, for the case of the far-field boundary pressure fixed at 6.0 MPa and the saturation at 1.0. Finally, Figure 41 shows the associated temperature field on vertical and horizontal planes. Maximum temperature for this example is 81^{o}C.

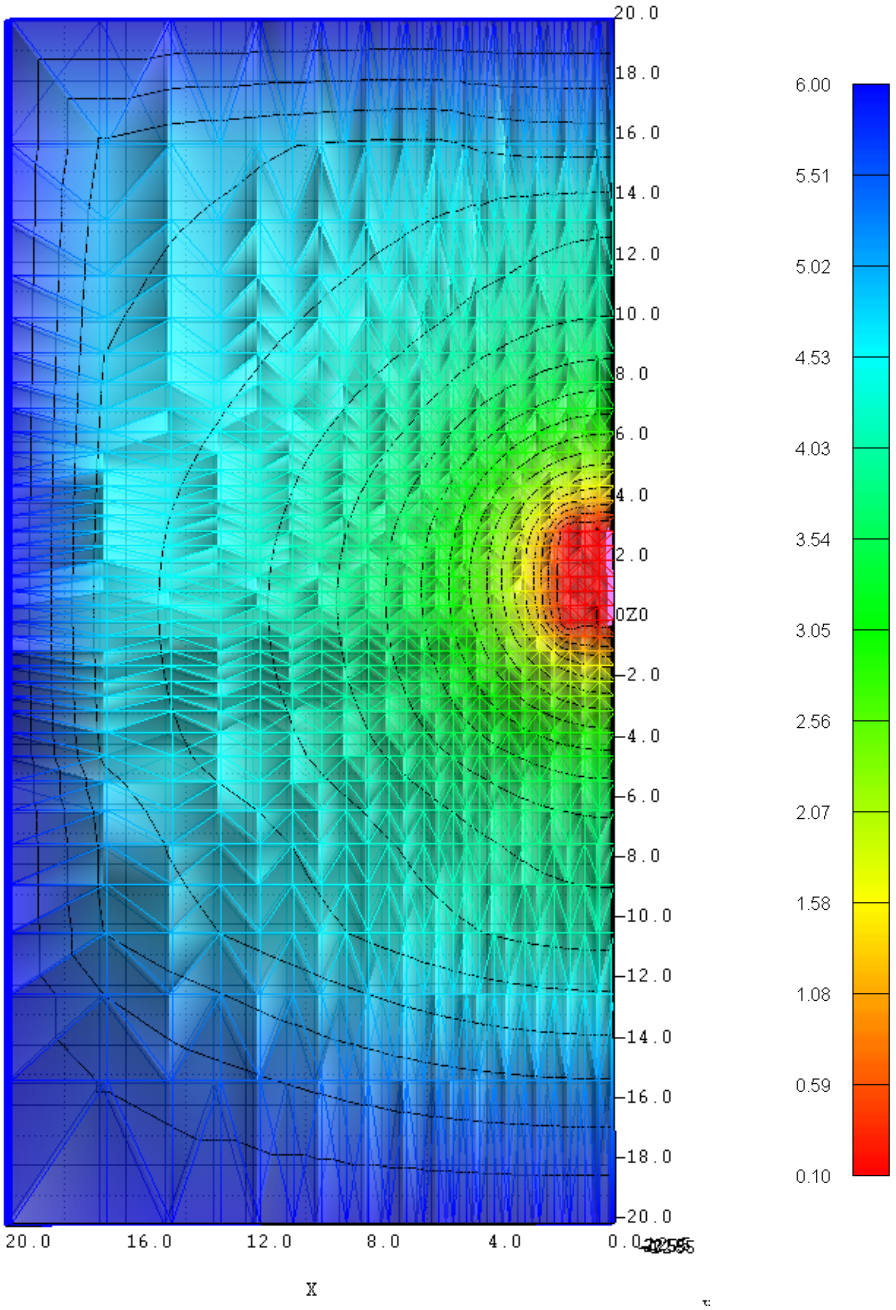

Figure 40: Pressure (MPa) around the 0.1 MPa drift at 305 days for the 500W heater scenario with k=6 x 10^{-20} m^2. The slice plane y=0.

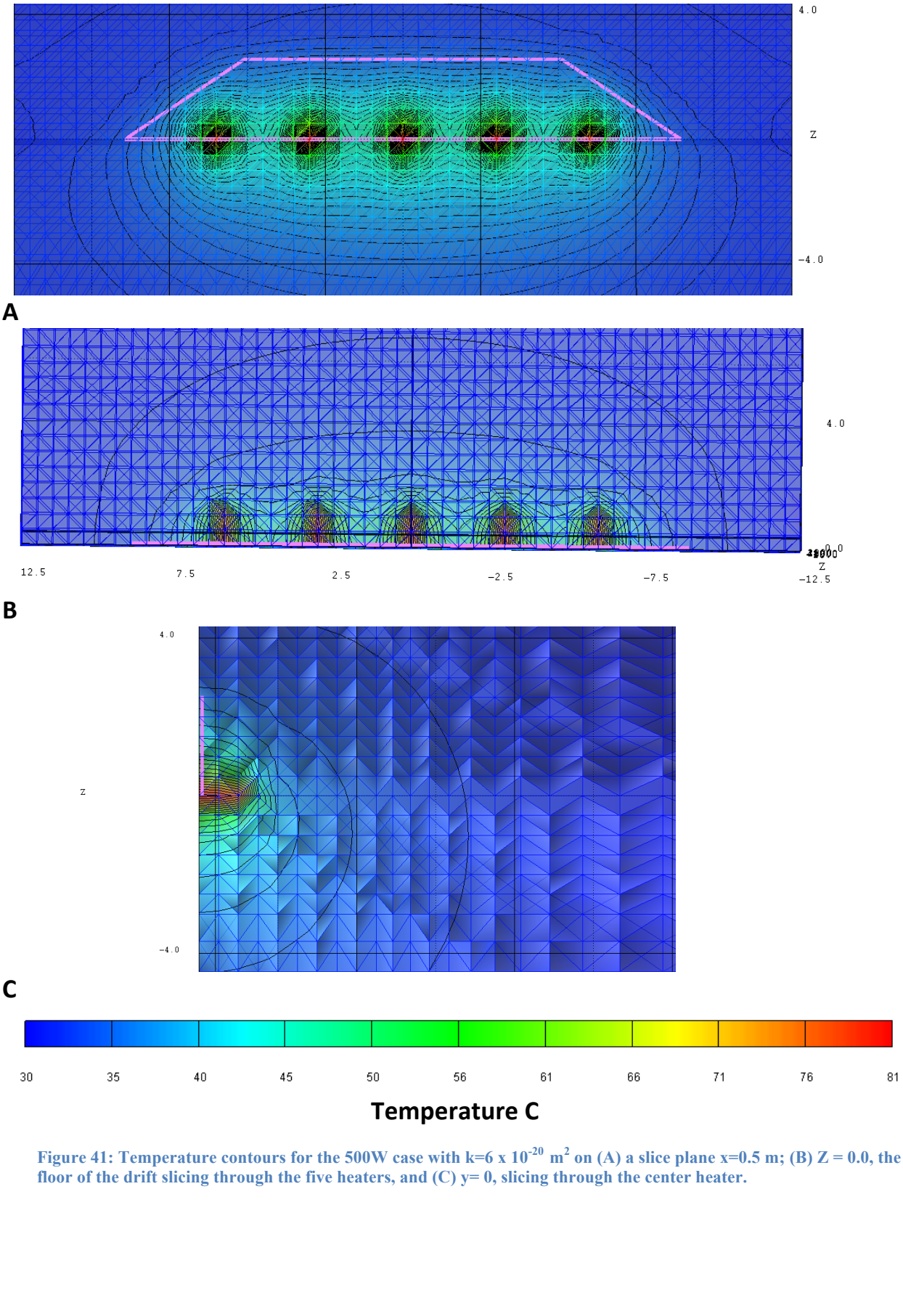

Figure 41: Temperature contours for the 500W case with k=6 x 10^{-20} m^2 on (A) a slice plane x=0.5 m; (B) Z = 0.0, the floor of the drift slicing through the five heaters, and (C) y= 0, slicing through the center heater.

5.2.3 High-Heat simulation (1500W with k= 6 x 10^{-19} m^2)

This section presents results from a very wet, high-thermal-load simulation and with values summarized in the last column of Table 3. Figure 42 shows saturation slices after 1 year of heating. Dry-out is more advanced than in the 500W case, and irregular saturation contours can be seen above the heaters. Interestingly, water is accumulating at the lower tips of the backfill slopes. Water also accumulates between the heaters, with saturations being higher at x=0 (heater center).

The irregular saturation contours evolve through time in a very dynamic manner. However, by two years of heating, water flow into the backfill leads to much less convective vapor transport and only the heater nodes themselves are completely dry (Figure 43). The total amount of water that has seeped into the backfill in two years is 8278 kg, nearly 10 m^3. This amount of water represents a very high estimate of possible scenarios where the drift and subsequent thermal mechanical damage could lead to drainage of a water lens or large fluid filled vug (meter scale). The two-year saturation for this case results in the heaters being surrounded by saturations of greater than 0.4. Figure 44 shows that maximum temperatures for this example are near 200^{o}C.

Figure 45 shows that temperatures are above boiling (105^{o}C) in a region around the heaters, spreading out to about a meter from the heaters. The amount of water in the problem is such that this boiling region does not lead to dry-out; water vapor condenses both vertically and laterally away from the heat source and flows back toward the heaters as liquid water. This result shows that heaters could become surrounded by fairly wet run-of-mine salt at temperatures above 100^{o}C. Additionally, as shown in Figure 46, water vapor pressure in the boiling region stays quite high (>0.1 MPa), meaning that the non-condensible gas has been forced out of this region and the unsaturated pore-space is filled exclusively with water vapor.

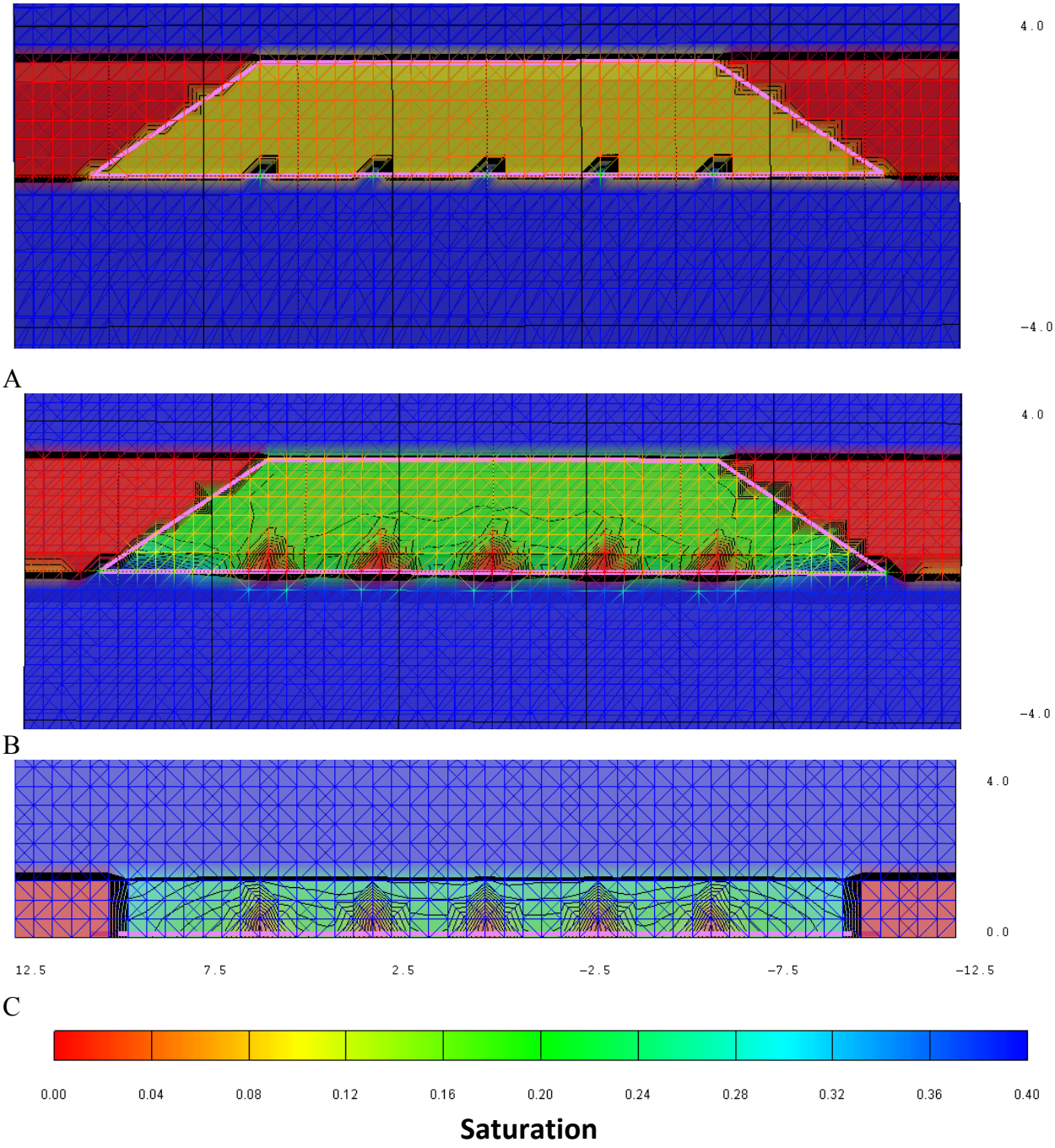

Figure 42: The initial saturation (A) and saturation at 365 days (B) close to the symmetry boundary (x=0.5). (C) shows saturation on the z=0.5 plane, just above the floor of the experimental drift. Results for the 1500W k= 6 x 10^{-19} m^2 case.

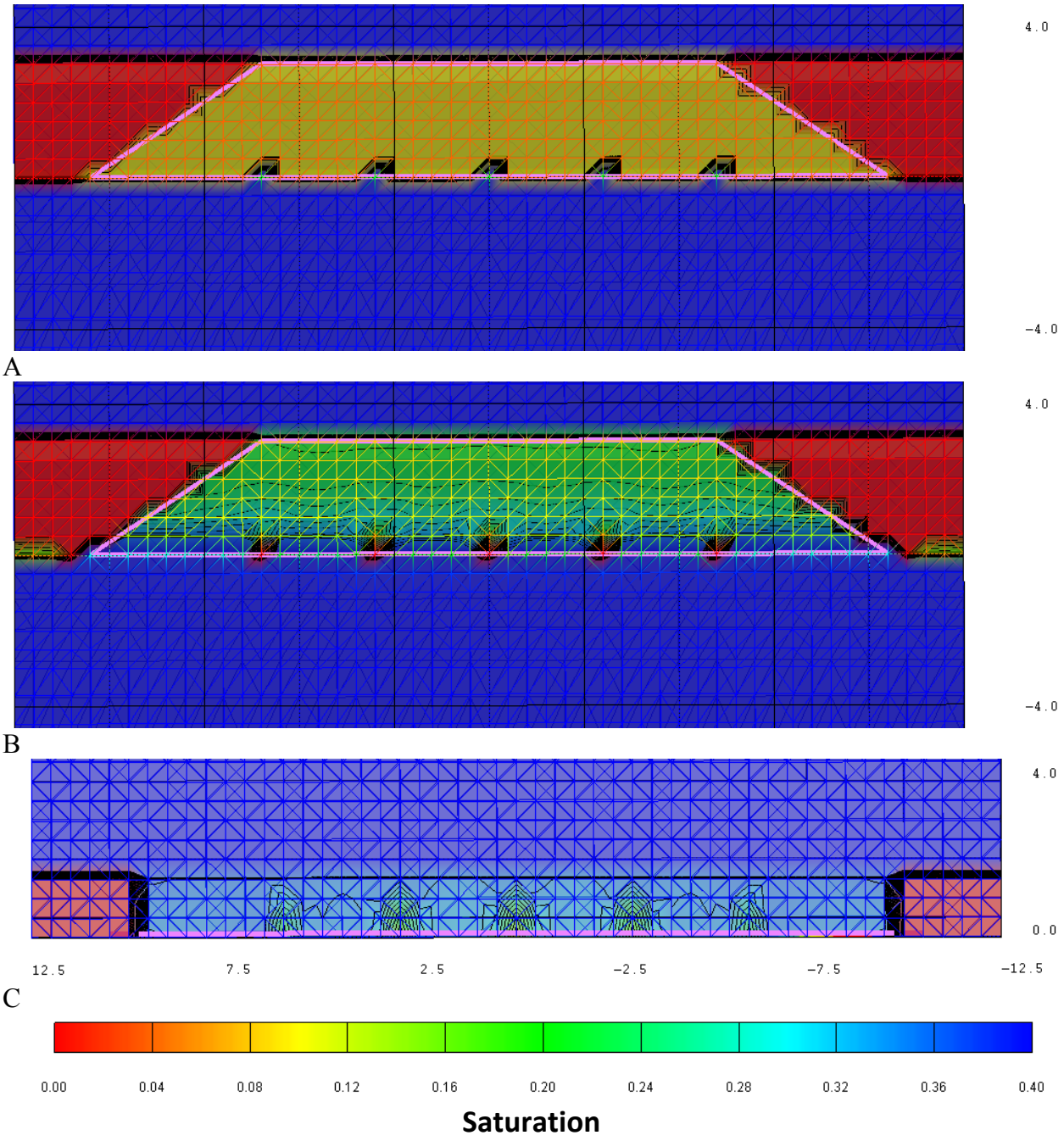

Figure 43: The initial saturation (A) and saturation at 730 days (B) close to the symmetry boundary (x=0.5). (C) shows saturation on the z=0.5 plane, just above the floor of the experimental drift. Results for the 1500W k= 6 x 10^{-19} m^2 case.

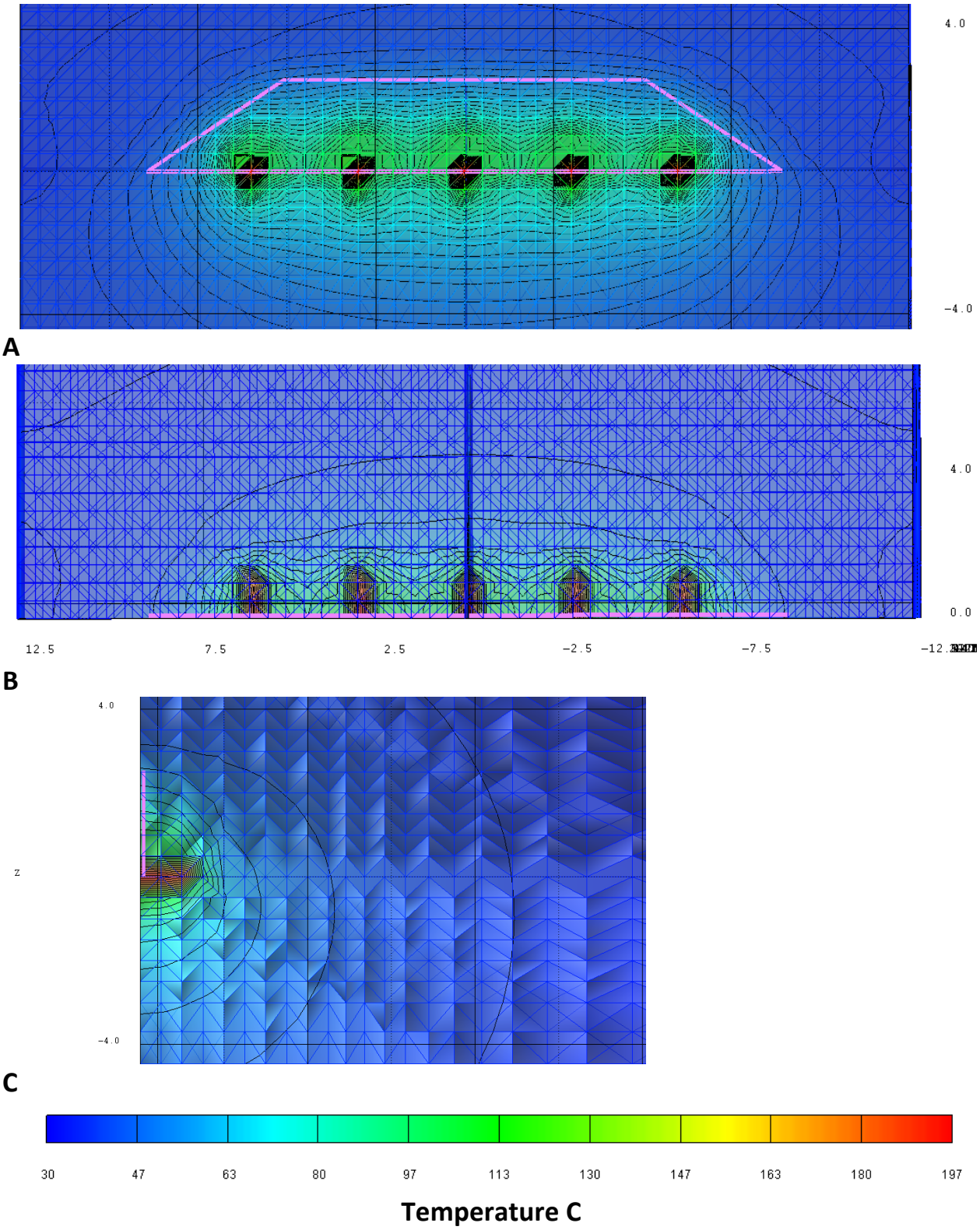

Figure 44: Temperature contours for the 1500W case at 730 days after heating begins, with k=6 x 10^{-19} m^2 on (A) a slice plane x=0.5 m; (B) Z = 0.0, the floor of the drift slicing through the five heaters, and (C) y= 0, slicing through the center heater.

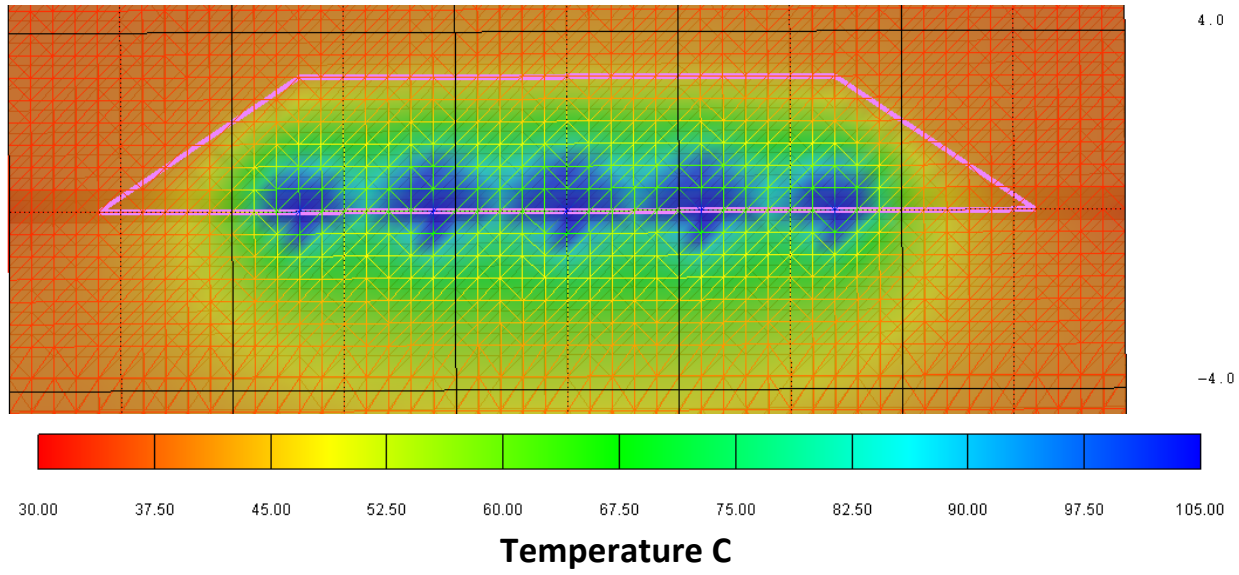

Figure 45: Temperature truncated at 105°C for the 1500W case at 730 days after heating begins, with k=6 x 10^{-19} m^2 on slice plane x=0.5.

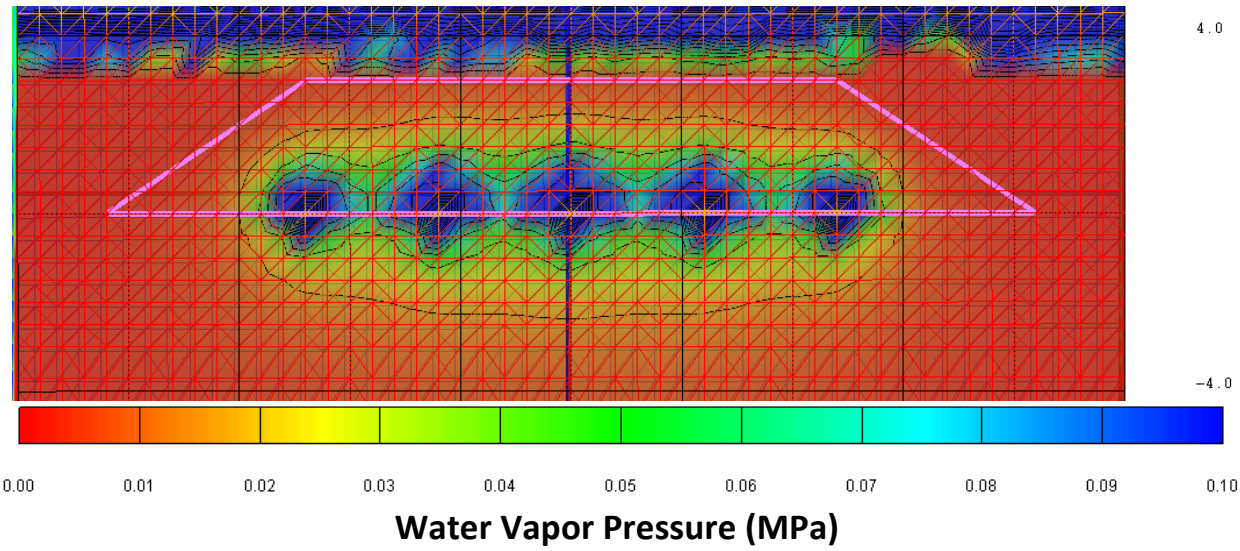

Figure 46: Water vapor pressure truncated at 0.1 MPa for the 1500W case at 730 days after heating begins, with k=6 x 10^{-19} m^2 on slice plane x=0.5.

Finally, we present evidence that the coupled simulations show significant perturbations to temperature fields when compared to thermal only simulations. For this comparison, the extreme case of 1500W with k= 6 x 10^{-19} m^2 was run from the same initial saturation file (50 days) using only the thermal solution. Results from this comparison are shown in Figure 47, which is a zoom in on the three center heaters sliced on the x=0.5 plane. In this figure, maximum temperature is set to 223°C. Maximum temperature in the thermal only solution is 223.2°C, while for the full air-water-water vapor simulation, maximum

temperature is 196.6^{o}C after 2 years of heating. A lower maximum temperature (in the heater) is also seen for the case of 1500W with k= 6 x 10^{-20} m^2; however for this case the maximum heater temperature reaches 211.2^{o}C. The differences in temperature fields are explained by the presence of heat pipes in the multiphase simulations. Heat pipes lead to rates of thermal transport that are higher than achieved through conduction alone. In these simulations, water vapor diffuses away from high concentration regions near the heaters (Figure 46) and eventually condenses back to liquid water. After condensing, some of the water flows back toward the heaters by gravity flow and along capillary pressure gradients where the cycle is repeated.

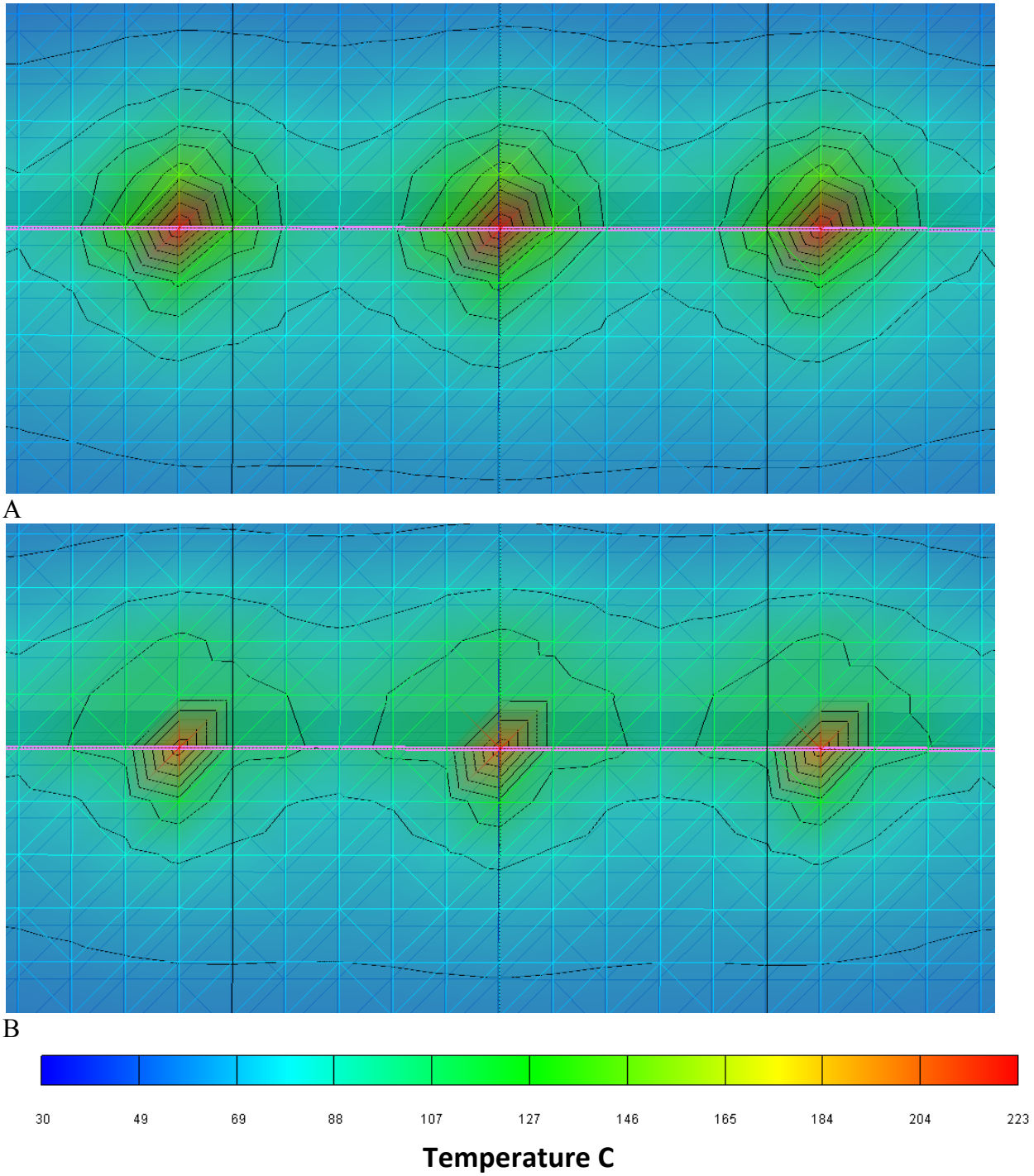

Figure 47: Temperature field for the 1500W case at 730 days after heating begins, with k=6 x 10^{-19} m^2 on slice plane x=0.5. (A) is for thermal conduction only and (B) includes multiphase heat pipe effects. Grid blocks visible as horizontal lines 0.5 m on a side, while diagonal lines show the mesh connectivity. The pink line is along z=0, the center elevation of the heaters.

Figure 48 is included to show the difference in temperature between the cases depicted in Figure 47. Interestingly, the maximum temperature difference between the thermal conduction only versus the heat pipe simulation occurs not at the heater, but on the nodes directly above the heater at z=0.5 m. The maximum positive delta T for this comparison is 44^{o}C directly above the heaters, while the maximum negative delta T is around 10^{o}C and occurs between the heaters. This means that the heat pipe mechanism is redistributing heat vertically as well as laterally, leading to a region with low thermal gradients compared to the conduction only simulation. Such temperature homogenization could be a diagnostic when looking for multiphase impacts in a drift scale experiment.

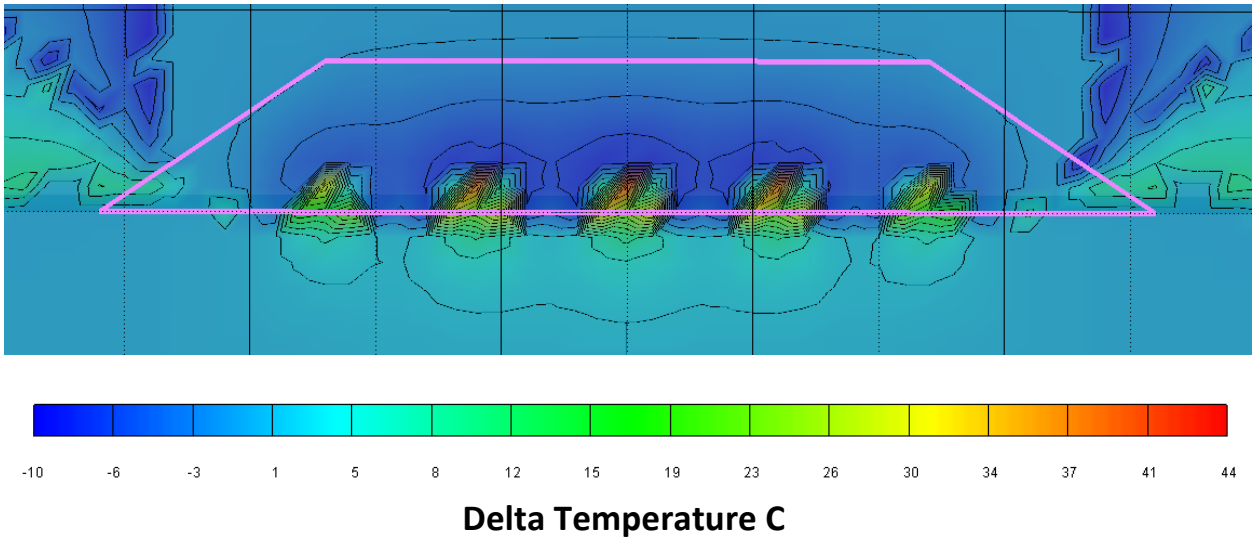

Figure 48: Temperature difference field between the conduction only case and the heat pipe case. (1500W at 730 days after heating begins, with k=6 x 10^{-19} m^2 on slice plane x=0.5).

6. Thermal-Hydrologic-Chemical (THC) Calculations of a Field Scale Heater Test

This section presents results from calculations of coupled thermal-hydrological-chemical simulations designed to highlight the first order effects of many complex coupled processes. FEHM has been updated in this study to allow simulation of several important coupling feedbacks associated with chemical changes during heating. Specifically, as described in Chapter 2, FEHM now allows porosity to change as salt is dissolved or precipitated. Porosity change leads to changes in thermal conductivity, permeability, and water vapor diffusivity. Salinity change with temperature is also included, impacting water vapor pressure and porosity. Changing thermal conductivity impacts temperature gradients. Boiling now leads to precipitation of salt as water vapor is forced away from high temperature regions. Mineral dehydration has also been added to FEHM, allowing temperature rise in clay-bearing salt to produce water. Water produced from dehydration is then added to any existing heat-pipe in the RoM salt.

The goal of this chapter is to describe how the simulations are impacted by the addition of chemical processes, and to investigate uncertainty in primary parameters, such as initial water content of the RoM salt, thermal load from the waste canisters, capillary suction in the RoM salt, and clay content of the RoM salt. Additionally, results from this work will allow more intelligent experimental design (i.e., placement of sensors) for a future thermal test. For example, if measureable changes in porosity are predicted due to the redistribution of salt, the model will inform the process of forensic examination that would confirm this process.

A significant difference with the TH modeling work presented in Chapter 5 is that the current assumption for heater spacing is 0.3 m (1 ft) between waste canisters. The reduced spacing leads to lower thermal loads per canister to stay below a target temperature in the 150 – 200^{o}C range. Also, the current thinking is that a test would have RoM backfill that does not fill the air space above the waste, allowing cooler temperatures from the drift to move across the covered canisters.

In the sections below, a specially constructed numerical mesh is described that was designed to keep high resolution in the RoM salt where porosity changes are most likely. Next, initial and boundary conditions are described, followed by presentation of simulations of various scenarios exploring the impacts of uncertain primary variables on system behavior.

6.1 Drift scale heater test simulation design: Thermal-Hydrological-Chemical (THC) model

The 3-D numerical mesh built for exploring options for a field-scale thermal test contains 117,670 nodes with high resolution in the RoM salt to allow accurate delineation of boiling fronts that move through time and space.

The three-dimensional mesh is a ¼ space representation of the true domain, with reflection boundaries on both faces of Figure 49. The mesh extends from -18.3 to +18.3 m in the z direction, from 0.0 to 18.3 m in the y direction, and from 0.0 to 12.2 m (40 ft) in the x direction. The drift is 3.0 m (10 ft) high and the pile of RoM salt is 1.8 m (6 ft) high. The damaged rock zone (DRZ) is 1.5 m (5 ft) thick surrounding the drift. Material properties and/or initial conditions used in these simulations are shown in Table 4.

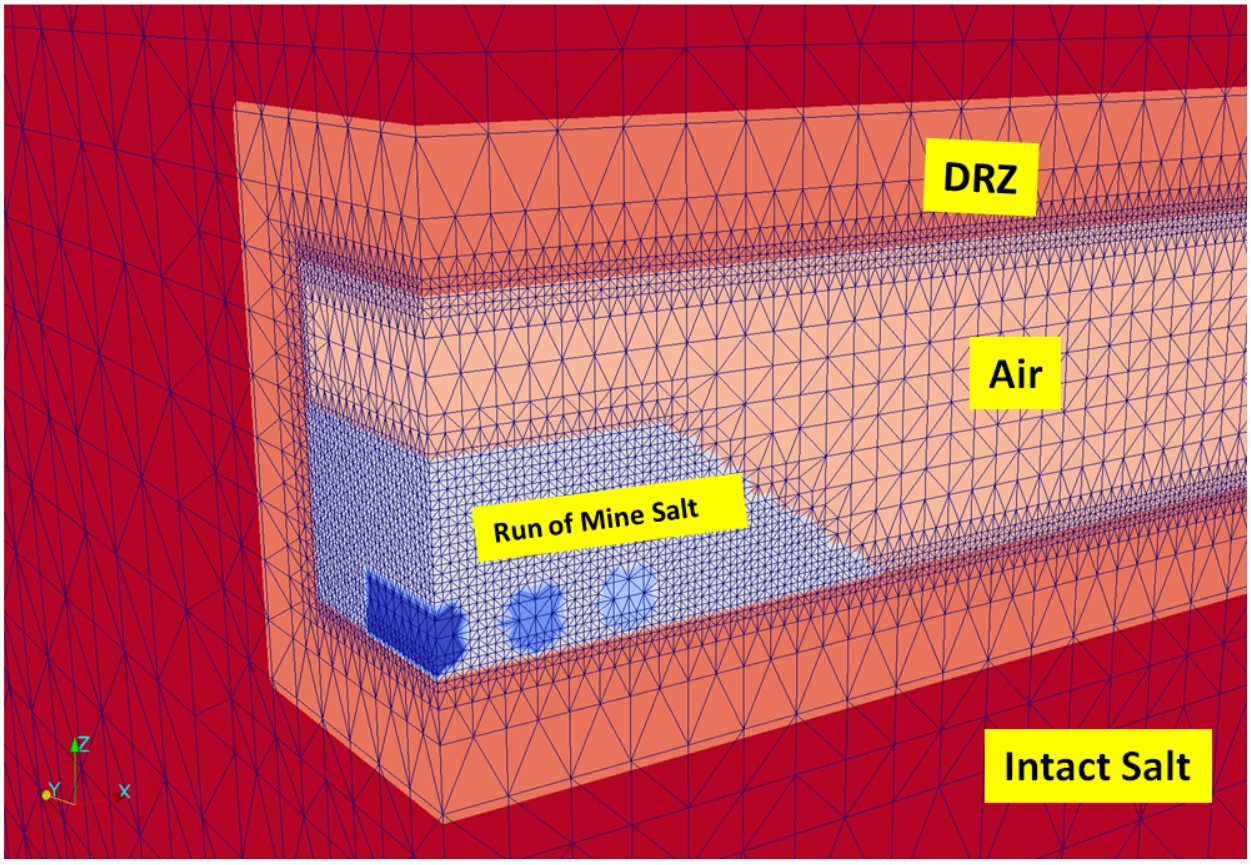

Figure 49: View of the high resolution section of the mesh.

Table 4: Material properties and/or initial conditions for the THC model runs

	Canister	RoM Salt	Air	DRZ	Intact salt
density	2230.	2165.	2165.	2165.	2165.
Thermal cond	1.1	variable	14.0	variable	variable
Heat capacity	710.	931.	0.46	931.	931.
porosity	0.00001	variable 0.35 initial	0.999	0.01	0.001
Saturation	1e-5	0.01 to 0.1	1e-6	1 initial	1
Permeability (m^2)	10^{-21}	variable	10^{-11}	10^{-19}	10^{-21}
Max capillary pressure (MPa)	0.1	0.1 to 1.0	0.001	0.1 to 1.0	0.1 to 1.0
Water vapor diffusion coefficient (m^2/s)	variable	variable	variable	variable	variable
Initial concentration of salt in water Mol/kg	0.0	6.16	0.0	6.16	6.16
Solubility reaction	NO	YES	YES	NO	NO
Clay mass fraction	0	0 – 10%	0	0	0

Air in the simulations is modeled as having a small solid component that helps with numerical stability of the simulations. The air solid density is set to salt density for compatibility with the solubility reaction and heat capacity of the air solid component is reduced to make the product of heat capacity and

density approximately equal to air at 30°C and pressure of 0.1 MPa. The solubility reaction is allowed to progress in the air region, to allow for dry-out of water moving through the air and subsequent deposition of tiny amounts of solid salt on the air-solid component. The air-solid component accounts for 0.1% of the air volume in the simulations and does not impact the results significantly, but this approach facilitates the calculation of this system with a porous medium code like FEHM. Finally, solid salt is modeled as having 17.11 moles of salt per kilogram of solid salt. This value does not change as salt dissolves and precipitates because the porosity change associated with precipitation/dissolution uses this same density.

The simulations are started from an initial state where the far-field pressure of 15 MPa is allowed to equilibrate with the drift pressure of 0.1 MPa. The temperature in these background runs is fixed at 30°C. In the background runs, the saturation in the RoM salt is varied from 0.01 to 0.1 saturation in model sensitivity runs, equivalent to a water fraction by mass of 025% to 2.5% (mass water/mass total). The background runs allow saturation in the DRZ to drop slightly during the initialization period of 60 days, as water is pulled from the DRZ into the RoM salt. However the RoM salt is set to a fixed saturation so no water is added to the initial saturation in this zone. Several initial states are generated ranging across different initial saturations. These initial states are used to start simulations with different combinations of heat loads, capillary pressures, initial saturation in the RoM salt, and clay fractions in the RoM salt.

All simulations of drift heating are run to two years, the assumed length of the heater test. The boiling in salt-saturated solutions is elevated with respect to pure water, and in our simulations occurs at around 110°C. The total volume of the RoM salt pile is 14.4 m^3, and the initial mass of water in this zone at 10% saturation is 500 kg. The simulations are performed in saturation space, while most of the measured data from WIPP is presented in gravimetric water content (Mass of water/ mass of solid salt), obtained by oven-drying the samples. In addition to gravimetric water content, water mass fraction (mass of water/ initial sample weight) is also sometimes used. To facilitate comparisions, Table 5 shows the conversions between these forms of reporting water quantity. The table assumes 35% porosity and a grain density for salt of 2165 kg/m^3.

Table 5: Conversion factors for different methods of reporting quantity of water in salt

Saturation					
0.01	0.02	0.03	0.05	0.1	
1407.25	1407.25	1407.25	1407.25	1407.25	kg salt per cubic meter
3.5	7	10.5	17.5	35	kg water per cubic meter
0.002481	0.00495	0.007406	0.012283	0.024268	water mass fraction
0.002487	0.004974	0.007461	0.012436	0.024871	gravimetric water content
0.0035	0.007	0.0105	0.0175	0.035	water vol fraction

6.2 Results

6.2.1 Porosity change due to temperature

The results below that come from a parameter space evaluation for the fully coupled THC simulations show that a range of behavior can occur in the RoM salt based on availability of both water and heat. One of the primary indicators of changes in behavior is porosity change from the initial 35% (35% is indicated as yellow in the porosity figures below). Figure 50 illustrates the types of porosity change seen in different simulations; in this case the only parameter varied was the heat load in the canisters. For increasing heat loads ranging from 250W to 500W and finally 750W in Figure 50A, B, and C respectively, the porosity changes are significantly enhanced for higher heat loads and temperatures. In all cases there is little water flowing into the RoM salt from the DRZ, the initial saturation of the RoM pile is 10%, and the maximum capillary suction in the RoM salt is 1.0 MPa. As a metric for porosity change, we use the following:

PC_{tot} = sum over all RoM nodes (abs(initial porosity – final porosity).

This metric produces a volume of porosity and sums both gains and losses. For case A, this value is 0.16 m^3, for case B it is 0.46 m^3, while for case C PC_{tot} = 1.18 m^3.

Temperature versus time at locations on the line of maximum temperature (x=0, y=0) show that the middle of the RoM salt (labeled crushed in the figure) reaches only 60°C in the 250W case, while reaching near 110°C in the 750W case (Figure 51). Although the 500W case did not reach boiling at the edge of the canister, there was still enough vapor transport and recirculation of condensate to lead to a significant amount of porosity change (PC_{tot} = 0.46).

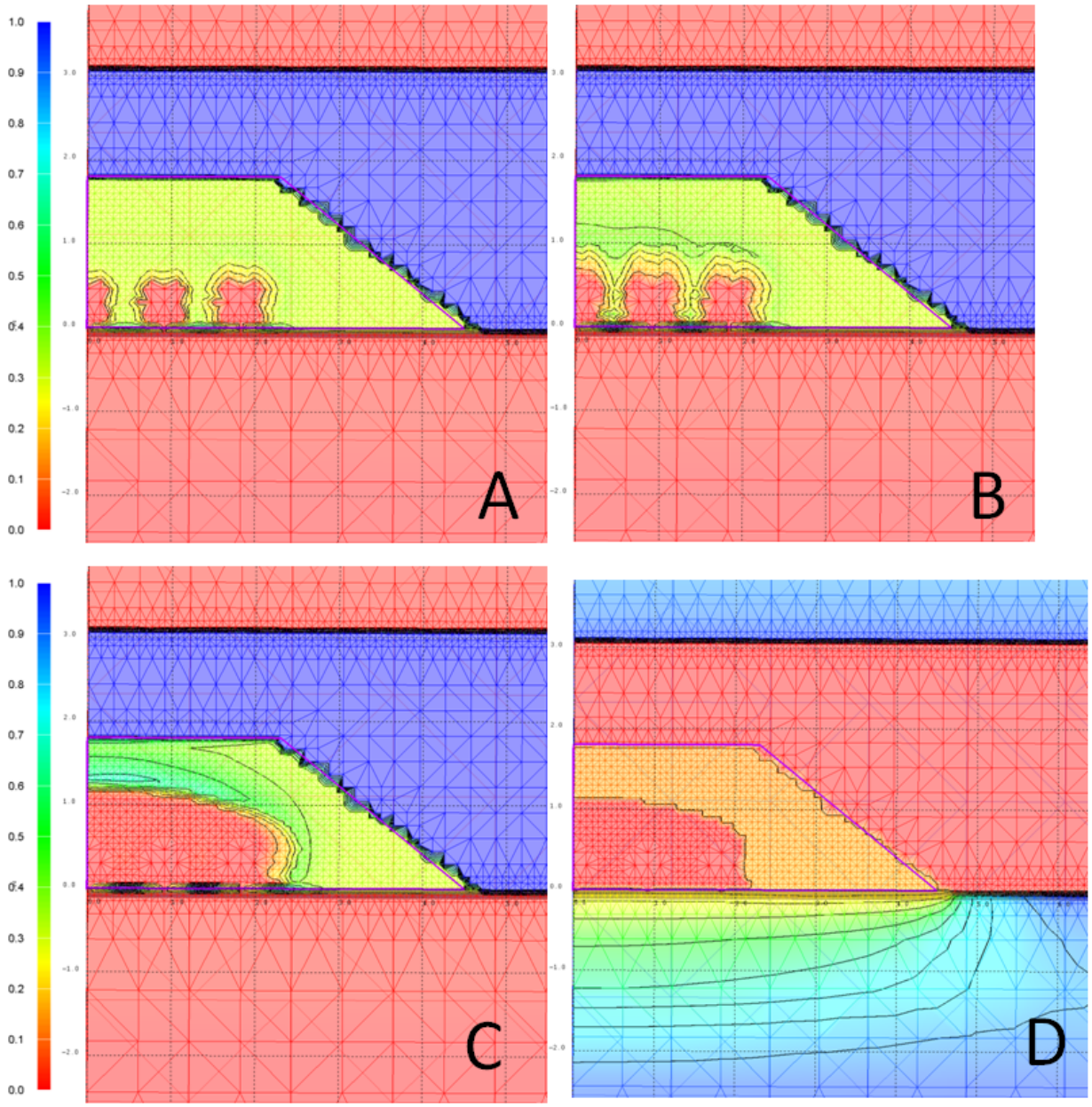

Figure 50: Porosity after 2 years of heating for A) 250W B) 500W and C) 750W per heater. D) Saturation corresponding to the porosity in C.

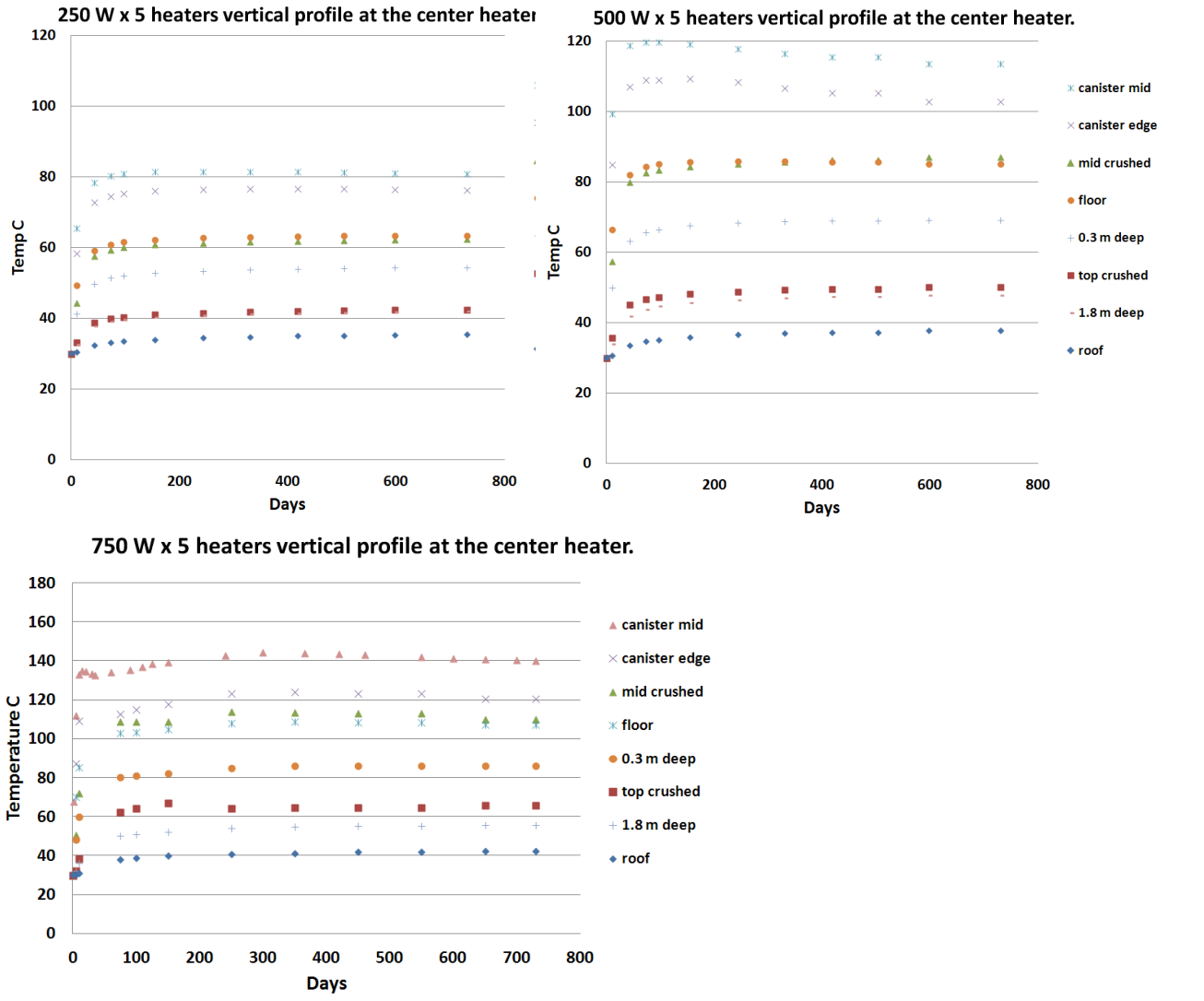

Figure 51: Temperature versus time for A) 250W B) 500W and C) 750W per heater.

The large changes in porosity seen in the 750W case are caused by the creation of a heat pipe that pushes purified water vapor away from the heat and pulls saturated brine back towards the heat by capillary suction from wetter regions to the very dry region that develops around the heaters. The dry-out region can be seen in Figure 50D.

Although tests have not been performed in this configuration, there is experimental evidence for mass redistribution and porosity change in heated salt from 1980s heater tests in Room B (Krumhansl et al., 1991). In these tests, 24 in. diameter canisters were placed into 36 in. diameter boreholes and heated to about 130°C. One borehole was not backfilled, one was backfilled with crushed salt, and two were

backfilled with a mixture of bentonite and sand. In the cases with crushed salt backfill and open space, after the heater test, the heaters were found to be enclosed in solid rock salt with final bulk density within 99% of that of intact salt (2160 kg/m^3) (Krumhansl et al., 1991). Figure 52 shows the heater, post-experiment, from borehole BO45 with crushed salt backfill (Brady et al. (2013). The porosity of the crushed salt has been greatly reduced (Krumhansl et al., 1991). In the case of the test with no backfill (borehole BO42), a 0.2 to 2 in. skin of salt was formed around the heater from evaporating brine. The likely cause of the porosity redistribution is heat pipe formation with liquid re-supplied by fluids seeping from the intact salt around the borehole. Fluids collected from BO42 during the experiment indicated a rate of brine influx to the borehole of about 60 mL/day (Krumhansl et al., 1991, Figure 2B).

Figure 52: Heater from borehole BO45 showing porosity reduction as a likely result of heat pipe activity (Krumhansl et al., 1991). From Brady et al. (2013).

6.2.2 Porosity change as a function of initial saturation

Another set of simulations demonstrates the impact of available water on porosity redistribution (Figure 53). For these three simulations, the heat load is constant at 750W per canister and the maximum capillary suction in the RoM salt is 0.5 MPa. In these simulations, the maximum temperature is higher in

the dry cases, with the 1% saturation leading to maximum temperature of 19^{o}C at 2 years, while the 10% saturation case reaches only 14^{o}C (Figure 54). In all of the cases in Figure 53 the dry-out region is approximately the same as seen in Figure 50D, with the drier initial condition simulations having slightly larger dry-out envelopes. The PC_{tot} for these cases is A = 0.22, B = 0.19, C = 0.38, D = 1.17. Although cases A and B are nearly the same, at this time we do not understand why Case A has slightly more total porosity transport than Case B. Interestingly, the temperature profiles are consistent for most of the domain, deviating only near the waste canisters, with marked differences between the wet initial condition that created a heat pipe and the other initial states that do not (Figure 55).

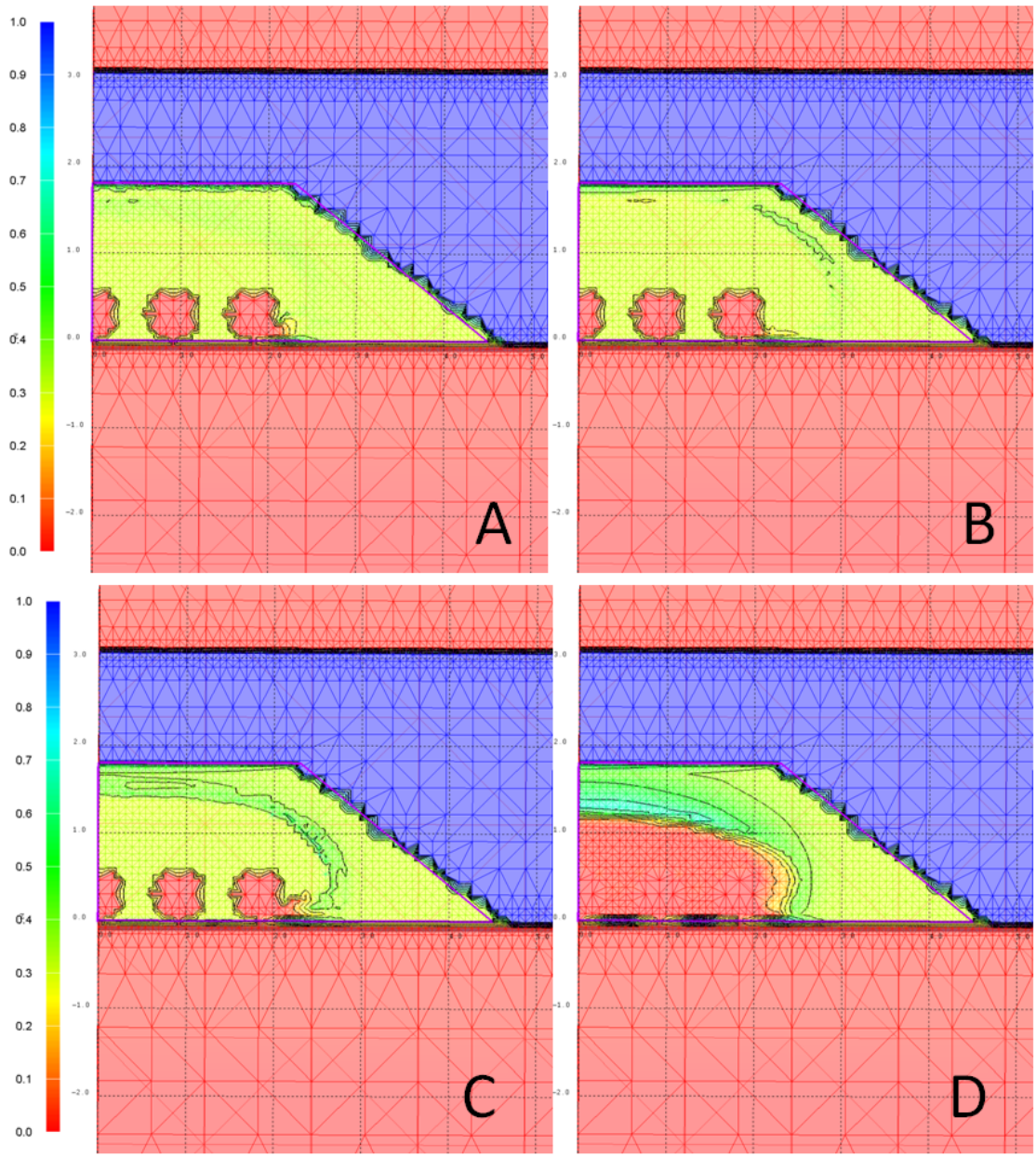

Figure 53: Porosity after 2 years for cases with initial saturation varying from A = 1%, B = 3%, C = 5%, and D = 10%. Heat load in all cases is 750W.

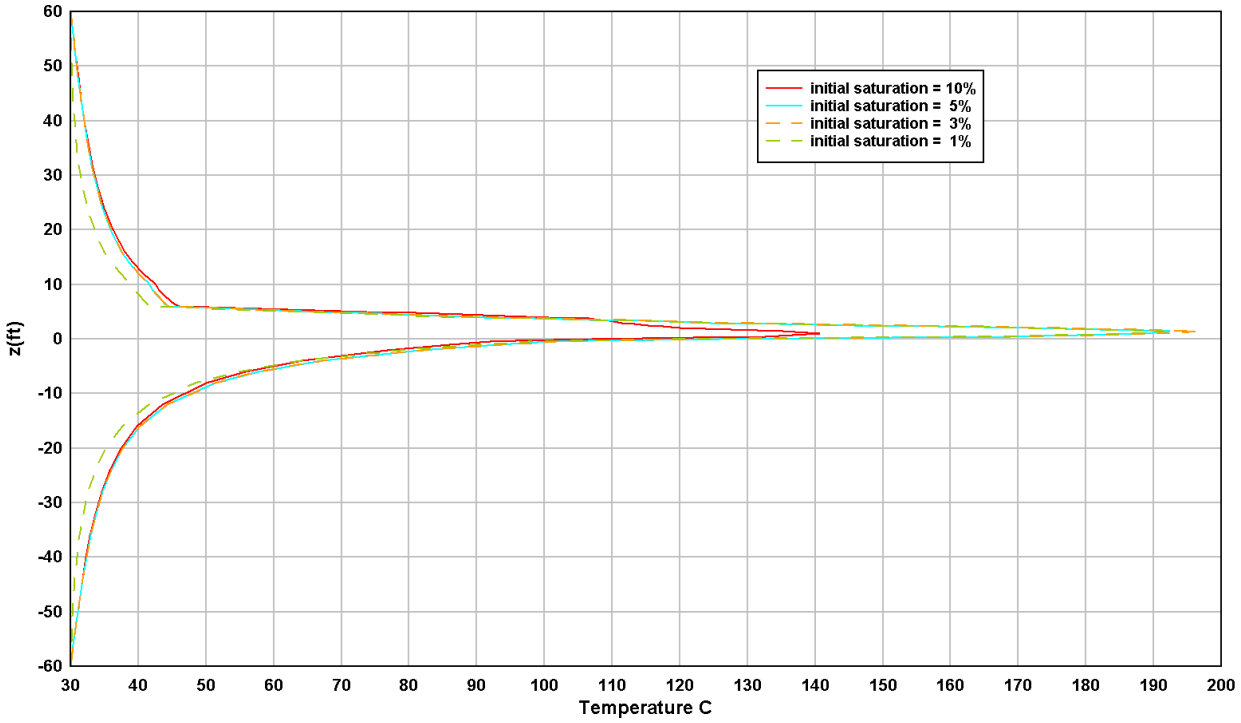

Figure 54: Temperature profile at X=0, Y=0 after 2 years for cases with initial saturation varying from A = 1%, B = 3%, C = 5%, and D = 10%. Heat load in all cases is 750W. Z units switched to feet for conformity with the engineering drawings.

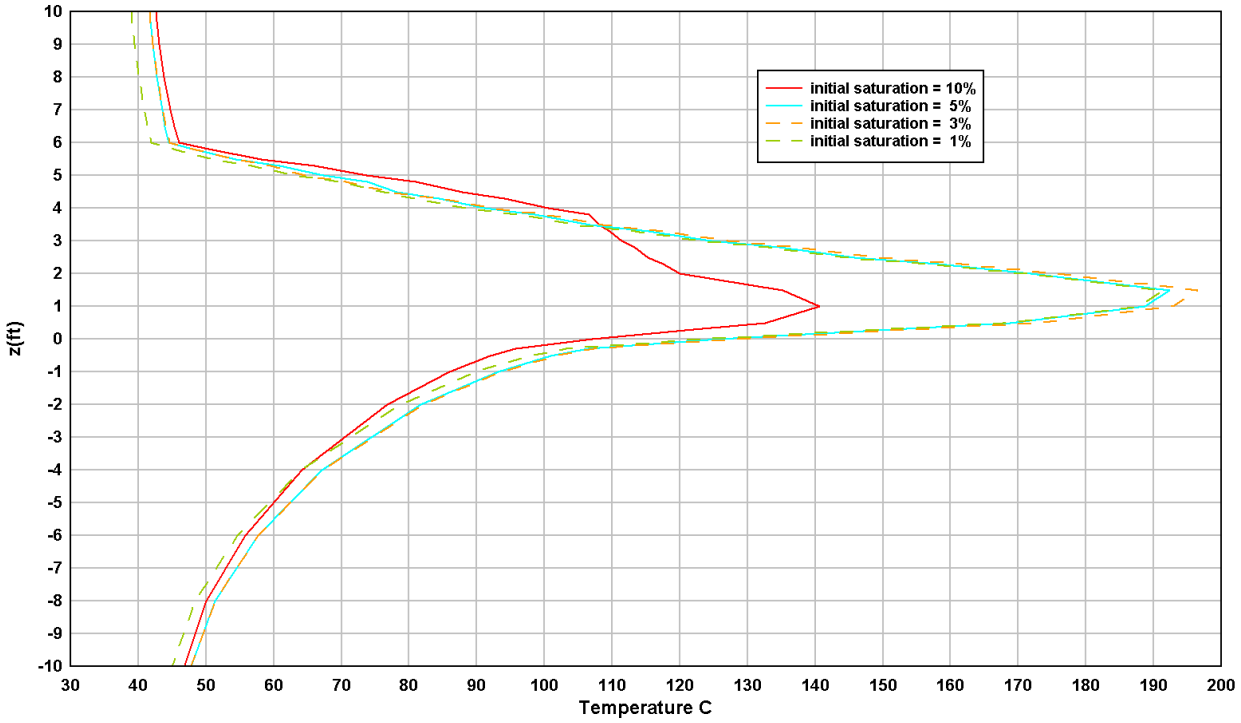

Figure 55: Temperature profile at X=0, Y=0 (zoomed in on the region +-10 ft of the drift floor) after 2 years for cases with initial saturation varying from A = 1%, B = 3%, C = 5%, and D = 10%. Heat load in all cases is 750W. Z units switched to feet for conformity with the engineering drawings.

6.2.3 Porosity change as a function of capillary suction in the RoM salt

Capillary suction impacts the available water in the RoM salt through interactions with the DRZ beneath the pile. For greater suction, more water can be pulled into the RoM salt, providing more drive for the heat pipe. Similarly, more suction allows the heat pipe to strengthen, as increased suction is more efficient at pulling saturated brine back towards the hot region. Figure 56 shows how (A) varying from 0.5 MPa of maximum suction in the RoM salt to (B) 0.1 MPa impacts the two year porosity distribution. The PC_{tot} for these cases is A = 0.38, B = 0.29. In both cases the initial saturation is 5% with 750W canisters.

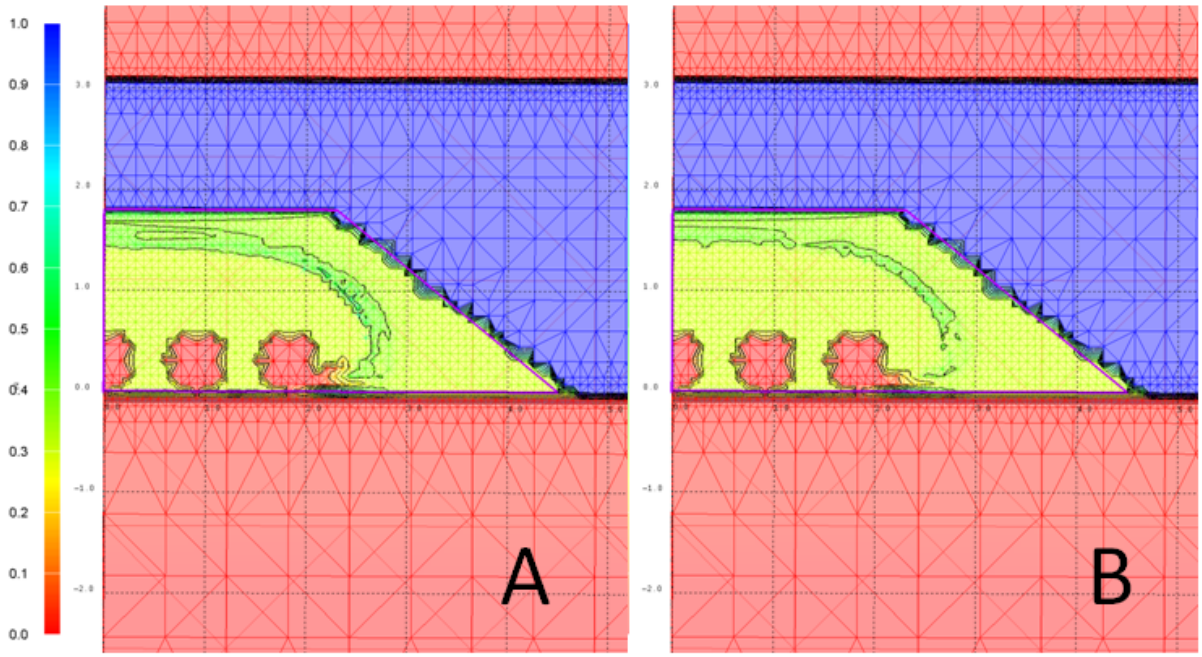

Figure 56: Porosity after 2 years for cases with maximum capillary suction in the RoM salt varying from A = 0.5 MPa to , B = 0.1 MPa. Heat load in both cases is 750W. Initial saturation is 5%.

6.2.4 Porosity change as a function of clay fraction

The effect of clay dehydration in the full three-dimensional model was tested and compared to corresponding cases without clay. All simulations in this section assumed 750W heaters. Clay dehydration was only added in the crushed salt zone, with percentages of clay ranging from 1 to 10% in different simulations. Temperature and saturation for three crushed salt nodes above one of the heaters versus time for the case with 10% clay fraction are shown in Figure 57. The closest node to the heater (z = 0.61 m) reaches 64^{o}C and releases water at 2.2 days. This node reaches 110^{o}C at 8.8 days and more

water is released, but the released water goes directly to the vapor phase and there is a dip in temperature as the water is boiled. The next nearest node to the heater (z = 0.99 m) reaches 64°C and water is released but the node does not reach 110°C in the time of the simulation. The furthest node from the heater does not reach 64°C and thus releases no water.

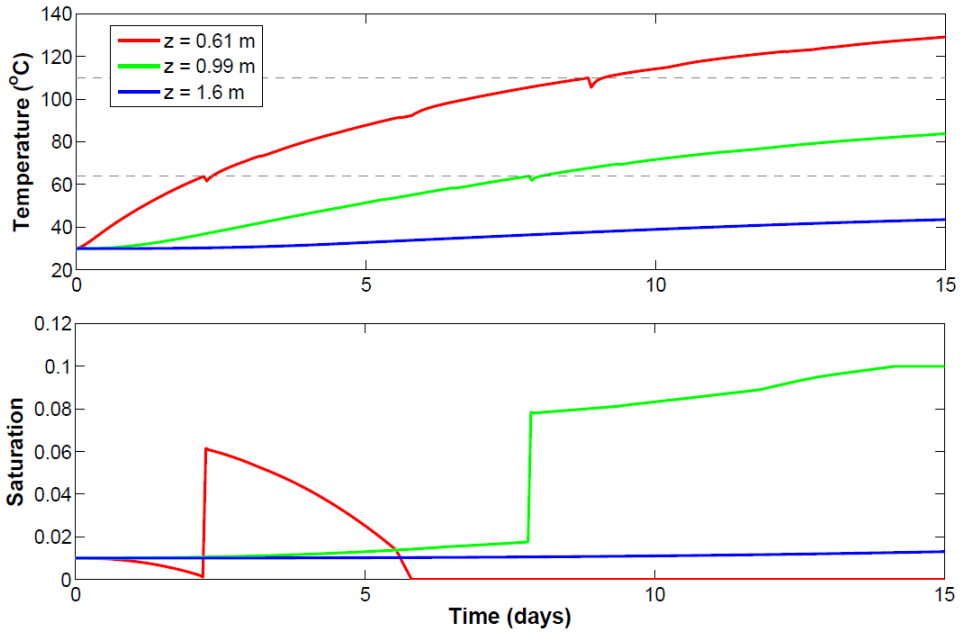

Figure 57: Temperature and saturation for three nodes with increasing distance from heater 1 in the simulation with 10% clay in the crushed salt, initial saturation of 1%, and 0.2 MPa maximum suction.

The saturation, porosity, and temperature differences at 460 days between 10% clay and the corresponding simulation with no clay (both with initial saturation 1% in the crushed salt and 0.2 MPa maximum capillary suction) are shown in Figure 58. The purpose of this comparison is to determine whether the simulated water release from a material with high clay content will make the difference between heat pipe dry-out (as seen in the 1% initial saturation case) and an active heat pipe that contributes to porosity reduction around the heaters. The amount of water produced in the simulation with 10% clay in the crushed salt pile is 119 kg by 460 days. In comparison, the case that starts with 10% initial saturation has ~500 kg more water in the crushed salt than the case with 1% initial saturation. Therefore, the 10% clay case produces an intermediate amount of water and the timing of water release is staggered for the nodes across the crushed salt pile.

In Figure 58(a), a ring of higher saturation persists outside the boiling region in the case where clay dehydration releases a source of water, but it is not enough water to sustain a vigorous heat pipe as in the 10% initial saturation case. The porosity difference between the clay and no clay cases, Figure 58(b),

shows the small amount of salt buildup (porosity reduction) in the wetter case with clay dehydration. Temperatures are generally cooler for the wetter case, Figure 58(c), as seen above (section 6.2.2).

The choice of maximum capillary pressure at zero saturation has an effect on the simulations as before with no clay. Figure 59 shows the difference in saturation at 460 days between the case with 0.2 MPa and 1 MPa maximum suction. (In the equivalent case with 1% initial saturation and 1 MPa suction with no clay, the simulation did not complete because very low saturation/high suction simulations sometimes suffered numerical difficulties. With clay, on the other hand, dehydration releases sufficient water to propel the simulation to completion.) The case with greater suction leads to reduced saturation in the intact salt below the crushed salt pile, slightly increased saturation in the intact salt of the drift ceiling, and increased saturation in the halo outside the boiling front. However, the greater saturation in the crushed salt pile is still not enough to drive a vigorous heat pipe.

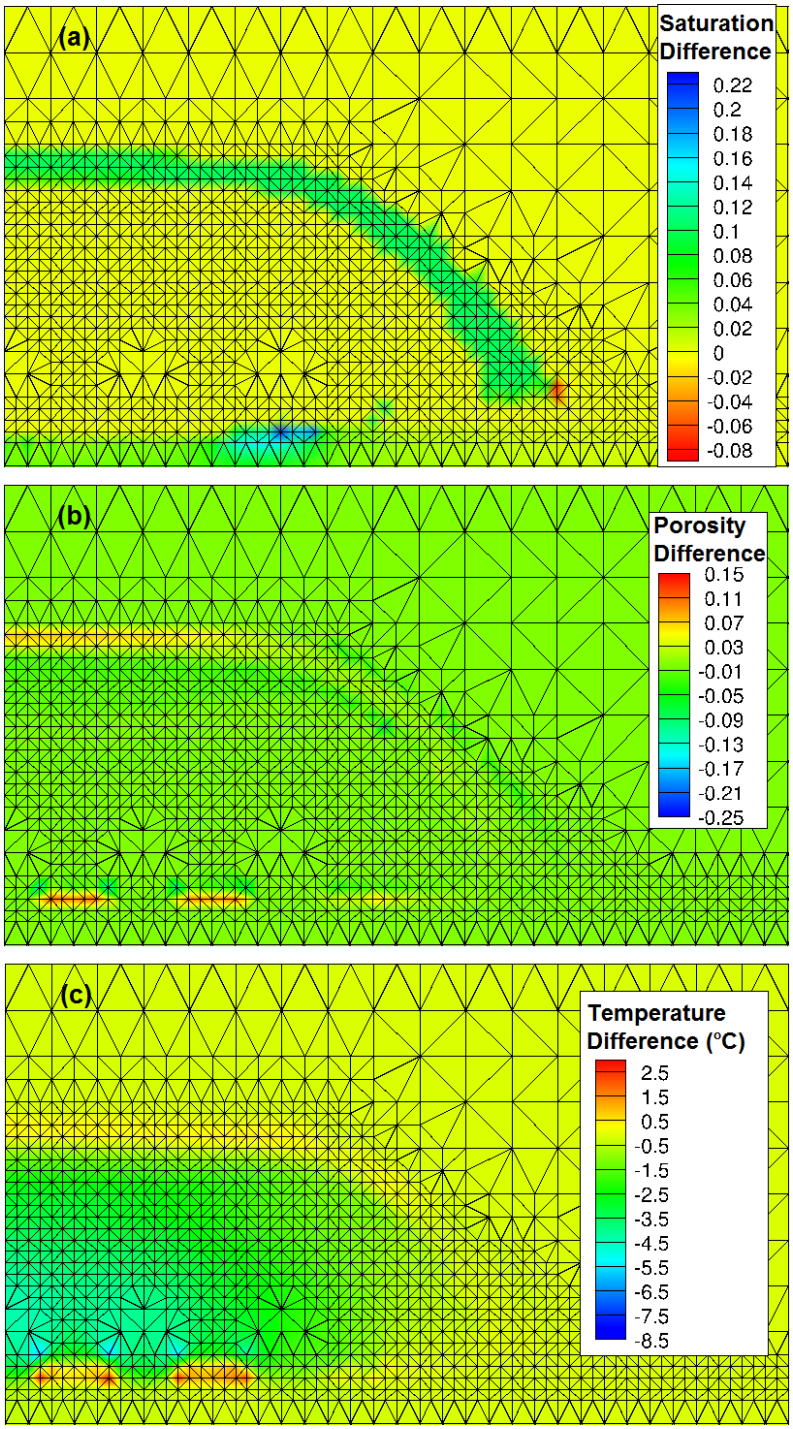

Figure 58: Differences of 10% clay minus no clay at 460 days for simulations with initial saturation of 1% and maximum suction 0.2 MPa: (a) saturation, (b) porosity, and (c) temperature.

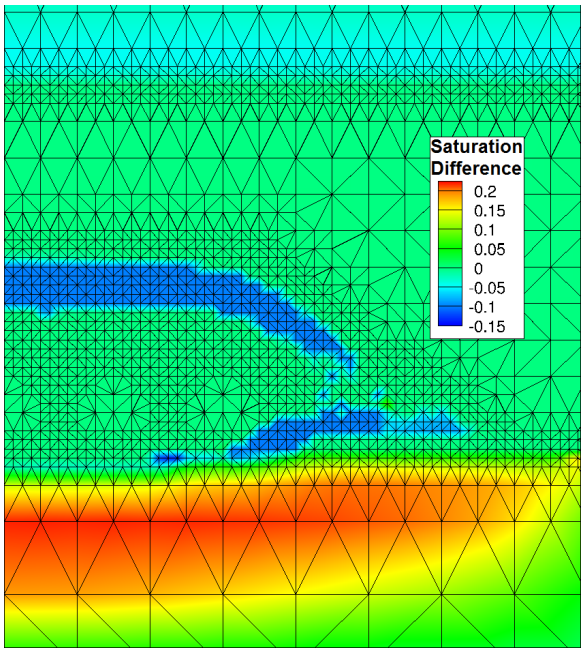

Figure 59: Saturation difference of 0.2 MPa minus 1 MPa maximum suction at 460 days; both cases with 10% clay and initial saturation of 1% in the crushed salt

6.2.5 Other interesting output and graphs.

The porosities and vapor fluxes at 460 days are shown in Figure 60 for five cases, ranked in order of increasing vigor of the heat pipe activity (i.e., drier to wetter in the crushed salt pile). Saturation and liquid fluxes at 460 days are shown in Figure 61. The five cases are:

(a) Initial saturation of 1%, no clay, maximum suction 0.2 MPa
(b) Initial saturation of 1%, 10% clay, maximum suction 0.2 MPa
(c) Initial saturation of 5%, no clay, maximum suction 0.2 MPa
(d) Initial saturation of 10%, no clay, maximum suction 0.2 MPa
(e) Initial saturation of 10%, no clay, maximum suction 1 MPa

By 460 days, the low initial saturation case with no clay shown in Figure 60(a) has no porosity change around the heaters from brine migration, precipitation, and dissolution (i.e., no heat pipe). The case with 10% clay, which has an additional 119 kg water released into the crushed salt pile from dehydration, shows slight changes in porosity around the bases of the heaters [Figure 60(b)]. This is a similar result as the case with no clay but 5% initial saturation in the crushed salt pile [Figure 60(c)], which has ~200 kg additional brine in the crushed salt compared to the driest case in Figure 60(a). On the other hand, the case with 10% initial saturation in the crushed salt and no clay has an active heat pipe with greatly decreased porosity around the heaters and a halo of increased porosity at the boiling front [Figure

60(d)]. Comparatively, this case has ~500 kg more water in the crushed salt than the case with 1% initial saturation. The greatest heat pipe activity is seen in the case with higher suction (1 MPa) in Figure 60(e).

The differences in saturation in Figure 61 reflect the differing temperatures of the wetter and drier cases. As discussed above, the drier cases are hotter and the boiling front extends farther into the crushed salt pile.

Even with a large mass fraction of clay (10%) added to the crushed salt in a case with 1% initial saturation, behavior is more like the dry cases, particularly because the timing of water release is staggered and moves outwards from the heater as more and more nodes reach the dehydration temperatures. Clay dehydration is still an important factor to improve in the model, however, as significant differences in brine fluxes are found in boreholes that cross clay layers (Kuhlman and Malama, 2013). In the case of discrete clay layers, dehydration leads to clay shrinkage and may create enhanced permeability pathways between higher-pressure regions and the lower-pressure excavated spaces. This will be investigated in future versions of the model.

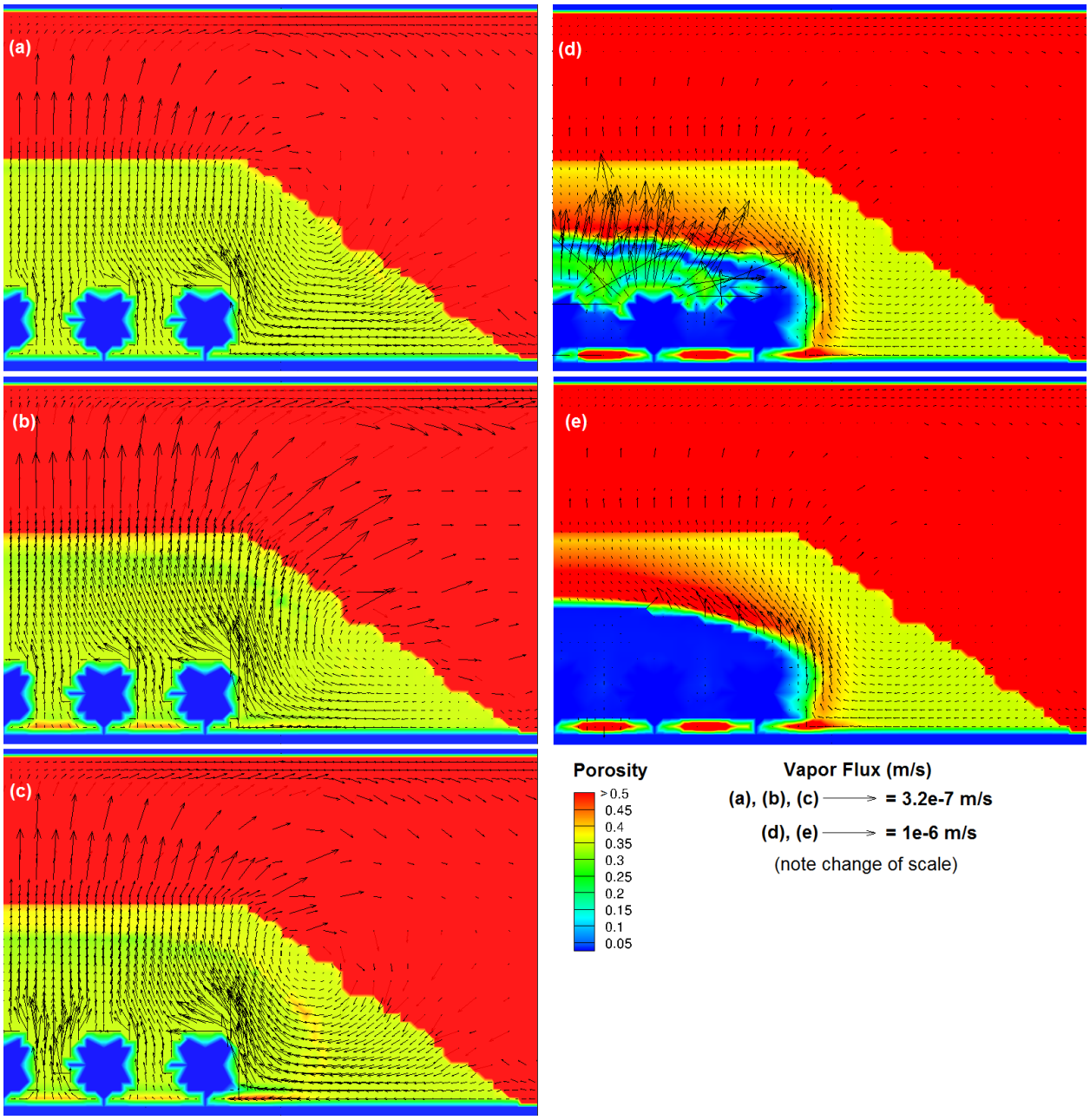

Figure 60: Porosity and vapor flux at 460 days for the following cases: (a) initial saturation of 1%, no clay, maximum suction 0.2 MPa; (b) initial saturation of 1%, 10% clay in crushed salt, maximum suction 0.2 MPa; (c) initial saturation of 5%, no clay, maximum suction 0.2 MPa; (d) initial saturation of 10%, no clay, maximum suction 0.2 MPa; and (e) initial saturation of 10%, no clay, maximum suction 1 MPa.

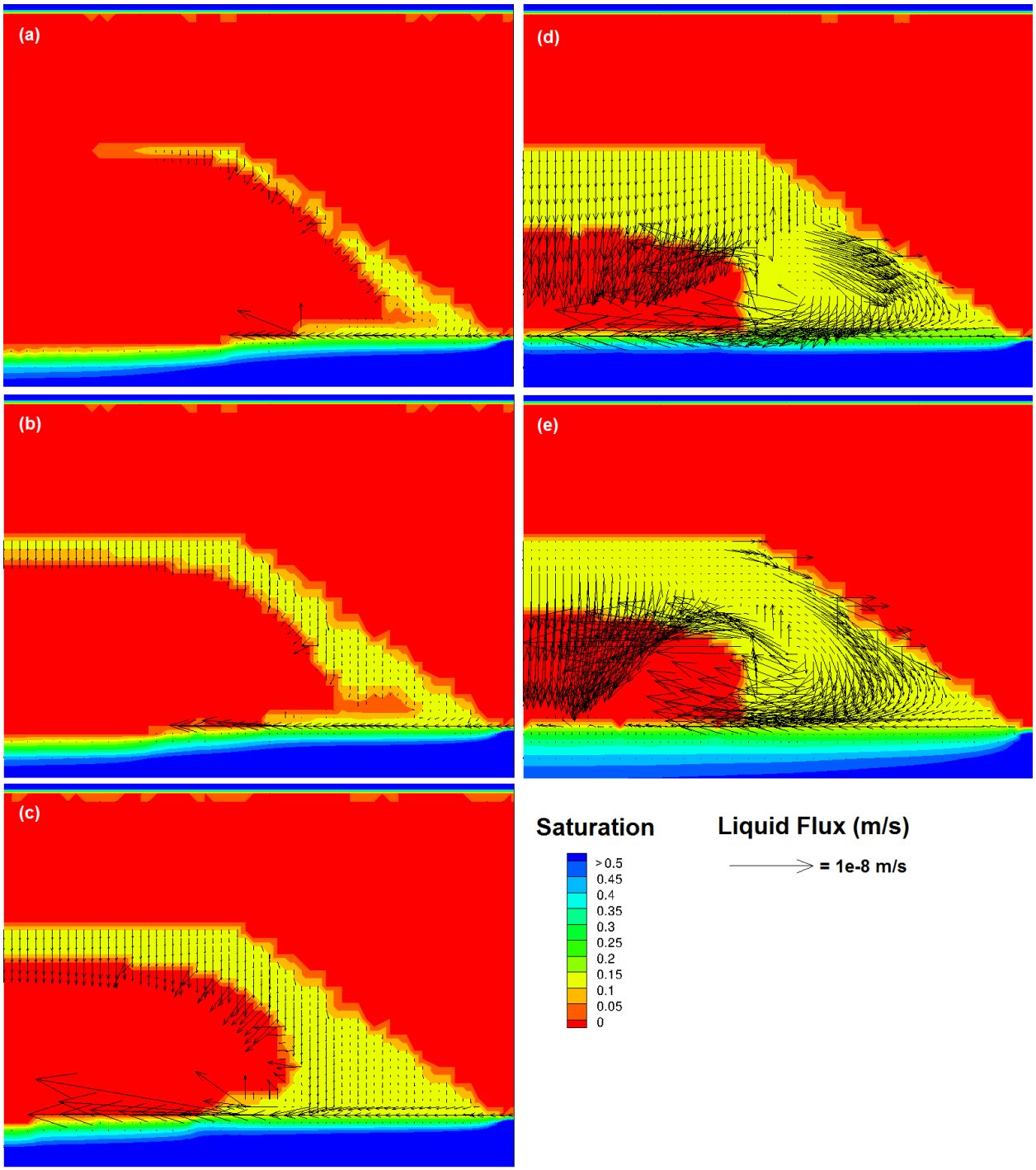

Figure 61: Saturation and liquid flux at 460 days for the following cases: (a) initial saturation of 1%, no clay, maximum suction 0.2 MPa; (b) initial saturation of 1%, 10% clay in crushed salt, maximum suction 0.2 MPa; (c) initial saturation of 5%, no clay, maximum suction 0.2 MPa; (d) initial saturation of 10%, no clay, maximum suction 0.2 MPa; and (e) initial saturation of 10%, no clay, maximum suction 1 MPa.

7. Uncertainty Quantification for a Generic Salt Repository

The complexity of the coupled THC processes controlling the behavior of a salt repository presents challenges regarding the interpretation of the results. For such a complex system, it is difficult to unravel the processes to determine which parameters contribute the most to the overall uncertainty with respect to a given metric. In this chapter, a numerical model is set up to examine these uncertainties for the early-time behavior of a generic salt repository with waste emplaced using the in-drift disposal concept.

7.1 Numerical mesh and simulation set-up

Morris method (Morris, 1991) sensitivity analyses on a model of a generic salt repository are presented here. The Morris method is a one-step-at-a-time (OAT) approach to global sensitivity that is useful for identifying elementary effects, curvature, and interaction of parameters with a limited number of simulations (i.e. the sampling scheme is economical). The Morris method performs a sampling of elementary effects for each parameter, where an elementary effect is the normalized change in model output given two values of a single parameter (change in output divided by change in input parameter). Parameter-set samples are selected in such a way that the sample mean and variance of the computed elementary effects for each parameter are unbiased estimates of the mean and variance of their underlying distribution.

For the model domain presented in Figure 62, reflection (no-flow) boundaries allow the effects of the entire waste canister to be modeled by explicitly modeling ¼ of the waste canister. Reflection boundaries are applied to the two broad vertical sides and front of the model in Figure 62, resulting in an infinite line of heaters. The remaining vertical back side (i.e. thin side out of view) and top and bottom are modeled as far-field boundaries. Allowing the simulation to run without heat for 2 weeks creates initial conditions. Heated simulations are run up to 2 years with decaying enthalpy in the waste according to a half-life of 30 years, based on the half-lives of Cesium-137 (30.17 y) and Strontium-90 (28.90 y). The mesh contains 12,877 nodes discretized from 4 ft (1.2192 m) in the intact salt down to 1 ft (0.3048 m) in the drift (air, RoM salt, and waste).

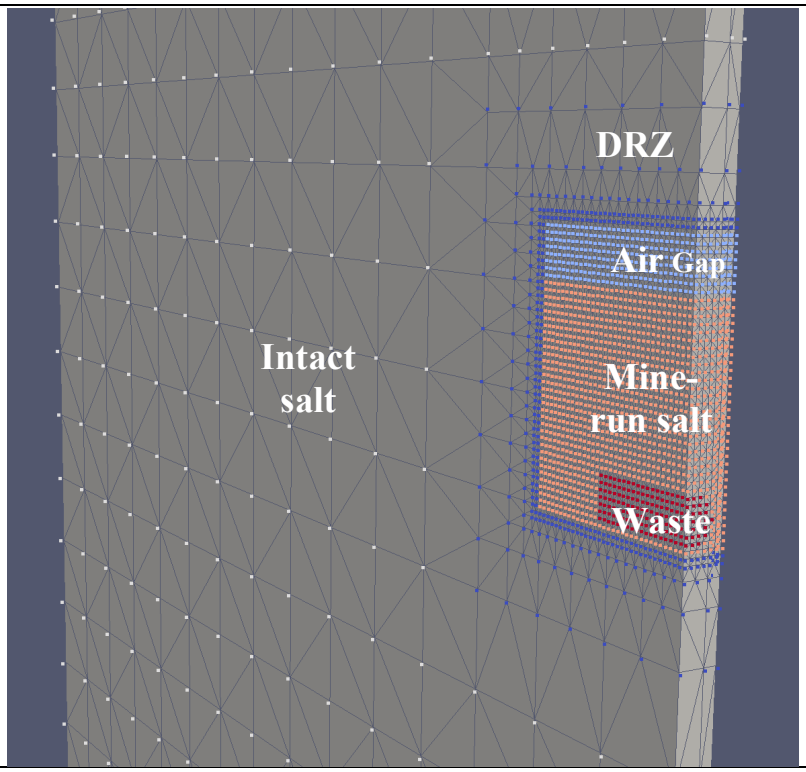

Figure 62: Mesh (nodes and connectivity) representing an infinite line of heaters. Reflection (no-flow) boundaries allow ¼ of one waste canister to be modeled explicitly. Reflection boundaries also account for the infinite line of canisters. Node coloring identifies regions.

Nine parameters were selected for the Morris method. Table 6 lists the nine parameters selected for the Morris method, their ranges and provides a brief description. Initial values of RoM porosity, f_{mri}, and volumetric water content, VWC_{mri}, will change due to precipitation and dissolution. Initial RoM saturation is defined as VWC_{mri} / f_{mri}. This saturation value is fixed in the mine-run salt during the two-week initialization simulation. Parameter ranges were selected based on (1) expected values in domal and bedded salt formations, (2) ensuring that the algorithms implemented in the code are exercised, and (3) ensuring numerical stability of the simulations.

The Morris method implementation in R's package 'sensitivity' (Pujol, 2013) was used here. Three elementary effects were extracted for each parameter, resulting in 30 samples ($r*(k+1)$, where r is the number of elementary effects and k is the number of parameters). The parameter levels were selected to ensure that appropriate values were used (e.g. 5 levels were specified for h_{mr} to ensure that only integer values were selected [4,5,6,7, and 8 ft] as required by the mesh discretization).

Table 6: Parameter ranges used in the Morris method sensitivity analysis.

Parameter	Lower Bound	Upper Bound	Description
f_{drz}	1	2	Order of magnitude of damage used to increase the porosity and permeability of the DRZ [-]
$k_{h,is}$	-22	-20	Log10 permeability of intact salt [log10 m^2]
ϕ_{is}	0.00001	0.0001	Porosity of intact salt [-]
ϕ_{mri}	0.3	0.4	Initial porosity of mine-run salt [-]
$k_{t,air}$	1	20	Effective thermal conductivity of air in the air gap [W/m*K]
E	50	600	Enthalpy of the total waste canister [W]
VWC_{mri}	0.005	0.035	Initial volumetric water content of the mine-run salt [-]
h_{mr}	4	8	Height of mine-run salt pile above adit floor [ft]
$p_{c,max}$	0.01	1	max capillary pressure in the mine-run salt [MPa]

7.2 Uncertainty Quantification Results

Figures 63, 64 and 65 present the results of the Morris method plotting the standard deviation of the elementary effects (S_i) versus the mean of the absolute values of the elementary effects (μ_i^*) for various model outputs. The standard error of the mean of the elementary effects is estimated as $SEM_i = S_i/\sqrt{r}$, where r is the number of elementary effects obtained (3 in this case). The lines in figures represent $\mu_i^* = 2\ SEM_i$. If a parameter plots below this line (i.e. its elementary effects have relatively low standard deviation), it is generally assumed that the elementary effects are significantly different than zero. Larger mean values are taken to indicate greater importance for the parameter. Larger standard deviations

indicate curvature in the sensitivity and/or interaction with other parameters. Tables 7, 8 and 9 summarize these conclusions for Figures 63, 64 and 65, respectively. It is important to note that these sensitivities are relative the parameter ranges selected.

Figure 63 presents the Morris method results for the maximum temperature at 300 days for various zones as the model output. The plot titled 'Total' uses the maximum temperature throughout the model domain, which will likely be within the waste. The change in the magnitude of the elementary effects for the various zones is apparent by inspecting the range of the x-axis in the plots. As expected, 'Total' has the highest magnitude, followed by 'Mine-Run Salt', while 'Intact Salt' is the smallest. Enthalpy, E, is found to dominate sensitivities for all zones; however, sensitivity curvature and/or interaction is indicated by the high standard deviation for the 'Air' zone. Also showing significant importance for the 'Air' zone are $k_{t,air}$ and h_{mr}, but these also have sensitivity curvature and/or interaction. These results indicate that, as expected, the enthalpy will be the most important parameter for the maximum temperature, but that the air temperature will also be influenced by its effective thermal conductivity (an uncertain parameter currently incorporating effects of convective and radiative heat transfer) and the depth of the mine-run salt. These results are summarized in Table 7.

Total	Mine-Run Salt	Air	DRZ	Intact Salt	
E	E	E	E	E	
f_{mri}	f_{mri}	h_{mr}	h_{mr}	h_{mr}	
h_{mr}	VWC_{mri}	$k_{t,air}$	VWC_{mri}	VWC_{mri}	
VWC_{mri}	h_{mr}	VWC_{mri}	$k_{t,air}$	$k_{t,air}$	
$k_{t,air}$	$k_{t,air}$	f_{drz}	f_{mri}	f_{mri}	
f_{drz}	f_{drz}	f_{mri}	f_{drz}	$k_{h,is}$	
f_{is}	f_{is}	$k_{h,is}$	$k_{h,is}$	f_{is}	
$p_{c,max}$	$p_{c,max}$	f_{is}	f_{is}	f_{drz}	
$k_{h,is}$	$k_{h,is}$	$p_{c,max}$	$p_{c,max}$	$p_{c,max}$	

Sensitivity →→→

Table 7: Parameter sensitivities to the maximum temperature in different zones.

Note: Yellow and red indicate important parameters while red also indicates sensitivity curvature and/or interaction. Sensitivity increases from the bottom row to the top row.

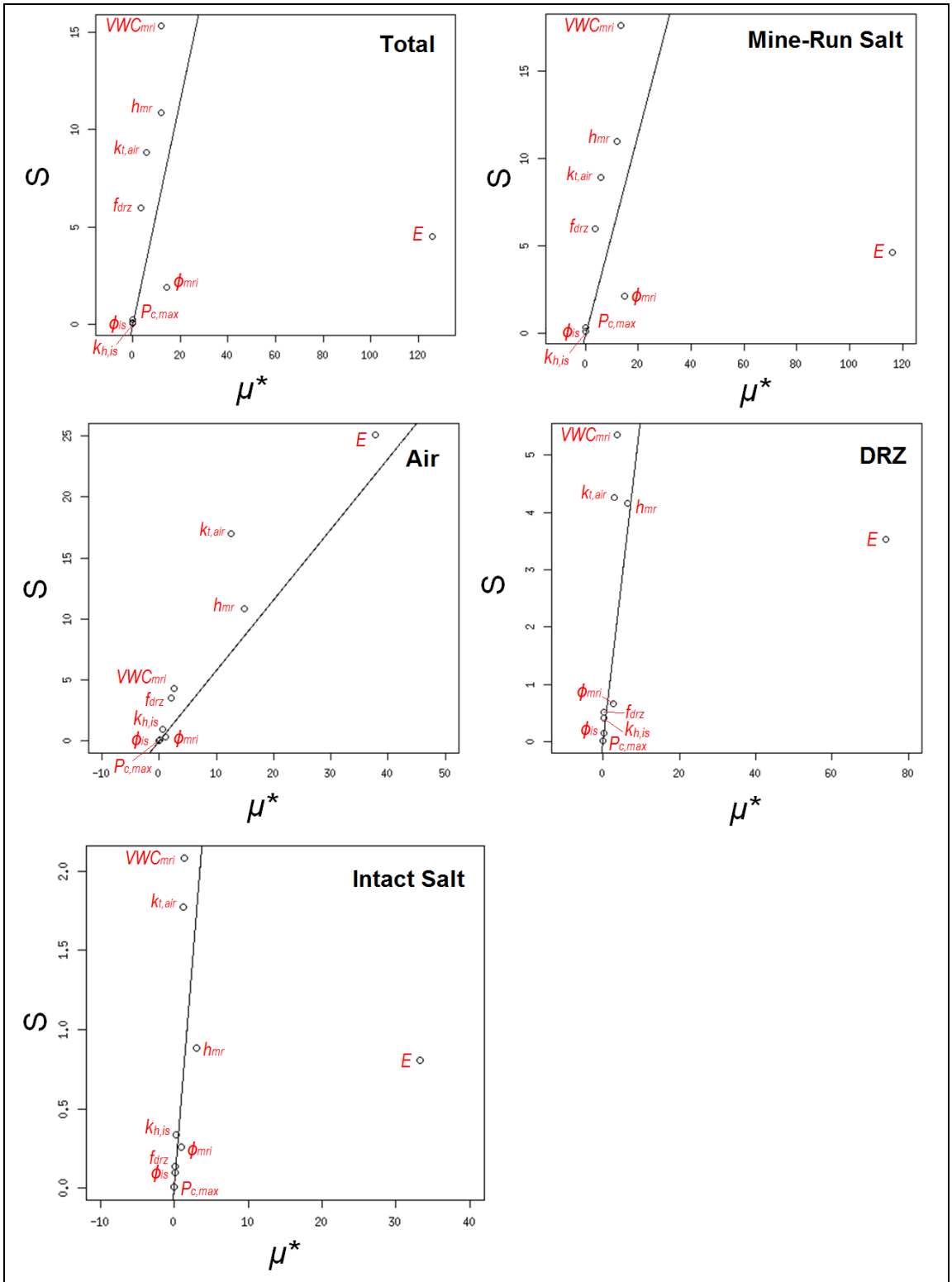

Figure 63: Morris method results using maximum temperature at 300 days as the performance metric. Plot titles indicate model zone. The vertical line is $\mu_i^* = 2\ SEM_i$

Figure 64 uses the relative change in the water mass within zones as the model output, defined as $RC_{Mw} = (M_{w,f} - M_{w,i})/M_{w,i}$, where M_w is the mass of water and subscripts f and i indicate final (300 days) and initial (14 days; start of heating), respectively. The intact salt zone had very small values of RC_{Mw}, and is omitted here. From the plots in the figure, it is apparent that all parameters have sensitivity curvature and/or interactions with other parameters (large S_i). It is interesting to note that for the 'Mine-Run Salt' and 'Air' zones, the most important parameter is the height of the mine-run salt (h_{mr}), while for 'DRZ', it is the hydraulic conductivity of the intact salt ($k_{h,is}$), followed by the porosity of the intact salt (f_{is}). These results indicate that relative water content changes in the mine-run salt and air are highly influenced by salt pile depth and that accurate intact salt properties will improve our modeling of overall water content changes in the DRZ. These results are summarized in Table 8.

Mine-Run Salt	Air	DRZ	
h_{mr}	h_{mr}	$k_{h,is}$	
VWC_{mri}	$p_{c,max}$	f_{is}	
f_{drz}	VWC_{mri}	$p_{c,max}$	
f_{is}	$k_{h,is}$	f_{drz}	
$k_{h,is}$	f_{is}	h_{mr}	
$k_{t,air}$	$k_{t,air}$	E	
E	f_{mri}	VWC_{mri}	
$p_{c,max}$	E	f_{mri}	
f_{mri}	f_{drz}	$k_{t,air}$	

Sensitivity→→→

Table 8: Parameter sensitivities to the relative change in water mass in different zones.

Note: Yellow and red indicate important parameters while red also indicates sensitivity curvature and/or interaction. Sensitivity increases from the bottom row to the top row.

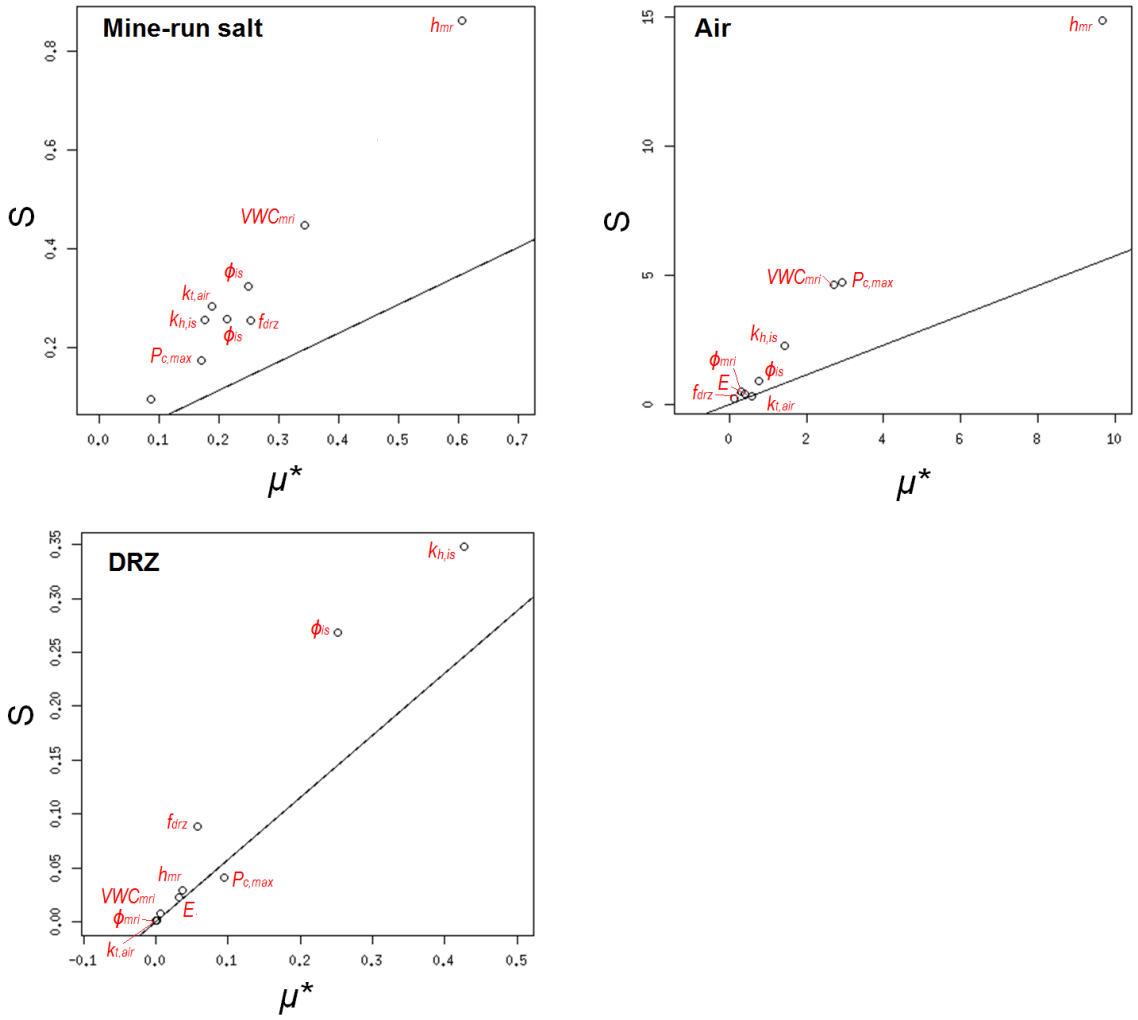

Figure 64: Morris method results using the relative change in water mass within a zone at 300 days as the performance metric. Plot titles indicate zone. The vertical line is $\mu_i^* = 2\,SEM_i$.

Figure 65 uses the summation of the absolute change in water mass for nodes in a zone as the model output. This captures not only the total change in water mass within a zone, but also the amount of redistribution of water within that zone. 'Mine-Run Salt' and 'DRZ' were the only zones to have significant absolute changes in water mass. 'DRZ' has much larger elementary effects than 'Mine-Run Salt'. The important parameters differ between 'Mine-Run Salt' and 'DRZ'. For 'Mine-Run Salt', h_{mr} and VWC_{mri} indicate importance; however, this is likely mostly an artifact of the increase in total water mass available in mine-run salt as the salt pile depth (h_{mr}) and initial volumetric water content (VWC_{mri}) increase. This leaves E as the dominant parameter for 'Mine-Run Salt', but with sensitivity curvature and/or interaction (large S_i). For 'DRZ', f_{drz} is the most important, followed by $k_{h,is}$ and f_{is}, with

significant sensitivity curvature and/or interaction for all these parameters. As in Figure 64, this indicates that understanding the surrounding intact salt properties and the degree of damage to the DRZ, and how that affects DRZ permeability and porosity, is critical to improving our modeling of water movement within the DRZ. These results are summarized in Table 9.

Mine-Run Salt	DRZ
h_{mr}	f_{drz}
VWC_{mri}	$k_{h,is}$
E	ϕ_{is}
f_{mri}	$p_{c,max}$
f_{drz}	h_{mr}
f_{is}	E
$k_{h,is}$	VWC_{mri}
$k_{t,air}$	$k_{t,air}$
$p_{c,max}$	f_{mri}

Sensitivity→→→

Table 9: Parameter sensitivities to the relative change in water mass in different zones.

Note: Yellow and red indicate important parameters while red also indicates sensitivity curvature and/or interaction. Sensitivity increases from the bottom row to the top row.

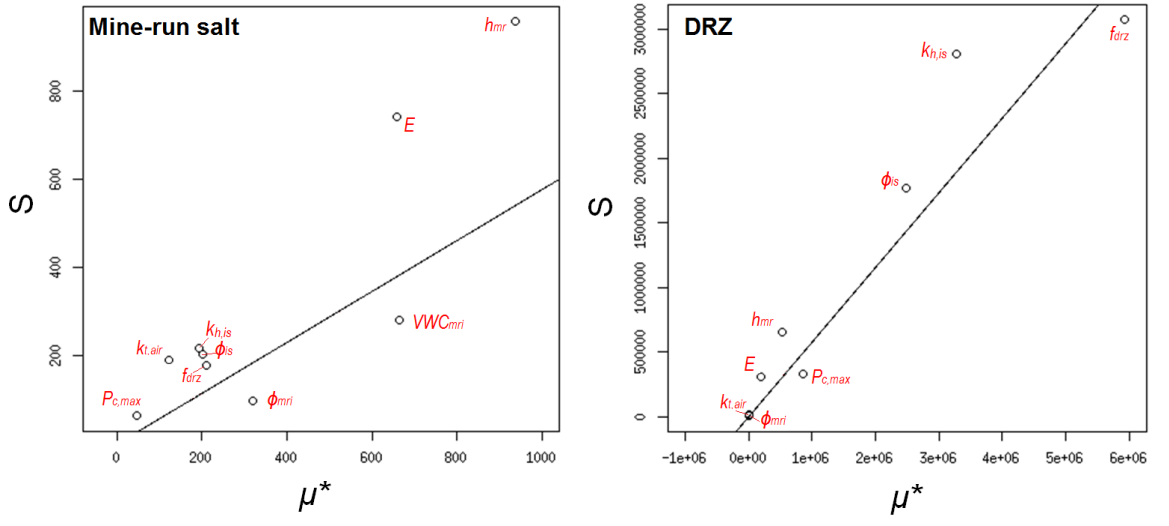

Figure 65: Morris method results using the summation of the absolute change in water mass within the nodes of a zone at 300 days as the performance metric. Plot titles indicate zone. The vertical line is $\mu_i^* = 2\ SEM_i$.

In summary, this analysis indicates that:

1. The heat load of the canisters (E) overwhelmingly dominates all other parameters with regard to the maximum temperature in all zones except for the air gap.

2. Experimental studies on the conductive, convective and radiative heat transfer across the air gap are needed to determine an accurate effective thermal conductivity for the air in order to model air temperatures accurately.
3. The depth of mine-run salt has an important effect on air temperature, decreasing the temperature as the depth increases.
4. Intact salt properties are important for modeling water mass changes and redistribution in the DRZ.
5. Understanding how excavation changes the permeability and porosity of the DRZ are important for modeling water redistribution in the DRZ.

8. Pore-Scale Simulation of Brine Behavior under Thermal Gradients

This chapter presents a model for the pore-scale simulation of brine transport within aggregates of salt crystals with no mineral impurities. The pore-scale model is based on the lattice Boltzmann method and combines the single-component multiphase model, the mass transport model, and the dissolution/precipitation model previously developed at LANL. Additional schemes are also developed to handle reactive and moving boundaries with complex geometries, to account for liquid/vapor phase transition, and to guarantee mass and momentum conservation. The pore-scale model is shown to capture coupled non-linear multiple physicochemical processes including multiphase flow with phase separation, heat transfer, mass transport, chemical reaction, dissolution/precipitation, and dynamic evolution of the pore geometries. After confirming the numerical implementation by comparing to other solutions of several multiphase flow and reactive transport problems, the model is used to study the behavior of a brine inclusion in a single salt crystal. Multiphase reactive transport phenomena with phase transition between liquid-vapor phases and dissolution/precipitation of the salt in the brine inclusion are simulated, and effects of initial inclusion size and temperature gradient on the brine behavior are investigated. Many experimental observations are reproduced.

8.1 INTRODUCTION

Because thermally driven migration of brine will influence the evolution of the engineered system, including the waste canisters and waste form, or could impact the mechanical behavior of the salt medium (Robinson et al., 2012), models of the brine migration process are needed to inform the safety case for disposal of heat-generating nuclear wastes in salt. For the water phase residing as fluid inclusions within salt grains, the migration and liberation of water will be governed by several coupled physicochemical processes taking place, including multiphase fluid flow with phase transition, heat transfer, mass transport, heterogeneous reactions, dissolution and precipitation, and dynamic evolution of the pore geometry. Because these processes are ultimately governed by pore-scale interfacial phenomena, the pore-scale simulation can provide a full accounting of all of the important physical/chemical processes, enabling a far more realistic treatment of the fluid migration process. Moreover, pore-scale simulation can identify key parameters and physicochemical processes by enabling a systematic study of the effect of various factors on the behavior of brine inclusion; can help interpret experimental results and guide the design of new experiments; and can provide constitutive relationships for engineering-scale simulations, such as effective diffusivity, permeability-porosity, relative permeability, effective surface area, etc.

The challenges of pore-scale simulation of such a complex problem are to accurately model the coexistence of three phases (gas, liquid, and solid phases), to predict dynamic evolution of phase interfaces (liquid-gas interfaces due to phase transition and liquid-solid interfaces due to dissolution/precipitation), and to consider the complex interplay between the multiple processes. In addition, brine inclusion inside the salt crystal is a closed system, which requires careful treatment to ensure strict mass and momentum conservation.

The model developed in this project combines the single-component multiphase Shan-Chen model (Shan and Chen, 1993; Shan and Chen, 1994), a lattice Boltzmann (LB) mass transport model (Sullivan et al., 2005; Chen et al., 2012), and a dissolution and precipitation model (Kang et al., 2002; Kang et al., 2004). To guarantee mass and momentum conservation in a closed system, schemes are developed for handling flow and transport information associated with computational nodes undergoing liquid/vapor and liquid/solid phase changes. A new general LB concentration boundary condition is developed which can handle various concentration boundaries including complex moving and reactive boundaries. After the physicochemical model is described, the single-component multiphase Shan-Chen model is presented, along with the mass transport LB model, and the dissolution and precipitation model. Then, after validating models by comparison to standard solutions, simulation results are presented on thermal migration of a brine inclusion in a salt crystal, and avenues for future work are described.

8.2 PHYSICOCHEMCIAL MODEL

When a heat-generating nuclear waste is disposed in salt, the salt in the vicinity of the waste will heat up, and a temperature gradient will be established between the waste and the salt nearby. This modeling effort aims at the thermal gradient migration of a brine inclusion in a single crystal of salt under these circumstances. The physicochemical problem is schematically shown in Figure 66 and can be generally described as follows. A solid matrix (the single crystal of salt) contains an intra-granular inclusion of brine in chemical equilibrium with the solid salt. Then the solid matrix is subjected to a temperature gradient. The salt solubility increases with increasing temperature. Therefore, the salt dissolves on the hot side of the inclusion, the dissolved salt transports through the fluid to the cold side, and precipitates there. The net effect of this dissolution/precipitation is the microscopic dynamic evolution of the geometries of the inclusion, and the macroscopic migration of the inclusion toward the higher temperatures. During the migration process, the total volume of the inclusion may change due to unequal amounts of dissolution and precipitation. If the volume of the inclusion increases due to

dissolution outpacing precipitation, the brine in the closed inclusion may separate into a vapor phase and a liquid phase, leading to two-phase flow in the inclusion.

The multiple coupled non-linear physicochemical processes pose great challenges to numerical simulations, especially those based on solving partial differential governing equations using finite element, finite difference, or final volume techniques. Alternatively, the LBM is more promising for solving such coupled non-linear physicochemical problems at the pore-scale because of its ability to account for complex structures and all relevant physicochemical processes.

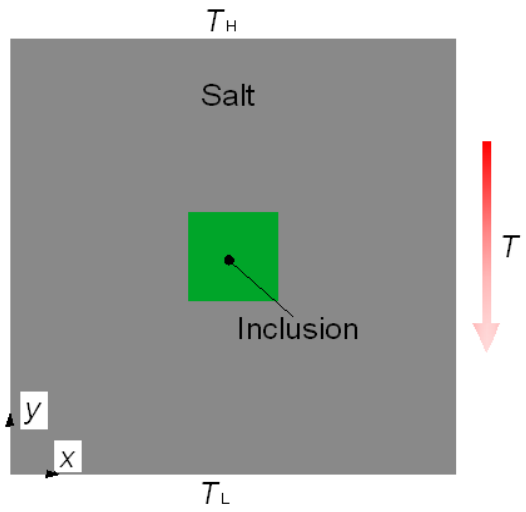

Figure 66: Schematic of thermal migration of a brined inclusion in a salt crystal

8.3 NUMERICAL MODEL

8.3.1 Lattice Boltzmann Model for Multiphase Flow and Solute Transport

In the LB method, the motion of fluid is described by a set of particle distribution functions. Based on the simple and popular Bhatnagar-Gross-Krook (BGK) collision operator (Bhatnagar et al., 1954), the evolution of the density distribution function is written as

$$f_i(\mathbf{x}+c\mathbf{e}_i\Delta t, t+\Delta t) - f_i(\mathbf{x},t) = -\frac{1}{\tau_v}(f_i(\mathbf{x},t) - f_i^{eq}(\mathbf{x},t)) \tag{28}$$

where $f_i(x,t)$ is the density distribution function at the lattice site $\mathbf{x}$ and time t, f_i^{eq} is the equilibrium distribution function, $c=\Delta x/\Delta t$ is the lattice speed with Δx and Δt as the lattice spacing and time step, respectively, and τ_v is the dimensionless relaxation time. The discrete velocities $\mathbf{e}_i$ depend on the

particular velocity model. With a proper choice of $\mathbf{e}_i$ and f_i^{eq}, Equation 28 can recover the Navier-Stokes equation for fluid flow with the fluid density ρ and velocity $\mathbf{u}$ given by the first and second moments of the particle distribution functions

$$\rho = \sum_i f_i \quad \rho\mathbf{u} = \sum_i f_i \mathbf{e}_i \tag{29}$$

and the fluid viscosity is related to the relaxation time by

$$\upsilon = c_s^2(\tau_\upsilon - 0.5)\Delta t \tag{30}$$

where c_s is the lattice sound speed.

For a fluid system with multiple fluid phases, multiple sets of distribution functions can be introduced, each representing a fluid phase. The segregation of a fluid system into different fluid phases can be realized through an interaction force between distribution functions of different fluids. In addition, different equations of state (EOS) can be obtained by changing the form of the fluid-fluid interaction (Yuan and Schaefer, 2006). Similarly, wettability can be incorporated through fluid-solid interaction.

For a fluid system with multiple dissolved species, additional sets of distribution functions can be introduced to describe the transport of the solute species. Again, with a proper choice of discrete velocities and equilibrium distributions, the evolution equation of these distributions can recover the advection-diffusion equation describing the transport of solute species, with the concentration given by the first moment of the distribution functions and diffusion coefficient related to the relaxation time.

The temperature field can be solved in a similar fashion as the concentration field. In this study, because of the small size of the brine inclusion compared to the salt grain, we assume that the existence of the brine does not affect the temperature field in the salt grain, which has a linear distribution from the top (hot) to bottom (cool).

8.3.2 Heterogeneous Reaction at the Solid-Liquid Interface

Since the solute exists only in the liquid phase, dissolution and precipitation only occur at the liquid-solid salt interface at which the following heterogeneous chemical reaction takes place

$$S_{\mathrm{aq}} \Leftrightarrow S_{\mathrm{S}} \tag{31}$$

where S_{aq} and S_{s} represent the aqueous phase (solute) and solid phase of the salt, respectively. Obviously, local super-saturated conditions result in precipitation, and local under-saturated conditions lead to dissolution. The boundary condition at the liquid-solid interface for the aqueous phase is represented by

$$D\frac{\partial C_{\mathrm{aq}}}{\partial \mathbf{n}} = -k(1 - KC_{\mathrm{aq}}) \tag{32}$$

where k is the reaction rate constant and C_{aq} is the salt concentration. The term **n** represents the surface normal which points into the fluid. K is the equilibrium constant, with a higher value corresponding to a lower salt solubility. K decreases with the temperature.

8.3.3 VOP for dissolution and precipitation

In the VOP (volume of pixel) method (Kang et al., 2006), the entire domain is divided to pixels (or computational nodes). Each pixel is assigned a value representing the volume of the solid phase. At each time step, at the reactive solid-fluid interfaces, the volume of a solid node V_{s} with initial value of V_0 is updated by

$$\frac{\partial V_{\mathrm{s}}}{\partial t} = -AV_{\mathrm{m}}k(1 - KC_{\mathrm{aq}}) \tag{33}$$

where A is the reaction area, and V_{m} is the molar volume. Thus, V_{s} is updated at each time step by

$$V_{\mathrm{s}}(t + \Delta t) = V_{\mathrm{s}}(t) - V_{\mathrm{m}}k(1 - KC_{\mathrm{aq}})\Delta tA \tag{34}$$

If V_{s} reaches zero, the dissolution is complete, and the solid node is removed and is converted to a fluid node; meanwhile, the fluid flow and mass information in this new fluid node must be initialized. On the other hand, when the volume of a solid node exceeds a certain threshold value, for example, if it doubles, precipitation takes place and one of the nearest neighboring fluid nodes becomes a solid node. At the same time the volume of the original solid node is set back to V_0 and the initial volume of the new solid node is assigned as V_0. Because there may be several fluid nodes around the original solid node, several rules have been proposed by Kang et al. (2006) to determine which fluid node is chosen for the precipitation. In the present study, this node is simply randomly determined.

8.3.4 A New General Concentration Boundary Condition

For solute transport in the liquid phase, the solid-liquid interfaces are reactive boundaries and the liquid-vapor interfaces are moving boundaries. To handle these interfaces which are often complex, a unified LB concentration boundary condition is required that can handle moving and reactive boundaries. Several concentration boundary conditions have been developed for different boundary condition types in the literature: for a recent review, the reader is referred to Huag et al. (2011) and Zhang et al. (2012). There have also been a few studies treating reactive boundaries (Kang et al., 2002; Zhang et al., 2012; Kang et al., 2007; Walsh and Saar, 2010). To discuss the concentration boundary conditions, a schematic

illustration of the fluid-solid interface is presented in Figure 67. Following Zhang et al. (2012), the boundary condition at this interface is

$$b_1 \frac{\partial C}{\partial \mathbf{n}} + b_2 C = b_3 \tag{35}$$

which is a general formula that can describe all the three types of boundary conditions: the Dirichlet, the Neumann, and a mixed boundary condition.

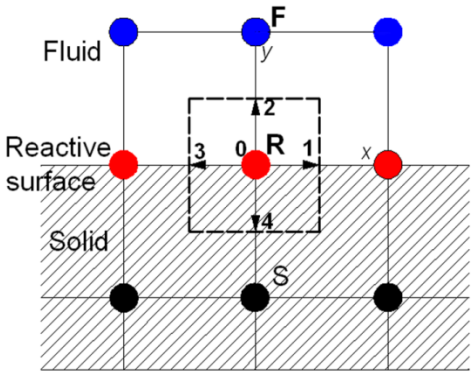

Figure 67: A schematic illustration of a fluid-solid interface node R. F is fluid node and S is solid node.

Kang et al. (2007) derived a correct expression of the concentration distribution function in terms of the corresponding concentration and its gradient

$$\sum g_i \mathbf{e}_i = C\mathbf{u} - D\nabla C \tag{36}$$

In Fig. 2, after each streaming step, g_2 is unknown and g_4 is known; and g_1 and g_3 do not affect the fluid domain and hence are not needed to calculate their values.

Zhang et al. (2012) proposed a so-called general bounce-back scheme for concentration boundary conditions, where they solved Equation 35 directly to obtain the concentration at the boundary using the following difference scheme

$$\frac{\partial C}{\partial n} = \frac{C_R - C_F}{|\Delta \mathbf{x}|} \tag{37}$$

where C_R and C_F are the concentrations at interface node R and adjacent fluid node F, respectively, and $\Delta\mathbf{x}$ is the vector connecting nodes F and R. Thus

$$b_1 \frac{C_R - C_F}{|\Delta \mathbf{x}|} + b_2 C = b_3 \tag{38}$$

C_R is the only unknown variable in Equation 38 and thus can be directly solved.

In this study, we use Equation 39 to solve the unknown distribution function after C_R is obtained from Equation 38. For the boundary node shown in Figure 67, the new boundary condition can be written as

$$\begin{cases} b_1 \dfrac{C_R - C_F}{c} + b_2 C = b_3 & (a) \\ g_2 - g_4 = C_R v - \dfrac{D}{c}\dfrac{\partial C}{\partial y} & (b) \end{cases} \tag{39}$$

Equation 39a is used to solve C_R, after which Equation 39b is used to solve g_2. In this way, this new boundary condition treatment can handle both static and moving, both reactive and nonreactive boundaries. For a static liquid-solid boundary, a precipitation or dissolution reaction described by Equation 32 leads to the following reduced form of Equation 39:

$$\begin{cases} D\dfrac{C_R - C_F}{c} = -k(1 - KC_R) & (a) \\ g_2 - g_4 = -\dfrac{D}{c}\dfrac{\partial C}{\partial y} & (b) \end{cases} \tag{40}$$

On the other hand, for the moving liquid-vapor boundary, there is no reaction, and the concentration gradient of solute is zero. Thus Equation 39 reduces to

$$\begin{cases} D\dfrac{C_R - C_F}{c} = 0 & (a) \\ g_2 - g_4 = C_R v & (b) \end{cases} \tag{41}$$

8.3.5 Numerical procedure

As introduced above, the physiochemical problem under consideration includes multiple processes such as single-component multiphase flow of liquid water and vapor, mass transport of salt in the aqueous phase with heterogeneous reaction at the liquid-solid interface, and dissolution and precipitation of the solid salt. After initialization, each iteration involves the following sub-steps: (1) updating the fluid field using the single-component multiphase Shan-Chen LB model, (2) solving the solute (namely the concentration of salt in the aqueous phase) transport in the liquid water with the heterogeneous reaction at the liquid-solid interface using the LB mass transport model, and (3) updating the density of solid salt nodes and updating the geometry of the solid phase using the dissolution and precipitation model. For the systems considered here, the evolution of the solid geometry due to dissolution or precipitation is very slow compared to fluid flow or solute transport. Thus at each configuration of the solid phase, the steady state of the fluid flow and mass transport can be obtained.

8.4 VALIDATION

Our numerical model is constructed incrementally by combining different models including the multiphase flow Shan-Chen model (Chen et al., 2012; Kang et al., 2005), mass transport with homogeneous and heterogeneous reactions (Kang et al., 2007; Chen et al., 2012) and dissolution and precipitation including nucleation and crystal growth (Kang et al., 2004; Chen et al., 2012). Since no analytical solutions or experimental results of these complex coupled non-linear multiple physicochemical processes is available for performing quantitative comparisons with our simulation results, our validation consists of testing each of the sub-models, each of which has appropriate theoretical results with which to compare to our pore-scale model.

8.4.1 Single-Component Two-Phase Flow

Several physical problems are selected for validation of the single-component multiphase Shan-Chen model, including the first order phase separation, coexistence curve of a circular static liquid droplet embedded in a vapor phase, and equilibrium contact angle for a liquid droplet on a flat and uniform solid wall. Here we present simulations of the circular static liquid droplet embedded in the vapor phase in a gravity-free field. We simulate this problem using a 201×201 lattice periodic system. In the simulation, a liquid droplet with initial radius r_0 is placed at the center of the domain. The density field is initialized using the method in Huang et al. (2011).

The LB simulated coexistence curves are in good agreement with the theoretical one as shown in Figure 68a. Besides, to calibrate the Laplace law, a series of simulations are conducted by changing r_0. Figure 68b plots Δp as a function of $1/r$, where the linear relationship can be clearly observed, indicating the Laplace law is well satisfied.

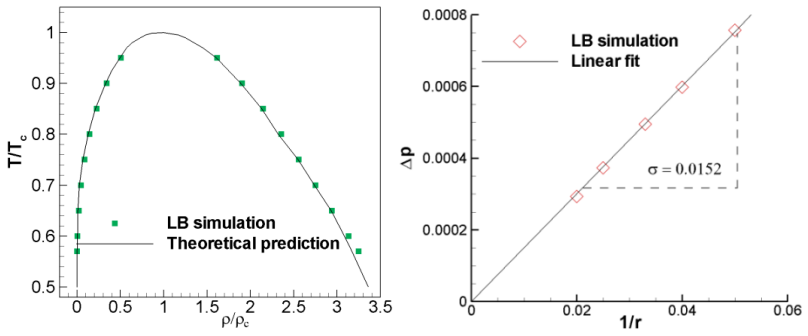

Figure 68: Simulation results of circular static liquid droplet embedded in vapor phase in a gravity-free field using a 201×201 lattices periodic system. (a) comparison of coexistence curve obtained from LB simulations with theoretical one predicted by Maxwell equal-area construction; (b) calibration of the Laplace law.

8.4.2 Mass Transport

Two reactive transport problems with analytical solutions are adopted to validate our mass transport LB model and the new concentration boundary condition. The first reactive transport problem for validation is species diffusion in a channel with surface reaction (Kang et al., 2007). Excellent agreement is obtained between simulation results and the analytical solutions.

The second reactive transport problem for validation is diffusion in a channel with bulk reaction (Chen et al., 2012). Species A enters a channel with size $a \times b$ from the left inlet with concentration C_{in} = 1 and leaves the channel at the right outlet with concentration C_{out} = 0. The solvent flows with a uniform constant horizontal velocity u and the transport of species A does not affect the flow field. The bulk reaction of A takes place in the entire domain with a bulk reaction rate constant k (s^{-1}). Thus, the left and right walls are moving boundaries with known concentration. Figure 69 shows the simulation results for different values of Pe (Pe = ub/D, representing the relative strength of convection to diffusion) and different k. The computational domain is discretized by 101 × 61 lattices. It can be seen from Figure 69a that the simulation results of the steady state profile of C along the x axis compare well with the analytical solutions for different Pe with k = 0. From Figure 69b the simulation results compare well with the analytical solutions for different reaction rate constants k, for the case of Pe =3.

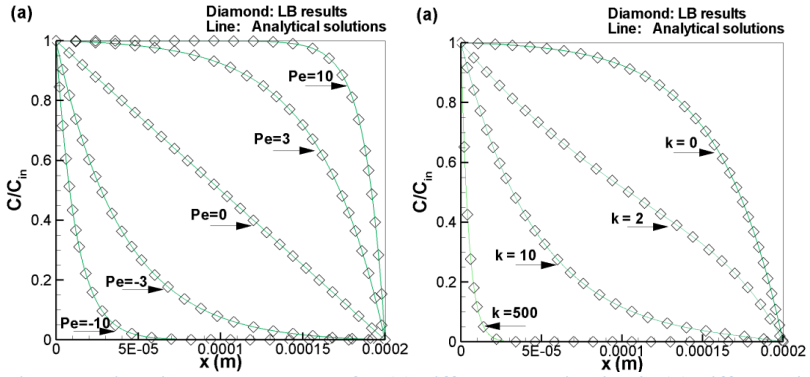

Figure 69: Concentration in the x direction at steady state for (a) different Pe with k = 0; (b) different k for Pe = 3.

8.5 RESULTS AND DISCUSSION

8.5.1 Thermal Migration of the Inclusion

In this section, we apply our numerical model to the study of thermal migration of a brine inclusion in a single salt crystal. The computational domain is shown in Figure 66, which is a salt crystal containing a brine inclusion at the center. The sizes of the salt crystal and the inclusion are $L \times H$ = 1 ×

1cm and $A \times B = 0.2 \times 0.2$ cm, respectively. The system is discretized by 202 × 202 lattices. Initially, the system is set at a uniform temperature $T_0 = 0.7T_c$ and the inclusion is filled with liquid brine with density ρ_l=0.3572 (the liquid density at $T_0 = 0.7T_c$). Then, the salt crystal is subjected to a temperature gradient with $T_H = 10 + T_0$ at y =1 cm and $T_L = -10 + T_0$ at y = 0 cm. The analytical temperature distribution is linear, with $T = T_L + (T_H - T_L)\, y/H$, which is symmetrical about y = H/2, where $T = T_0$. The kinetic viscosity is $\upsilon = 1 \times 10^{-6}$ m^2 s^{-1} with corresponding relaxation time τ = 1.0; and the diffusion coefficient of salt in water is $D = 9 \times 10^{-8}$ m^2 s^{-1}. Other parameters for simulations are $V_m = 0.625 \times 10^{-12}$ m^3 mol^{-1}, $k = 9 \times 10^{-5}$ m^3 s^{-1} and gravity $\mathbf{g} = (0, -0.035)$. The contact angle between liquid water and the solid salt is about 78^o, which is relatively hydrophilic. For fluid flow, the non-slip boundary conditions are applied on all the solid-fluid interfaces. The new concentration LB boundary condition for mass transport developed in Section III.D is employed on the reactive liquid-solid boundaries and the moving liquid-vapor boundaries.

The time evolution of the shape of the inclusion as well as the density field inside the inclusion are shown in Figure 70a, and corresponding concentration of the solute is displayed in Figure 70b. Subjected to the temperature gradient, the solute concentration at the bottom of the inclusion is super-saturated, while that at the top of the inclusion it is under-saturated. Therefore, the salt precipitates at the bottom of the inclusion (cold sites) and dissolves at the top of the inclusion (hot sites) (t = 0.08 s to t = 8.3 s). Such micro-evolution of the geometry of the inclusion leads to the macro observable migration of the inclusion (t = 0.08 s to t = 83.3 s). Since the migration is towards the hot site and the solubility gradually increases, the amount of dissolution is larger than the amount of precipitation, leading to a volume increase of the inclusion during migration. This is shown in Figure 71, which plots the volume of the inclusion with time, where the volume is normalized by the initial volume of the inclusion. Because the inclusion is a closed system, volume increase leads to decreased fluid density. When the density of the fluid is reduced to a critical value, the phase separation takes place (t = 112.5 s), with the fluid partitioning into liquid and vapor phases with densities of 0.3572 and 0.00312, respectively. As shown in Figure 70, the rate of increase of inclusion volume slows down after the phase separation occurs. This is because the solute once in the entire inclusion now is concentrated into liquid phase during the short time of phase separation, leading to higher concentration of solute in the liquid phase. The higher solute concentration facilitates the precipitation while slowing down the dissolution, leading to reduced rate of the inclusion volume growth. In addition, the reactive surface area for dissolution/precipitation reactions, which only take place at liquid-solid interfaces, decreases (t = 112.5 to t =187.5 s in Figures 70a and 70b). From the set of images in Figure 70 it can be seen that there are a large number of extremely small inclusions left behind in the wake of the inclusion. This is due to the randomness of the precipitation

process. Finally, it is worth mentioning that during the entire process the fluid flow in the closed system is extremely slow, which leads to the dominance of diffusion over advection for mass transport in the inclusion. The concentration profiles in Figure 70 are consistent with this interpretation.

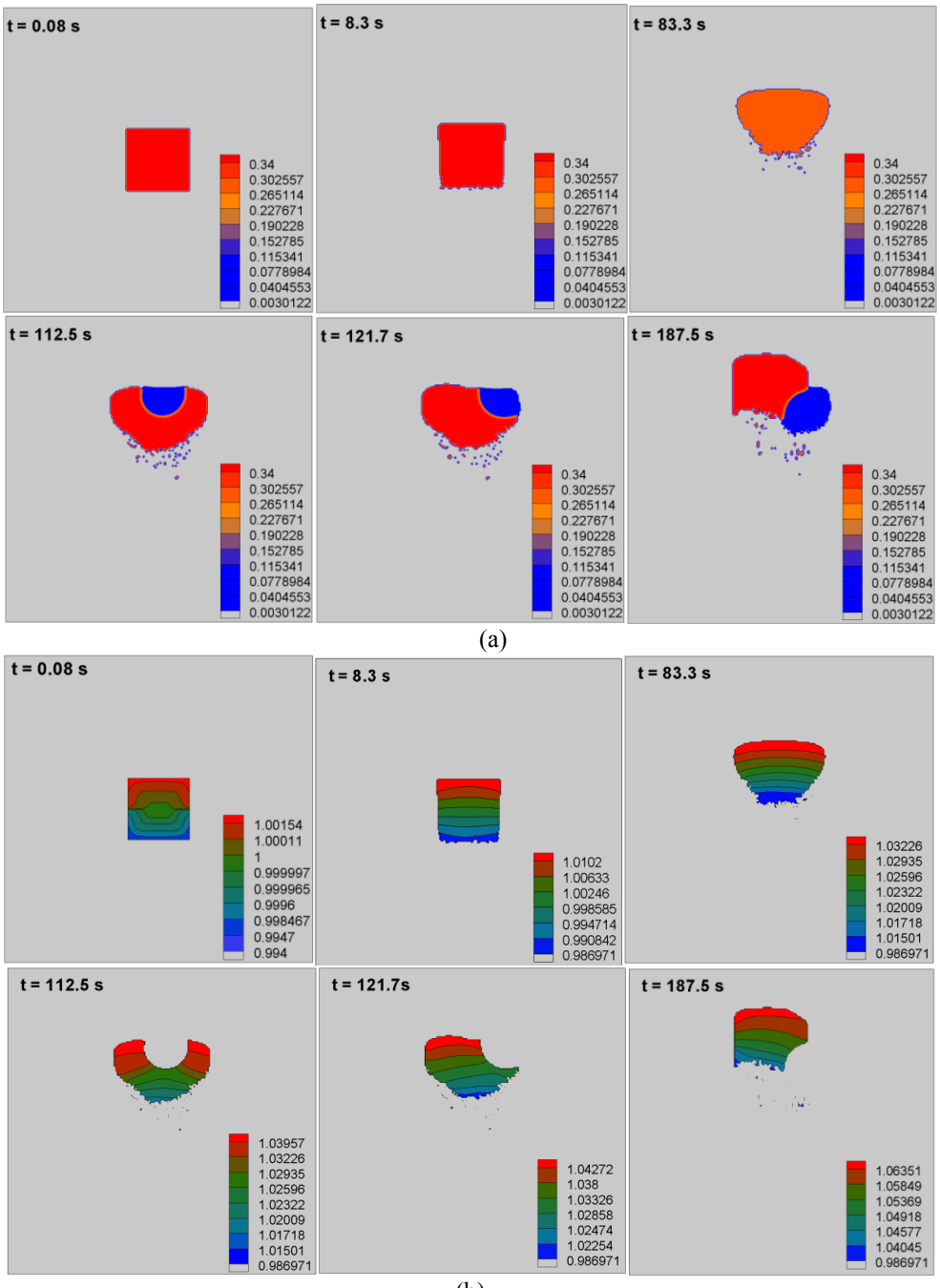

Figure 70: Simulation results of the thermal migration of the inclusion in the salt crystal. (a) time evolution of the density field in the inclusion, (b) time evolution of the aqueous salt concentration.

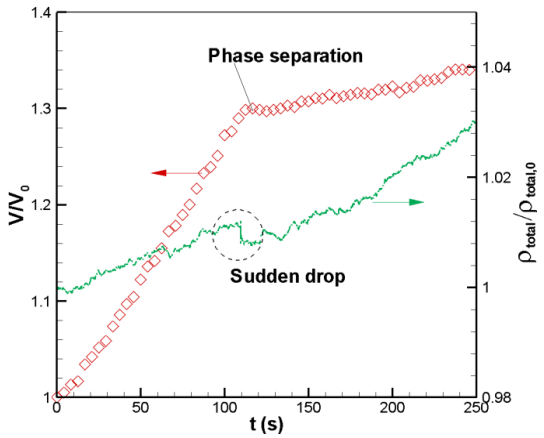

Figure 71: Variation of inclusion volume and total density of fluid with time. The volume is normalized by the initial volume of the inclusion.

Figure 71 also shows the variation of total fluid density in the inclusion with time. The mass conservation constraint is well satisfied, with maximum relative variation of the density of 3.02% in 250 s, indicating that our scheme of handling information associated with nodes undergoing phase change is reliable. Note that there is sudden drop of the total density when phase separation of liquid-vapor phases occurs, as shown in Figure 70. This is because the current Shan-Chen model and the force scheme employed in the present study introduces an unphysical source term into the mass conservation equation, as reported in Kang et al. (2006) and Li et al., (2012) . Since the source term is the time derivative of the forces, it is relatively large when phase separation takes place, which generates forces between liquid and vapor phases in a very short time, thus resulting in the sudden drop of total density. Overall, the macro thermal migration of the inclusion as well as the microscopic complex coupled multiple physicochemical processes including multiphase flow with phase separation, mass transport, surface reaction, and dissolution/precipitation are well captured by our pore-scale model.

8.5.2 Effects of Initial Inclusion Size and Temperature Gradient

We now present parameter sensitivity studies examining the effects of initial inclusion size and the temperature gradient on the thermal migration processes. To simplify the discussion, we ignore the phase separation and assume that only liquid phase exists during the entire migration process. Since the migration of the brine inclusion is very slow and the fluid flow inside the inclusion is inconsequential, this analysis considers only the mass transport and dissolution/precipitation sub-processes. Figure 72a shows the relationship between inclusion volume and time for different initial inclusion size, for simulations in which the inclusion travels from the starting point to the top boundary of the salt crystal. Figure 72b shows the inclusion geometries and positions for different initial inclusion size at t =249.8 s. In the simulations, all the parameters are the same as that in the above section, except the initial inclusion

size. Figure 72a shows that the volume increase depends strongly on the inclusion size, such that the larger inclusions exhibit smaller relative volume increases. For example, for the inclusion with initial size of 0.5 mm, the ratio between the final volume and initial volume is nearly 5, while for the inclusion with initial size of 2 mm, the corresponding ratio is only about 1.7. This is due to more efficient and quicker mass transport from hot sites to cold sites for smaller inclusions. In addition, the macro migration velocity is larger for larger inclusions, as shown in Figure 72b. For example, the time required for the inclusion to reach the top boundary of the salt crystal is about 250 s for the 2mm inclusion, while for the 0.5 mm inclusion size, the travel time is almost 400 s. However, in the limit of very small inclusions, such as those with size of 0.15 mm, the volume variation is small (the oscillation in Figure 72a is due to the small initial inclusion size and model discretization issues in which one lattice of dissolution or precipitation leads to large V/V_0) and migration is extremely slow. This is because the concentration difference required for dissolution and precipitation cannot be established in such a narrow space due to the tiny temperature difference across that space. Therefore, there is rare dissolution and precipitation and thus the inclusion is almost static. Such phenomenon are consistent with the conclusion in Olander et al. (1982) that at given thermal gradient there is a critical inclusion size under which the inclusion velocity becomes very small.

Figure 73a shows the relationship between inclusion volume and time and Figure 73b shows the inclusion geometries and position at certain time for different temperature gradients. The volume variation as well as the macro migration velocity are larger for larger temperature gradients. This is expected, as the larger temperature gradient leads to larger solubility differences, and thus a greater driving force for dissolution/precipitation driven inclusion migration. Similar to the phenomenon described above of a critical inclusion size, there is a critical temperature gradient at which the inclusion velocity becomes very small. As shown in Figure 73, for ΔT of 2 K, the inclusion is almost static after some dissolution and precipitation at the initial stage.

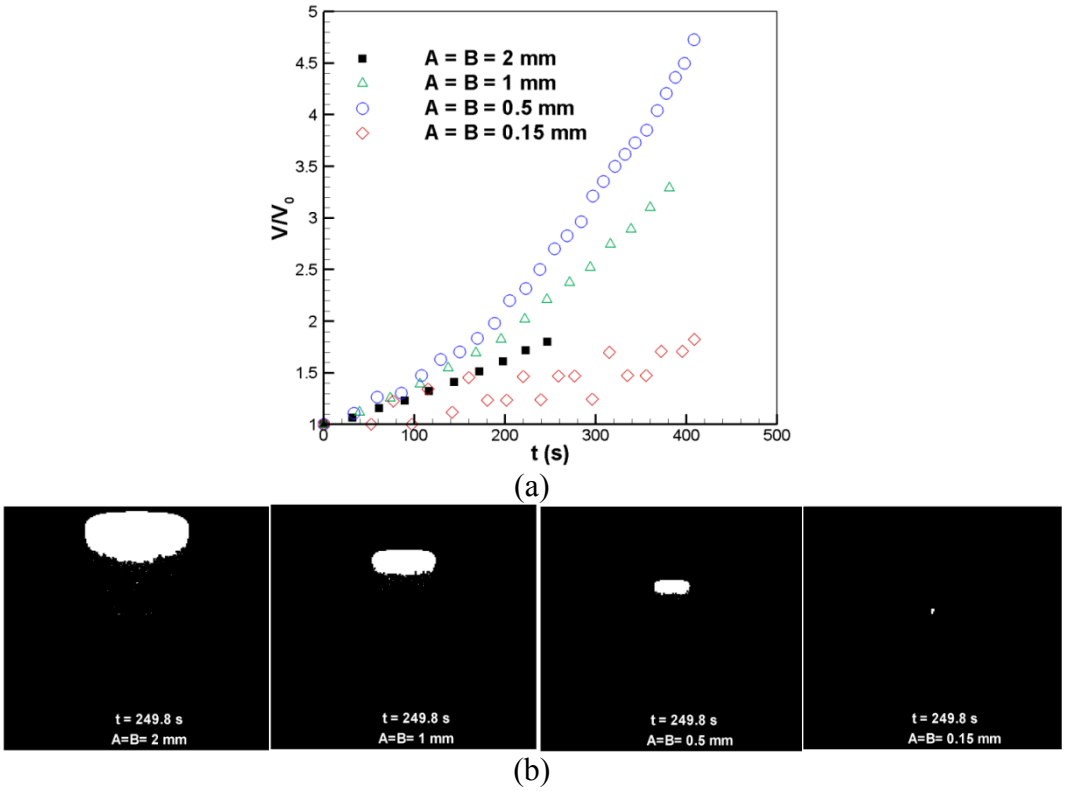

Figure 72: Effects of inclusion size on the migration process, (a) relationship between inclusion volume and time, (b) the inclusion shape and location at a given time (249.8 s).

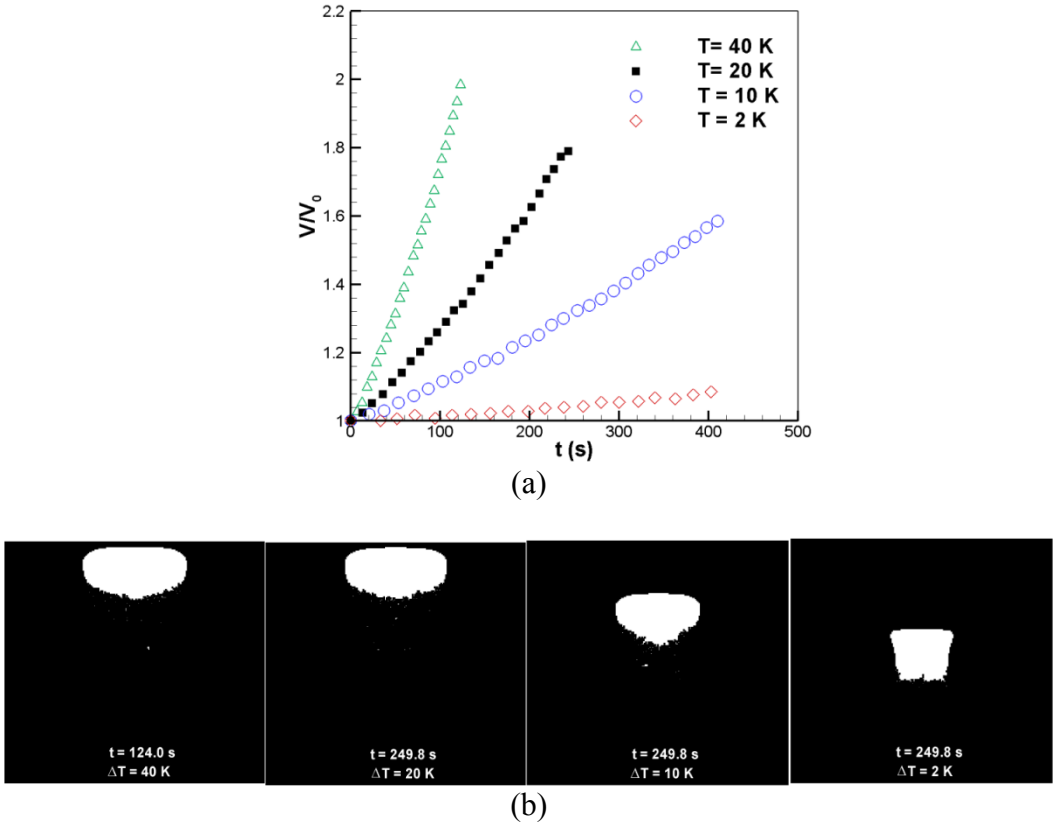

Figure 73: Effects of temperature gradient on the migration process, (a) the relationship between inclusion volume and time, (b) the inclusion shape and location at a given time (249.8 s, except for the leftmost figure, for which the inclusion reaches the boundary at 124 s).

8.5.3 Comparison with Experiments

Some of the simulation results are consistent with experimental observations, e.g., the migration of the liquid inclusion in the direction of the temperature gradient. However, distinct differences also exist. For example, the process observed in the experiments whereby the liquid inclusion travels toward the heat source, but the vapor goes in the opposite direction, is not observed in the pore-scale model. There may be several reasons for this difference. First, the temperature (gradient) influences liquid and vapor differently. As a result, an initial inclusion with a different liquid/vapor ratio may behave very differently. In the current numerical simulation, the initial inclusion was assumed to contain liquid water only, which may not be the case in the experiments. Second, because salt only dissolves into liquid water (not vapor), the salt surface in contact with the vapor is nonreactive. This blanketing of the salt surface by the vapor may play an important role in the evolution of the inclusion. In the numerical simulation, the temperature gradient is in the opposite direction of the gravity. Because the vapor bubble rises to the top of the inclusion due to buoyance, the salt surface covered by the vapor is then the hottest part of the salt-inclusion interface. In the experiments, however, the temperature gradient is perpendicular to the direction

of gravity. Third, the defect of the salt crystal, which likely exists in the experiments, but not considered in the current simulation, may change the energy barrier for salt dissolution/precipitation, and hence may play an important role in the evolution of the inclusion.

In future simulations, the conditions, including liquid/vapor ratio of the initial inclusion, the direction of temperature gradient with regard to the gravity, as well as the defect of the salt crystal, will be carefully chosen (if known from the experiments) or systematically varied to investigate their effect on the behavior of brine inclusion, and to obtain better agreement between the model and experimental results.

8.6 Summary of pore scale modeling results

In this section, a pore-scale model based on LBM is developed to investigate the coupled multiple physicochemical processes including multiphase flow with phase transition, heat transfer, mass transport, surface chemical reaction, dissolution and precipitation, and dynamic evolutions of the pore-scale geometries of the solid phase. The single-component multiphase Shan-Chen LB model (Shan and Chen, 1993; Shan and Chen, 1994) is used to simulate the liquid-vapor two-phase flow, the mass transport LB model with general form of equilibrium function (Sullivan et al., 2005) is used to account for mass transport, and the VOP method is adopted to describe dissolution and precipitation.

A new general LB concentration boundary condition is also developed. The new LB concentration boundary condition can handle concentration boundaries with the general form $b_1 \partial C / \partial \mathbf{n} + b_2 C = b_3$, and the boundaries can be moving and can have complex structures. Two reactive transport problems are employed to validate the new general LB concentration boundary condition, and the simulation results are in good agreement with the corresponding analytical solutions.

The pore-scale model is used to simulate the thermally driven migration of an inclusion in a salt crystal. The macro thermal migration of the inclusion, as well as the microscopic coupled multiple physicochemical processes (multiphase flow with phase separation, mass transport, surface reaction, and dissolution/precipitation) are well captured by our pore-scale model. Effects of initial inclusion size and temperature gradient on the migration process were investigated. It was found that variation of the volume of the inclusion is larger for smaller inclusions due to more efficient mass transport from hot sites to cold sites in the narrow closed spaces of a smaller inclusion. In addition, the macro migration velocity is larger for larger inclusions. However, when the inclusion is extremely small, the concentration difference required for dissolution and precipitation cannot be established in the extremely narrow space of the small inclusion, and thus the volume variation of the inclusion is small and the inclusion is almost static. With respect to the temperature gradient, the volume variation and the macro migration velocity are larger for

larger temperature gradients, due to the larger solubility difference, which leads to greater amounts of dissolution and precipitation. However, for a given inclusion size, there is a critical temperature gradient below which the inclusion does not migrate.

Future work will include simulating water migration for more complex geometries such as the interaction of the inclusion with the intergranular pore space in the salt, providing insight to the design of pore-scale experiments, and upscaling the pore-scale results to provide input to field scale modeling.

9. Geomechanical Effects

Disturbance and stress relief caused by the act of excavation and tunneling, and the heating caused by the subsequent testing, will affect the properties of the salt formation in the vicinity of the tunnel. While the extent of these effects during the early period of operation of a repository, or during a two year heater test, is expected to be small, it is necessary to evaluate such processes. The purpose of this chapter is to evaluate the potential impact of mechanical deformation processes coupled with the thermal, hydrological, and chemical processes that are expected to occur within the EDZ in the 2-year time frame of the planned test.

While all the rock properties relevant to the thermal, hydrologic, and mechanical processes are expected to be affected, the most dramatic change is displayed by the permeability of the salt. This can be seen in figure 74 (Figure 9 of Rutqvist et al., 2012), which shows that the salt permeability can change by as much as 5 orders of magnitudes even for relatively small fluid pressure changes, and many more orders of magnitude if the fluid pressure changes exceed the minimum principal in situ stress. The brine enclosed in the fluid inclusions contained in the salt beds will undergo thermal expansion upon heating. The coefficient of thermal expansion for brine is on the order of 2×10^{-4} /^{0}C (e.g. Dittman 1977) and the value for rock salt is on the order of 4×10^{-5} /^{0}C (Table 4.1 of Rutqvist et al., 2012). As the salt heats up, the solid material will expand, and the volume of the fluid inclusions will tend to decrease. At the same time, the brine in the inclusions will tend to expand. Both these effects will contribute to a rise in the fluid pressure in the brine inclusions, driving the salt permeability toward significantly higher values, as seen in Figure 74.

In a field test, it is expected that the tunnel will be in place for some time before heating begins. The same is true for a repository during normal operations. The extent of the EDZ is expected to be about 1.5 to 2 m from the drift face into the host salt beds, as shown in Figure 75 (reproduced form Figure 12 of Park et al. 2007). They used ultrasonic wave velocity data from a cross-hole acoustic test at the WIPP site to estimate the DRZ depth – an abrupt change in the slope of the wave velocity versus depth curve is diagnostic of a boundary between the fractured EDZ and the inteact host rock. They also indicate the range of permeability values in the EDZ to be 2.09×10^{-18} to 10^{-21} m^2.

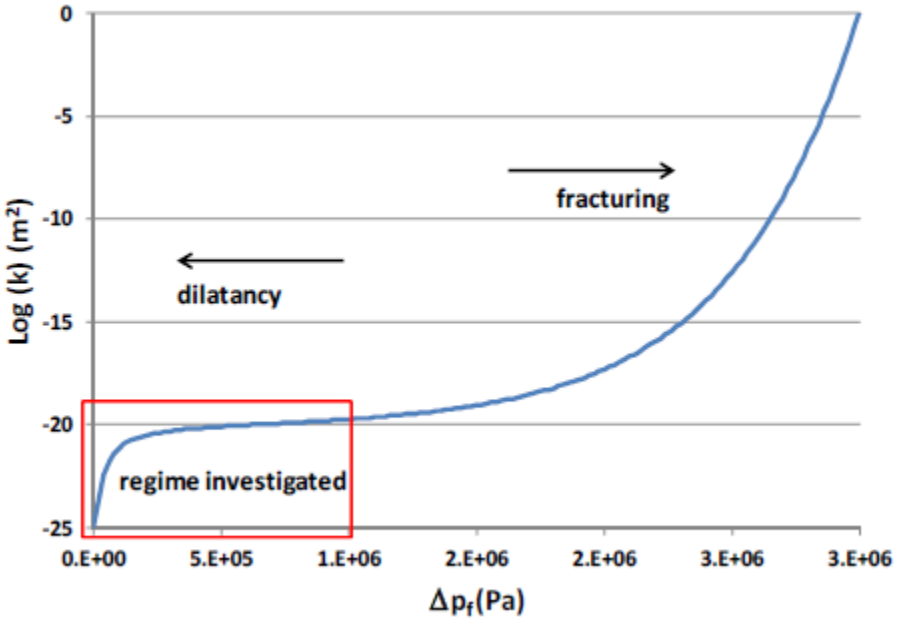

Figure 74: Salt permeability as a function of the fluid pressure change (source: Figure 9 of Rutqvist et al., 2012).

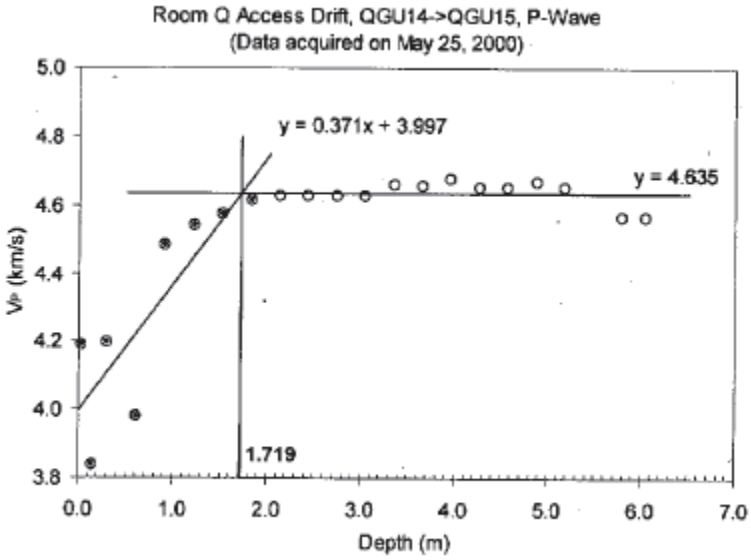

Figure 75: Estimating the depth of the EDZ from the velocity versus depth data from a cross-hole acoustic test (source: Figure 12 of Park et al. 2007).

The EDZ can be conceptualized as a dual porosity, dual permeability medium for the purpose of analyzing fluid flow behavior. EDZ tends to be highly fractured, likely due to the relief of in situ stresses

resulting from excavation and tunnel emplacement - fracture densities in the EDZ at WIPP are reported to be in the range of 164 to 454 per centimeter, with apertures in the range of 47 to 105 micrometers (Section 4.3.3 of Bambus II project report, Bechthold et al., 2004). This implies fracture spacings on the order of 0.002 to 0.006 cm, and permeabilities in the fractures on the order of 10^{-9} to 10^{-10} m^2. The majority of these fractures are thought to be parallel to the tunnel walls; however, such fracturing must be accompanied by fracturing perpendicular to the tunnel walls as well. Even if the fractures orthogonal to the walls have densities lower by a few orders of magnitude than those that are parallel to the walls, this would result in fracture spacings on the order of 0.2 to 0.6 cm. Thus, the fluid from the brine inclusions will have to travel distances on the order of 1 cm or less before gaining access to the high permeability fractures. Nowak et al. (1988) in Section 3.4.1 suggest hydraulic diffusivity values on the order of 10^{-7} m^2/s for the WIPP salt. If the test duration is taken to be 2 years, this would lead to pressure front diffusing over distances on the order of 1.7 m, several orders of magnitude greater than the fracture spacing for the WIPP EDZ. Thus for the time scales considered here, the hydraulic behavior of the EDZ can be well approximated by a single porosity effective medium approach.

In previous chapters, models of the region surrounding the tunnel using this approach suggest that the thermal front travels no further than the depth of the EDZ in 2 years, and that the EDZ remains well-drained over this time frame, and does not build up pore pressures. Thus for the purpose of the current modeling, it is adequate to treat the EDZ as a single porosity medium with effective damaged porosity and permeability values appropriate for the EDZ. It must be recognized that for higher heat loads, longer time frames, or different geometries, the thermal front will travel well beyond the EDZ, so that careful analysis of coupled mechanical-thermal-hydraulic-chemical processes will be required to model the system.

10. Concluding Remarks

In this concluding section, we summarize and reiterate the most important points learned from this modeling study, and point to additional work that could be performed to solidify our conclusions. Defense high level waste and spent nuclear fuel disposal in bedded salt introduces heat to the current WIPP configuration. In this work, coupled Thermal, Hydrological, and Chemical (THC) processes are simulated at both pore and continuum scales. At the continuum scale, coupled processes include solubility of salt as a function of temperature, clay dehydration, wherein clay minerals release water while undergoing mineralogical changes, boiling of saturated salt water and precipitation of salt, transport of water vapor, condensation water vapor back to liquid water and subsequent dissolution of salt, thermal conductivity of salt as a function of porosity and temperature, permeability as a function of porosity, and water vapor pressure as a function of salt concentration and temperature. These processes have been added to FEHM, LANL's state-of-the-art porous flow simulator for multiphase thermal problems.

The FEHM model shows that the heating can lead to porosity changes determined mainly by the water content of the Run of Mine (RoM) salt used as backfill and the heat load of the waste canisters. Heat loads on the order of 750W are required to generate heat pipes assuming five canisters with 0.3 m spacing. Secondary impacts on porosity change include the initial clay content of the RoM salt and the capillary suction in this material. Creation of a strong heat pipe in hot, wet cases leads to porosity reduction in a band around the heaters due to boiling and subsequent precipitation of salt from the circulating brine. Evidence of heat pipe formation in past heater tests at WIPP in Room B boreholes suggests that the mechanism could be important. Lower temperatures result from higher thermal conductivity, where porosity is decreased due to boiling and subsequent precipitation. Threshold initial water content for creation of a heat pipe appears to be between 1.2 and 2.4 wt% water, toward the high end of measured WIPP water contents, but additional work is needed to determine whether a vigorous heat pipe is a realistic expectation for the heater test scenario.

Interestingly, drier initial conditions allow more water to be generated by clay dehydration because of higher temperatures further from the simulated waste canisters. Although clay content and capillary suction are second order effects, they could play a deciding role in cases for which the RoM initial saturation is close to threshold heat-pipe conditions. Prediction success of the model depends on correctly capturing the complex behavior of heated impure salt; bench-scale experiments with intact salt crystals and crushed RoM salt have been performed and work completed to date suggests that the FEHM model shows excellent performance for thermal behavior. The ability of the model to accurately predict

the onset of heat pipe formation in RoM salt could be tested through bench-scale heat pipe experiments that include more of the coupled THC processes. Finally, one approach to increasing the likelihood of heat pipe effects in the SDDI test would be to add brine to the RoM salt, thereby bringing the saturations to the high end of expected saturations. This would provide the opportunity to study the coupled THC effects in-situ in a scenario that could potentially arise from the emplacement of HLW. The downside of this approach is that the test would perhaps be driven to a set of conditions that would not otherwise arise.

Sensitivity analyses indicate that (1) experimental studies to determine conductive, convective, and radiative heat transfer across the air gap are needed to accurately model air temperature in the air gap, (2) the depth of RoM salt can be used to control air gap temperature, (3) accurate intact salt properties are required to accurately model water movement and redistribution within the damaged rock zone (DRZ), and (4) experimental studies on changes to the permeability and porosity are needed to more accurately model water movement and redistribution within the DRZ.

At the pore scale, the coupled multiple physicochemical processes including water-vapor two-phase flow with phase transition, heat transfer, transport of dissolved salt in water, dissolution and precipitation of salt, and dynamic evolutions of the pore-scale geometries of the salt are implemented in a pore-scale model based on the LBM. Some of the simulation results are consistent with experimental observations, e.g., the migration of the liquid inclusion in the direction of the temperature gradient. However, distinct differences also exist that should be the subject of future study. In future simulations, the conditions, including liquid/vapor ratio of the initial inclusion, the direction of temperature gradient with regard to the gravity, as well as defects in the salt crystal will be carefully chosen and/or systematically varied to investigate their effect on the behavior of brine inclusions, and to obtain better agreement between the model and experimental results. Water migration for more complex geometries such as the interaction of the inclusion with the intergranular pore space in the salt should also be simulated to provide insight to the design of pore-scale experiments. With these advances, the pore-scale results should be able to be used to provide upscaled parameters for water migration and release in the field scale modeling.

11. References

Beauheim, R. L., and R. M. Roberts. "Hydrology and hydraulic properties of a bedded evaporite formation," *J. Hydrol.*, 259, 66-88. 2002.

Bechthold W., Smailos E., Heusermann S., Bollingerfehr W., Sabet B.B., Rothfuchs T., Kamlot P., Grupa J., Olivella S., and Hansen F.D., 2004. Backfilling and sealing of underground repositories for radioactive waste in salt (Bambus II project). Final Report for European Atomic Energy Community EUR 20621, Office for Official Publications of the European Communities, Luxembourg. ISBN 92-894-7767-9.

Bejan, A. (1995). Convection Heat Transfer. John Wiley and Sons.

Brady R., C. Herrick, K. Kuhlman, B. Malama, M. Schuhen, and B. Stenson. Sandia Experimental Programs Background and Targeted Activities for Forensic Investigation of Rooms B and A1. NE Milestone M4FT-13SN0818036. Dated August 26, 2013. Page 14.

Bhatnagar, P. L.; Gross, E. P.; Krook, M., A model for collision processes in gases. I. small amplitude processes in charged and neutral one-component systems. *Physical Review* 1954, *94*, (3), 511-525.

Callahan, G., D.C. Guerin, D.G. Levitt, D.L. Newell, B.A. Robinson, L. Van Sambeek. 2012. *Salt Repository Synthesis Data of Non-Delaware Basin and International Programs for the Storage/Disposal of Nuclear Waste.* Los Alamos National Laboratory Report LCO-SDI-002.

Caporuscio, F. A., H. Boukalfa, M. C. Cheshire, A. B. Jordan, and M. Ding, 2013. Brine Migration Experimental Studies for Salt Repositories, FCRD Used Fuel Disposition Campaign Milestone FCRD-UFD-2013-000204, September 25, 2013.

Carter, J.T., F.D. Hansen, R. Kehrman, T.A. Hayes. 2011. *A Generic Salt Repository for Disposal of Waste from a Spent Nuclear Fuel Recycle Facility*. Savannah River National Laboratory Report SRNL-RP-2011-00149.

Carter, J. T., A. J. Luptak, J. Gastelum, C. Stockman, and A. Miller, 2012. Fuel Cycle Potential Waste Inventory for Disposition, Fuel Cycle Research & Development Report FCR&D-USED-2010-000031 Rev 5.

Chen, L.; Luan, H.-B.; He, Y.-L.; Tao, W.-Q., Pore-scale flow and mass transport in gas diffusion layer of proton exchange membrane fuel cell with interdigitated flow fields. *International Journal of Thermal Sciences* 2012, *51*, 132-144.

Chen, L.; Luan, H.; Feng, Y.; Song, C.; He, Y.-L.; Tao, W.-Q., Coupling between finite volume method and lattice Boltzmann method and its application to fluid flow and mass transport in proton exchange membrane fuel cell. *International Journal of Heat and Mass Transfer* 2012, *55*, (13–14), 3834-3848.

Chen, L.; Kang, Q.; He, Y.-L.; Tao, W.-Q., Mesoscopic study of the effects of gel concentration and materials on the formation of precipitation patterns. *Langmuir* 2012, *28*, (32), 11745–11754.

Cinar, Y., G. Pusch, and V. Reitenbach, 2006. Petrophysical and Capillary Properties of Compacted Salt, Transport in Porous Media, 64, 199-228.

Clayton, D.J. and C.W. Gable, 2009. 3-D Thermal Analyses of High-Level Waste Emplaced in a Generic Salt Repository, Advanced Fuel Cycle Initiative, AFCI-WAST-PMO-MI-DV-2009-000002, SAND2009-0633P. LA-UR-09-0089.

Crank J., The Mathematics of Diffusion. Clarendon Press, Oxford, 1979, p. 87.

Christian-Frear, T., and G. Freeze (1997). A method of modeling time-dependent rock damage surrounding underground excavations in multiphase groundwater flow, SAND--97-1310C, Sandia National Laboratories.

Deal D. E. and J. B. Case, IT Corporation, Brine Sampling and Evaluation Program. Phase I Report. DOE-WIPP-87-008, prepared by the Engineering and Technology Department of the Management and Operating Contractor, Waste Isolation Pilot Plant Project for the U. S. Department of Energy, June 1987. .

Dittman G.L., 1977. Calculation of brine properties [Above 80^0F and salt content between 5 and 25%]. Lawrence Livermore National Laboratory Report UCID-17406, DOI: 10.2172/7111583.

DOE Carlsbad Field Office (DOE CBFO), 2012. A Management Proposal for Salt Defense Disposal Investigations (SDDI) for the Disposal of DOE-EM Managed Wastes, U.S. Department of Energy Carlsbad Field Office document, February 2012.

Nowak E. J., D. F. McTigue and R. Beraun, Sandia Report SAND88-0112, Brine Inflow to WIPP Disposal Rooms: Data, Modeling, and Assessment, prepared by Sandia National Laboratories, September 1988. .

FEHM. (2012). FEHM reference list, online at http://fehm.lanl.gov/pdfs/FEHM_references_list.pdf, accessed Aug. 31, 2012. .

Gable, C. W., D. J. Clayton, and Z. Lu. "Inverse Modeling to Determine Thermal Properties of Salt due to Heating From High Level Waste Emplaced in a Generic Salt Repository." U.S. DOE Office of Nuclear Fuel Recycling Report AFCI-WAST-PMO-DV-2009-000001. 2009.

Gangi A. F. (1978), Variation of whole and fractured porous rock permeability with confining pressure, Rock Mech. Sci. and Geomech. Abstr. 15: 249-257.

GRIDDER (2012). Gridder Users Manual, (Loraine Lundquist), on-line at https://meshing.lanl.gov/gridder/users_manual.html accessed Aug. 31, 2012. .

Hansen, F.D., and C.D. Leigh. "Salt Disposal of Heat-Generating Nuclear Waste."SAND2011-0161. Albuquerque: Sandia National Laboratories. 2011.

Hardin, E., J. Blink, H. Greenberg, M. Sutton, M. Fratoni, J. Carter, M. Dupont, and R. Howard, 2011. Generic Repository Design Concepts and Thermal Analysis (FY11), SAND2011-6202. Albuquerque: Sandia National Laboratories.

Harp D.R., P.H. Stauffer, P.K. Mishra, D.G. Levitt, and B.A. Robinson (2013). Thermal Modeling of High-Level Nuclear Waste Disposal in a Salt Repository. Nuclear Technology. In Revision).

Holcomb, D. J., and R. D. Hardy. "Assessing the disturbed rock zone (DRZ) at the Waste Isolation Pilot Plant in salt using ultrasonic waves characteristics of the DRZ." *Proc. 38th U.S. Symp. on Rock Mech.*, Paper 01-0489. 2001.

Huang, H.-B.; Lu, X.-Y.; Sukop, M. C., Numerical study of lattice Boltzmann methods for a convection–diffusion equation coupled with Navier–Stokes equations. *J. Phys. A: Math. Theor.* 2011, *44*, 055001.

Huang, H.; Krafczyk, M.; Lu, X., Forcing term in single-phase and Shan-Chen-type multiphase lattice Boltzmann models. *Physical Review E* 2011, *84*, (4), 046710.

Incropera, F., and D. Dewitt, 1985. Introduction to Heat Transfer, OSTI ID: 6008316.

Kang, Q.; Zhang, D.; Chen, S.; He, X., Lattice Boltzmann simulation of chemical dissolution in porous media. *Physical Review E* 2002, *65*, (3), 036318.

Kang, Q.; Zhang, D.; Lichtner, P. C.; Tsimpanogiannis, I. N., Lattice Boltzmann model for crystal growth from supersaturated solution. *Geophysical research letters* 2004, *31*, L21604.Morris, M.D. (1991). Factorial Sampling Plans for Preliminary Computational Experiments. Technometrics 33(2). pp. 161-174.

Kang, Q. J.; Zhang, D. X.; Chen, S. Y., Displacement of a three-dimensional immiscible droplet in a duct. *J. Fluid Mech.* 2005, *545*, 41-66.

Kang, Q. J.; Lichtner, P. C.; Zhang, D. X., Lattice Boltzmann pore-scale model for multicomponent reactive transport in porous media. *Journal of Geophysical Research-Solid Earth* 2006, *111*.

Kang, Q.; Lichtner, P. C.; Zhang, D., An improved lattice Boltzmann model for multicomponent reactive transport in porous media at the pore scale. *Water resources research* 2007, *43*, W12S14.

Kelkar, S., G. WoldeGabriel, and K. Rehfeldt, 2011. Hot Dry Rock Geothermal Energy Development at Los Alamos National Laboratory: 1970-1995, Final Report. Los Alamos National Laboratory Report LA-14433-HDR.

Kuhlman, K., S. Wagner, D. Kicker, R. Kirkes, C. Herrick, D. Guerin. 2012. *Review and Evaluation of Salt R&D Data for Disposal of Nuclear Waste in Salt.* DOE Office of Nuclear Energy Report FCRD-UFD-2012-000380.

Kuhlman, K.L. and Malama, B. (2013). *Brine Flow in Heated Geologic Salt*. SAND2013–1944, Albuquerque, NM: Sandia National Laboratories.

Kreith, F, and M.S. Bohn, 1993. Principles of Heat Transfer, 5th ed., St. Paul, MN: West Publishing Company, p. 176.

Krumhansl, J. L., C. L. Stein, G. D. Jarrell, and K. M. Kimball, 1991. Summary of WIPP Room B heater test brine and backfill material data. SAND90-0626, Sandia National Laboratories, Albuquerque, NM, 1991.

Kwicklis, E.M., A.V. Wolfsberg, P.H. Stauffer, M.A. Walvroord, and M.J. Sully (2006), Multiphase Multicomponent Parameter Estimation for Liquid and Vapor Fluxes in Deep Arid Systems Using Hydrologic Data and Natural Environmental Traces, *Vadose Zone Journal*, 2006 5:934-950

Li, Q.; Luo, K. H.; Li, X. J., Forcing scheme in pseudopotential lattice Boltzmann model for multiphase flows. *Physical Review E* 2012, *86*, (1), 016709.

McTigue, D. F. (1985), A linear theory for porous thermoelastic materials, SAND85-1149, Sandia National Laboratories, September 1985.

McTigue, D. F. and J. E. Nowak, 1988. Brine transport studies in the bedded salt of the Waste Isolation Pilot Plant (WIPP). SAND87-1274C, Sandia National Laboratories, Albuquerque, NM, December 1988.

Morris, M.D. (1991). Factorial Sampling Plans for Preliminary Computational Experiments. Technometrics 33(2). pp. 161-174.

Munson, DE, RL Jones, JR Ball, RM Clancy, DL Hoag and SV Petney. 1990. *Overtest for Simulate Defense High-Level Waste (Room B): In Situ Data Report (May 1984-February 1988) Waste Isolation Pilot Plant (WIPP) Thermal/Structural Interactions Program*, Sandia National Laboratories, SAND89-2671.

Notz, K.J., 1990. Characteristics of Potential Repository Wastes, First Annual International High-Level Radioactive Waste Management Conference, Las Vegas, Nevada, CONF-900406-11, April 1990.

Nowak E.J., McTigue D.F., and Beraun R., 1988. Brine Inflow to WIPP Disposal Rooms: Data, Modeling and Assessment. Sandia National Laboratory Report SAND88-0112.UC-70.

Olander, D. R.; Machiels, A. J.; Balooch, M.; Yagnik, S. K., Thermal gradient migration of brine inclusions in synthetic alkali halide single crystals. *J. Appl. Phys.* 1982, *53*, 669-681.

Park B.Y., Ismali A., Hilcomb D.J., and Herrick C.G., 2007. Analysis Report for Prediction of the Extent and Permeability of the Disturbed Rock Zone around a WIPP Disposal Room. Sandia National Laboratory Report WIPP: 1.4.1.2: PA:QA-L:545583

Pfeifle, T. W., and L. D. Hurtado, 1998. "Permeability of natural rock salt from the Waste Isolation Pilot Plant (WIPP) during damage evolution and healing," *Int. J. Rock. Mech. Mining Sci. Geomech.*, 35, 4, 637-638.

Polubarinova-Kochina, P., 1962. Theory of Ground Water Movement. Princeton University Press, Princeton,. N. J., 613 pp.

Pujol, G., Iooss, B., and Janon, A. (2013) sensitivity: Sensitivity Analysis. R package version 1.7, http://CRAN.R-project.org/package=sensitivity

Robinson, B. A.; Elkins, N. Z.; Carter, J. T., Development of a U.S. nuclear waste repository research program in salt. *Nuclear Technology* **2012,** *180*, 122-138.

Rutqvist J, Blanco-Martin L., Houseworth J., 2012. THM Coupled Process Modeling with TOUGHFLAC to Evaluate the Fate and Transport of Water in a Salt-Based Repository. Lawrence Berkeley National Laboratory Report FCRD-UFD-2012-000297.

Shan, X.; Chen, H., Lattice Boltzmann model for simulating flows with multiple phases and components. *Phys. Rev. E* **1993,** *47*, 1815-1819.

Shan, X.; Chen, H., Simulation of nonideal gases and liquid-gas phase transitions by the lattice Boltzmann equation. *Physical Review E* 1994, *49*, (4), 2941-2948.

Sparrow, B. S., 2003. Empirical equations for the thermodynamic properties of aqueous sodium chloride, Desalination, 159, 2, 161-170.

Svalstad, D.K., 1983. Forced ventilation analysis of a commercial high-level nuclear waste repository in salt ; prepared for Office of Nuclear Waste Isolation, Battelle Memorial Institute. Published 1983 by The Office, Available from National Technical Information Service in Columbus, Ohio, Springfield, VA .

Stauffer P.H., and Rosenberg, N.D. (2000), Vapor phase transport at a hillside landfill, *Environmental and Engineering Geoscience*, Vol. VI, No. 1, p. 71-84

Stauffer P.H., Auer, L.H., and Rosenberg, N.D.(1997), Compressible gas in porous media: A finite amplitude analysis of natural convection, *Int. J. of Heat and Mass Transfer,* 40 (7), 1585-1589.

Sullivan, S. P.; Sani, F. M.; Johns, M. L.; Gladden, L. F., Simulation of packed bed reactors using lattice Boltzmann methods. *Chemical Engineering Science* 2005**,** *60*, (12), 3405-3418.

Van Sambeek, L. L., J. L. Ratigan, and F. D. Hansen. "Dilatancy of rock salt in laboratory tests." *Int. J. Rock. Mech. Mining Sci. Geomech. Abstr.,* 30, 7, 735-738. 1993.

Walsh, S. D. C.; Saar, M. O., Interpolated lattice Boltzmann boundary conditions for surface reaction kinetics. *Physical Review E* 2010, *82*, (6), 066703.

Weaver, D., 2013. Test Strategy Plan – Exploration of the WIPP North Experimental Area, LCO-SDI-003-REVISION 0A.

Yuan, P.; Schaefer, L., Equations of state in a lattice Boltzmann model. *Physics of Fluids* 2006, *18*, (4), 042101:1-11.

Zhang, T.; Shi, B.; Guo, Z.; Chai, Z.; Lu, J., General bounce-back scheme for concentration boundary condition in the lattice-Boltzmann method. *Physical Review E* 2012, *85*, (1), 016701.

Zyvoloski, G.A., B.A. Robinson, Z.V. Dash, and L.L. Trease. 1997. Summary of the models and methods for the FEHM application— A finite-element heat-and mass-transfer code. Rep. LA-13307-MS. Los Alamos National Laboratory, Los Alamos, NM. .

Zyvoloski, G.A.(2007). *FEHM: A control volume finite element code for simulating subsurface multi-phase multi-fluid heat and mass transfer*, Report LA-UR-07-3359, Los Alamos National Laboratory.

Appendix A

Analytical solutions for transport in a cylindrical medium with composite properties

Appendix A

The governing equations for pressure in the EDZ and the intact salt are

$$\frac{\partial^2 p_1}{\partial r^2}+\frac{1}{r}\frac{\partial p_1}{\partial r}=\frac{1}{\kappa_1}\frac{\partial p_1}{\partial t},\quad a<r\le b, t>0 \tag{A1}$$

$$\frac{\partial^2 p_2}{\partial r^2}+\frac{1}{r}\frac{\partial p_2}{\partial r}=\frac{1}{\kappa_2}\frac{\partial p_2}{\partial t},\quad b<r\le c, t>0 \tag{A2}$$

subject to initial and boundary conditions

$$p_1(r,t)=P_0,\quad a<r\le b, t=0, \tag{A3}$$

$$p_2(r,t)=P_0,\quad b<r\le c, t=0, \tag{A4}$$

$$p_1(r,t)=P_a,\quad r=a, t>0, \tag{A5}$$

$$p_2(r,t)=P_c,\quad r=c, t>0, \tag{A6}$$

where p stands for the pressure head [Pa], P_0 is the initial pressure head in the domain, P_a and P_c are respectively the pressure head prescribed at $r=a$ and $r=c$, $\kappa=k/\phi C_t\mu$ is the diffusivity [m^2/s], k is permeability [m^2], ϕ is porosity [-], C_t is the total compressibility [Pa^{-1}], μ is the dynamic viscosity [$Pa\cdot s$], r is radial distance from the center of the cavity, and t is time. Subscripts '1' and '2' represent the quntities for the EDZ and the intact rock salt, respectively.

To solve equations (A1)-(A6), one needs two additional conditions at the interface $r=b$:

$$p_1(r,t)=p_2(r,t),\quad r=b, t>0 \tag{A7}$$

$$K_1\frac{\partial p_1}{\partial r}=K_2\frac{\partial p_2}{\partial r},\quad r=b, t>0, \tag{A8}$$

where K_1 and K_2 are the hydraulic conductivity [m/s] of the EDZ and the intact rock salt. Because the hydraulic conductivity is related to permeability by $k=K\mu/\rho g$, where ρ is the density of water and g is the gravitational constant (= $9.81 m^2/s$), (A8) can also be rewritten in terms of permeability k.

By some simple manipulations, these equations can be transformed to two sets of equations, whose solutions can be derived directly from Jaeger (1941), and the final solutions are then obtained by combining two sets of solutions:

$$\begin{aligned} p_1(r,t)=P_0+(P_a-P_0)&\left[\frac{k_1\ln(c/b)+k_2\ln(b/r)}{k_1\ln(c/b)+k_2\ln(b/a)}-\pi k_1k_2\sum_{n=1}^{\infty}e^{-\kappa_1\alpha_n^2 t}C(r\alpha_n,a\alpha_n)C^2(\kappa b\alpha_n,\kappa c\alpha_n)F(\alpha_n)\right]\\ +(P_c-P_0)&\left[\frac{k_2\ln(r/a)}{k_1\ln(c/b)+k_2\ln(b/a)}+\pi k_2^2\sum_{n=1}^{\infty}e^{-\kappa_1\alpha_n^2 t}C(r\alpha_n,a\alpha_n)C(\kappa b\alpha_n,\kappa c\alpha_n)C(b\alpha_n,a\alpha_n)F(\alpha_n)\right] \end{aligned} \tag{A9}$$

and

$$p_2(r,t) = P_0 + (P_a - P_0)\left[\frac{k_1 \ln(c/r)}{k_1 \ln(c/b) + k_2 \ln(b/a)}\right.$$
$$\left. - \pi k_1 k_2 \sum_{n=1}^{\infty} e^{-\kappa_1 \alpha_n^2 t} C(\kappa r\alpha_n, \kappa c\alpha_n) C(\kappa b\alpha_n, \kappa c\alpha_n) C(b\alpha_n, a\alpha_n) F(\alpha_n)\right] \tag{A10}$$
$$+(P_c - P_0)\left[\frac{k_1 \ln(r/b) + k_2 \ln(b/a)}{k_1 \ln(c/b) + k_2 \ln(b/a)} + \pi k_2^2 \sum_{n=1}^{\infty} e^{-\kappa_1 \alpha_n^2 t} C(\kappa r\alpha_n, \kappa c\alpha_n) C^2(b\alpha_n, a\alpha_n) F(\alpha_n)\right]$$

where $\kappa = \sqrt{\kappa_1 / \kappa_2}$, α_n are the positive roots of the following equation

$$k_1 C_1(b\alpha, a\alpha) C(\kappa b\alpha, \kappa c\alpha) - \kappa k_2 C(b\alpha, a\alpha) C_1(\kappa b\alpha, \kappa c\alpha) = 0, \tag{A11}$$

and $F(\alpha)$ is defined as

$$[F(\alpha_n)]^{-1} = C^2(\kappa b\alpha, \kappa c\alpha_n)\left\{\frac{1}{4}\pi^2 b^2 k_2 (k_2\kappa^2 - k_1)\alpha_n^2 C^2(b\alpha, a\alpha_n)\right.$$
$$\left. + \frac{1}{4}\pi^2 b^2 k_1 (k_1 - k_2)\alpha_n^2 C_1^2(b\alpha, a\alpha_n) + k_1 k_2\right\} - k_2^2 C^2(b\alpha_n, a\alpha), \tag{A12}$$

and $C(x,y)$ is the cylinder function defined as

$$C(x,y) = J_0(x)Y_0(y) - Y_0(x)J_0(x) \tag{A13}$$

where J_0 is the Bessel function of the first kind of order zero and Y_0 is the Bessel function of the second kind of order zero. Function $C_1(x,y)$, or $C_{1,0}(x,y)$, denotes the first-order partial derivative of C with respect to the first argument $C_1(x,y) = \partial C(x,y)/\partial x = -J_1(x)Y_0(y) + Y_1(x)J_0(y)$, where J_1 and Y_1 are respectively the Bessel functions of the first and the second kind of order one.

The total flow rate to the tunnel of length h can be written as

$$Q(t) = -\frac{2\pi a h k_1}{\mu} \left.\frac{\partial p_1}{\partial r}\right|_{r=a} \tag{A14}$$

where the derivative can be found from (A9):

$$\left.\frac{\partial p_1}{\partial r}\right|_{r=a} = \frac{k_2/a}{k_1 \ln(c/b) + k_2 \ln(b/a)}\left[P_c - P_a\right]$$
$$- \pi k_1 k_2 (P_a - P_0) \sum_{n=1}^{\infty} \alpha_n e^{-\kappa_1 \alpha_n^2 t} C_1(a\alpha_n, a\alpha_n) C^2(\kappa b\alpha_n, \kappa c\alpha_n) F(\alpha_n)$$
$$+ \pi k_2^2 (P_c - P_0) \sum_{n=1}^{\infty} \alpha_n e^{-\kappa_1 \alpha_n^2 t} C_1(a\alpha_n, a\alpha_n) C(\kappa b\alpha_n, \kappa c\alpha_n) C(b\alpha_n, a\alpha_n) F(\alpha_n) \tag{A15}$$

The steady-state flow rate can be derived by taking the limit of time approaching infinity:

$$Q_\infty = \frac{2\pi h}{\mu} \frac{k_1 k_2}{k_1 \ln(c/b) + k_2 \ln(b/a)}\left[P_c - P_a\right] \tag{A16}$$

For a special case of $k_1 = k_2$, the steady-state flow rate reduces to

$$Q_\infty = \frac{2\pi h k}{\mu \ln(a/c)}\left[P_c - P_a\right] \tag{A17}$$

References for Appendix A

Jain, P. C., The computation of the thermal conductivity of air in the temperature range 400-1600K, J. Phys D: Appl. Phys., 10, 2389-2391, 1977.

D.R. Caldwell, Thermal conductivity of sea water, Deep Sea Res. Oceanogr. Abstr. 21 (1974) 131–137.

D.T. Jamieson, J.S. Tudhope, Physical properties of sea water solutions: thermal conductivity, Desalination 8 (1970) 393–401.

Olivella, S. S. Castagna, E. E. Alonso, A. Lloret, Porosity Variations in Saline Media Induced by Temperature Gradients: Experimental Evidences and Modeling, Transport in Porous Media, 90: 763-777, 2011.

Castelli, V. J, and E. M. Stanley, The thermal conductivity of pure water and standard sea water as a function of pressure and temperature, Part II- Pure water, Naval Ship Research and Development Center report, AD-751 025.

Castelli, V. J., E.M. Stanley, and E.C. Fischer, The thermal conductivity of seawater as a function of pressure and temperature, Deep-Sea Research, 21, 311-319, 1974.

Ramires, M. L. V., C. A. Nieto de Castro, Y. Nagasaka, A. Nagashima, M. J. Assael, and W. A. Wakeham, Standard reference data for the thermal conductivity of water, 1994.

Sharqawy, M. H., New correlations for seawater and pure water thermal conductivity at different temperatures and salinities, Desalination, 313, 97-104, 2013.